Imaging of gas-hydrate deposits with full-waveform inversion of ocean-bottom seismic data

Zur Erlangung des akademischen Grades
Doktor der Naturwissenschaften
von der KIT-Fakultät für Physik des
Karlsruher Instituts für Technologie (KIT)

genehmigte
Dissertation
von

M.Sc. Laura Gaßner

Tag der mündlichen Prüfung:	07. Dezember 2018
Referent:	Prof. Dr. Thomas Bohlen
Korreferent:	Prof. Dr. Andreas Rietbrock

Abstract

Within this work the potential of full-waveform inversion (FWI) applied on ocean-bottom seismic (OBS) data in the context of gas-hydrate exploration is investigated. The detection of hydrate is typically achieved by conventional seismic methods, namely the analysis of migrated reflection-seismic streamer data where interpretation is based on reflectivity amplitudes which provide information on geological structures. In reflection seismic data gas-hydrate occurrence is indicated by the observation of so-called bottom-simulating reflectors (BSRs) which result from the typical elastic parameter distribution at the base of the gas-hydrate stability zone. In this work the delineation of potential hydrate and gas zones is achieved directly from the elastic parameter models resulting from FWI. The benefit of FWI is the capability to resolve highly detailed multiparameter models of the subsurface by using amplitude and phase information compared to standard ray-based methods where only arrival times are considered. In seismic exploration the application of FWI is still not a standard method, as it is costly in terms of calculation time and the use of supercomputers is required. Through the application of the reciprocity principle, OBS applications provide an opportunity to achieve results with highly reduced calculation time compared to streamer methods because of the relatively low number of stations.

Synthetic tests show the applicability of FWI to robustly reconstruct models of the P-wave velocity v_P with a subseafloor parameter distribution containing a hydrate and gas signature by using a typical OBS field geometry. In contrast, an increase in the S-wave velocity v_S which could give further indications for hydrate occurrence cannot be reconstructed. Little sensitivity towards the S-waves is observed because of their low amplitudes compared to P-wave signals. Under the given conditions an elastic inversion, where S-waves are considered, provides little to no benefit and only marginally improves the inversion result of the P-wave velocity model compared to an acoustic inversion. Reliable density values cannot be reconstructed by the inversion and at the bottom of the gas hydrate stability zone the parameter distribution of the P-wave velocity model is mimicked. Thereby the resolution of the BSR signature in v_P is decreased. This implies that results with additional inversion for ρ should be compared to results of inversion for v_P only, regarding an evaluation of hydrate and gas occurrence.

The successful application of 2D acoustic FWI to an OBS data set from the Western Black Sea is shown with the purpose of studying the distribution of gas-hydrate deposits. The data set was measured in the area of the Danube deep-sea fan where regional seismic measurements indicate the presence of large regions of BSRs. Traveltime tomography models serve as input for FWI which give no indications on zones of potential hydrate and gas occurrence. Hydrophone data from 10 OBS stations of two parallel profiles (P1 and P2) of 14 km length with 1 km separation between them are inverted. Results show that the application of time windowing to suppress the direct wave and primary reflections is beneficial for the inversion, because strong artifacts near the OBS positions are reduced which arise due to deviations of the OBS stations in the inversion geometry compared to the 3D field geometry.

A characteristic P-wave velocity trend for hydrate and gas occurrence at BSR depth is found in the first of the analyzed profiles with a horizontal extend of at least 5.6 km. No indications for gas accumulations below the predicted BSR on the second profile and only weak indications for hydrate are observed. These differences in v_P signature are consistent with reflectivity behavior of the migrated seismic streamer data of both profiles where a zone of high-reflectivity amplitudes is coincident with the potential gas zone derived from the FWI result. The comparison with seismic streamer data shows that the application of monoparameter v_P inversion provides structures of larger horizontal extent which is in better agreement with structures indicated by the reflectivity images. Calculating saturation estimates for the potential hydrate and gas zones yields values of up to 30 % and 1.2 %, respectively. The shape of these zones again indicates a typical gas and hydrate distribution at profile P1 above and below the BSR, respectively. At profile P2 only small areas of potential gas occurrence are observed below the predicted BSR and no distinctive zones of possible hydrate occurrence.

The application of acoustic FWI proves to be a reliable tool to assess the distribution and extent of potential hydrate and gas zones in the subsurface from resulting models of v_P.

Contents

1 Introduction

Exploration of the subsurface with geophysical methods is the main route to finding new energy resources. Conventional resources such as oil and gas are vastly explored and more and more reservoirs are being exploited. With the depletion of these resources in sight, potential future reservoirs are searched for to sustain our energy supply until renewable energy can provide a large enough share. As an unconventional reservoir gas hydrates have been in the focus of research since the late 1980s (e.g., Kvenvolden, 1988). Gas hydrates are molecules of gas, such as methane (CH_4), bound in water ice cages which occur naturally in permafrost regions and at continental margins. Low temperatures and high pressures are necessary for hydrates to form and limit their occurrence to a stability zone which extends to a few hundred meters below the earth's surface. They typically occur in the oceans where water depths are greater than 400 m. As they can be found in the shallow subsurface and have a high energy density (1 m^3 of hydrate stores a gas volume of 164 m^3) gas hydrates are regarded as a promising future reservoir (Kvenvolden, 1993). Recently, the amount of carbon available from hydrates has been estimated to be more than 455 Gt (Wallmann et al., 2012). Furthermore, the storage of carbon dioxide (CO_2) in hydrate layers exchanging it for methane is possible and therefore a potential method to dispose of a waste product of burning fossil fuels (e.g., Kvamme et al., 2007). Acting as a greenhouse gas the release of high amounts of methane from hydrates due to a change in the stability regime also poses a threat to the global climate. Therefore, increasing water temperatures caused by climate change could induce the release of methane from the subsurface which would then reinforce global warming. Furthermore, a correlation of hydrate occurrence and slope instability has been observed (e.g., Elger et al., 2018).

With gas hydrate acting as a climate factor, potential geohazard and future energy source, many works focus on the exploration of hydrate provinces. Indications for gas-hydrate deposits range from seabed features or the observation of gas seeps containing CH_4 to anomalies in geophysical data. Although recently also electromagnetic methods have been applied identifying hydrate and gas by their increased resistivity compared to surrounding sediments (e.g., Schwalenberg et al., 2005), seismic methods are most common to detect gas-hydrate deposits. By the observation of bottom-simulating reflectors (BSRs) which mark the lower bound of the gas-hydrate stability zone (GHSZ) hydrate occurrence can be identified. The characteristic distribution of hydrate and gas in the subsurface leads to a reflection with opposite polarity compared to the seafloor reflection. The BSR results from a contrast in the characteristic compressional wave velocity v_P of sediments hosting hydrate compared to water- or gas-saturated sediments. Because the depth of the bottom of the GHSZ depends on the temperature gradient in the subsurface and the overburden, the BSR is roughly parallel to the seafloor and may crosscut geological layers. Vice versa, the local temperature gradient can be calculated from the observation of a BSR (Shipley et al., 1979). Depending on the composition of the hosting sediment, hydrate will form in the pore space or become load bearing by cementing the sediment grains (e.g., Waite et al., 2009). In this case the occurrence of hydrate also affects the stiffness of the sediment and therefore influences the seismic shear

wave velocity v_S. If veins and fractures are present in the subsurface hydrate can occur in massive form. Effects of hydrate also show in the attenuation of seismic waves as attenuation is increased through the typical distribution of hydrate in the pore spaces (e.g., Guerin and Goldberg, 2002; Gerner et al., 2007). When hydrate constitutes part of the sediment matrix a contrary attenuation effect is assumed (Jaiswal et al., 2012).

In order to detect gas-hydrate occurrence highly detailed parameter models of the P-wave velocity (possibly also the S-wave velocity and attenuation) are necessary. By means of such models not only the base of the GHSZ can be delineated but also the vertical extent of a potential reservoir. Furthermore, the parameter values can provide indications about the saturation of the sediments with hydrate or gas. To derive highly detailed models of the subsurface parameter distribution the concept of seismic full-waveform inversion (FWI) was introduced in the 1980s by Tarantola (1984) and Mora (1988). Instead of arrival times the full amplitude and phase information of recorded signals is utilized in FWI. The aim of FWI is the minimization of the misfit between measured data from a field survey and calculated data for a set of model parameters. In an iterative approach parameter models are updated to explain all events of the field data in both their traveltimes and amplitudes. Due to the complexity of the problem a local optimization is applied. A starting model is needed which can already explain the observed signals within half a wavelength to avoid a mismatch in phase (cycle skipping). The resolution of the final models depends on the available frequency content of the data. The frequency range is limited due to increasing discretization requirements and therefore increasing model size with higher frequencies. Due to the large number of wavefield calculations, which is proportional to the number of seismic source positions, FWI is run on high-performance computer systems with several hundreds to thousands of cores.

The application of full-waveform inversion in exploration seismics has become more and more popular over the last decade. An increased model resolution is achieved by FWI compared to other methods but the interpretation of reflection seismic data still provides better resolution of the subsurface as there are fewer limitations regarding the frequency range. In FWI the available computational power has been a limiting factor but with better software and bigger supercomputers even 3D applications are achievable (e.g., Warner et al., 2013). The main advantage of FWI is the interpretability of absolute values of the elastic parameters of the subsurface that can be obtained from the resulting subsurface models. However, through the local optimization approach used in FWI results are strongly dependent on the starting models and because of the large number of model parameters no direct error estimation is possible. To mitigate these problems results for different workflows and input parameters need to be compared and discussed. Quality control criteria, like the convergence of the misfit function and the similarity of inverted source-time functions, are established to verify the success of an FWI run. Furthermore, the plausibility of the final models needs to be checked by additional results from further independent measurements and methods.

Previously, applications have demonstrated the potential of FWI to delineate structures relatable to hydrate occurrence. First studies using seismic streamer data and aiming at gas-hydrate characterization were performed by Singh et al. (1993), Pecher et al. (1996), and Korenaga et al. (1997) with a 1D acoustic approximation for selected sites. They derive v_P profiles where the velocity increases by up to 300 m/s above and drops by up to 600 m/s at BSR depth, hinting at hydrate over gas occurrence. A 2D acoustic

FWI approach was applied by Delescluse et al. (2011) to multichannel seismic (MCS) data. They observe increased velocities and associate it with a gas-hydrate zone as well as low-velocity zones related with the occurrence of gas. Delescluse et al. (2011) conclude from their study that the acoustic approximation is also applicable to far-offset data if v_S varies smoothly with depth. Kim et al. (2013) show results of 2D elastic FWI, where they observe increased P- and S-wave velocities as well as a reduced Poisson ratio in a zone which they relate to hydrate occurrence. An underlying layer of decreased velocity and higher Poisson ratio is interpreted as a gas zone. Jaiswal et al. (2012) perform 2D visco-acoustic FWI and relate increased velocities as well as reduced attenuation to the presence of gas hydrate, and reduced velocities and increased attenuation to gas occurrence. Based on 1D inversion results of the P-wave velocity Crutchley et al. (2011) estimate hydrate and gas saturation of the sediment.

1.1 Motivation

In this work the potential of the application of FWI to an ocean-bottom seismic (OBS) data set in the context of gas-hydrate exploration is investigated. In all previously mentioned studies FWI was applied to MCS data, but the potential and limitations to explore hydrate and gas distribution by the inversion of OBS data has not been assessed before. Although only few stations are usually available in an OBS experiment, the approach is advantageous in terms of computation time. The application of the reciprocity principle allows to use OBS locations as virtual source positions, and the actual shot locations as virtual receiver positions. This approach decreases the overall computation time compared to conventional MCS applications significantly, where hundreds of shot positions have to be evaluated.

The feasibility of the characterization of gas-hydrate deposits from OBS data by 2D FWI is evaluated using a data set recorded in the Western Black Sea where gas-hydrate occurrence has been inferred from reflection seismic measurements (Bialas et al., 2014). It is assessed wether the delineation of potential hydrate and gas zones and the estimation of saturation values is possible from an independent evaluation of the parameter models constructed by FWI only.

1.2 Overview

In Chapter 2 the basic concept of FWI is described with all the necessary components that are implemented to obtain the results shown in this work.

A synthetic example is developed to illustrate the potential of FWI to recover a BSR structure in a multiparameter model for an OBS measurement setting. The results and restrictions of the approach are discussed in Chapter 3.

An introduction to the field data set is given in Chapter 4, with an illustration of the preprocessing of the data and the preparation of the starting models.

The details and results of the application of acoustic FWI to the field data is shown in Chapter 5. Furthermore, their evaluation as well as an interpretation in terms of potential hydrate and gas saturation of the parameter models resulting from FWI is given in Chapter 6.

Conclusions are drawn in Chapter 7.

2 Full-waveform inversion

To gain knowledge about the subsurface data are collected by geophysical measurements. By passive or active methods spatially distributed data points or time series are acquired. Based on the geometry of the measurement, i.e. the location of sources and receivers, a model of the subsurface parameter distribution is calculated by the inversion of the measured data. Methods range from inverting the full data to only a subset or specific attributes of the data. The sampling of the subsurface by the geometry, the quality of the data (e.g. signal-to-noise ratio), and the accuracy of the assumptions on the actual physics are the main contributions to find a meaningful model.

The overall aim of seismic FWI is the construction of a subsurface model which can explain a measured seismic data set best with the chosen approach. In this work I apply 2D time-domain full-waveform inversion with the implementation developed by Köhn (2011). The main part of the inversion process is the simulation of seismic wavefields based on a set of model parameters (*forward modeling*). For each seismic source a wavefield is propagated through the model. The wave propagation is calculated on an equidistant Cartesian grid with a finite-difference forward solver (Bohlen, 2002).

In order to reduce the non-linearity of the inverse problem, different strategies can be applied. Usually, low-pass filtering is used to gradually increase the frequency content of the input data. Furthermore, time windowing can be applied to invert available information successively. This is called a multiscale approach and provides a framework to control the inversion process.

2.1 Forward modeling

To calculate seismograms from a given model a set of equations is necessary to describe the characteristics of wave propagation. In this section the theory of wave propagation in elastic, visco-elastic and acoustic media is presented. I use the Einstein notation, which means that repeated indices in a product indicate a summation over this index.

2.1.1 Wave equation

Two equations govern the propagation of seismic waves (Lay and Wallace, 1995). The first is the equation of motion, which is based on Newton's second law

$$\rho \frac{\partial v_i}{\partial t} = \frac{\partial \sigma_{ij}}{\partial x_j} + f_i \tag{2.1}$$

with the density ρ and the derivative of the particle velocity v with respect to time t on the left hand side of the equation and terms of volume force density f and surface force density, consisting of the derivative of the stress tensor σ with respect to the spatial coordinates x_i ($i = 1,2,3$), on the right.

The second equation is the stress-strain relationship, or Hooke's law, which is valid for small deformations and is generally formulated as

$$\sigma_{ij} = C_{ijkl}\varepsilon_{kl} \tag{2.2}$$

with the stress tensor σ, the elasticity tensor C and the strain tensor ε. Due to symmetries of the stress and strain tensors, and laws of conservation, C comprises a maximum of 21 independent parameters in 3D. In the case of an elastic and isotropic medium C is further reduced to two parameters. Therefore Equation 2.2 simplifies to

$$\sigma_{ij} = \lambda \operatorname{tr}(\varepsilon)\delta_{ij} + 2\mu\varepsilon_{ij} \tag{2.3}$$

with the Kronecker delta δ_{ij}, which equals 1 if $i = j$ and 0 if $i \neq j$, and the Lamé parameters λ and μ. While λ has no physical meaning μ is called shear modulus, defining the ratio of shear stress to shear strain which is a characteristic value for a medium.

The relation of the strain tensor to the particle velocities is expressed by

$$\frac{\partial \varepsilon_{ij}}{\partial t} = \frac{1}{2}\left(\frac{\partial v_i}{\partial x_j} + \frac{\partial v_j}{\partial x_i}\right) \tag{2.4}$$

which allows to rewrite Equation 2.3 as

$$\frac{\partial \sigma_{ij}}{\partial t} = \lambda \frac{\partial v_k}{\partial x_k}\delta_{ij} + \mu\left(\frac{\partial v_i}{\partial x_j} + \frac{\partial v_j}{\partial x_i}\right). \tag{2.5}$$

The set of first-order differential equations given by 2.1 and 2.5 fully describes the propagation of elastic waves in an isotropic, perfectly linear-elastic medium.

2.1.2 Attenuation

Subsurface media may be anelastic and exhibit absorption of seismic energy which is transferred to heat. To include a level of (intrinsic) attenuation in the model the medium under consideration is described by a generalized standard linear solid (GSLS) which consists of L parallel Maxwell bodies (a spring in series with a dash pot) in parallel with a spring (Blanch et al., 1995; Bohlen, 2002). Equation 2.3 is expressed as

$$\sigma_{ij} = \left(\dot{\Psi}_{\mathrm{P}} - 2\dot{\Psi}_{\mathrm{S}}\right) * \varepsilon_{kk}\delta_{ij} + 2\dot{\Psi}_{\mathrm{S}} * \varepsilon_{ij} \tag{2.6}$$

with the relaxation functions Ψ of the P- and S-waves (the dot denotes a time derivative and the asterisk a convolution)

$$\Psi_{\mathrm{P}}(t) = M\left(1 + \sum_{l=1}^{L}\left(\frac{\tau_{\varepsilon l}^{\mathrm{P}}}{\tau_{\sigma l}} - 1\right)e^{-t/\tau_{\sigma l}}\right)H(t) \tag{2.7}$$

$$\Psi_{\mathrm{S}}(t) = \mu\left(1 + \sum_{l=1}^{L}\left(\frac{\tau_{\varepsilon l}^{\mathrm{S}}}{\tau_{\sigma l}} - 1\right)e^{-t/\tau_{\sigma l}}\right)H(t) \tag{2.8}$$

where $\tau_{\sigma l}$ is the stress relaxation time and $\tau_{\varepsilon l}$ the strain retardation time for P- and S-waves of the lth Maxwell body of the GSLS. Instead of λ the P-wave modulus $M = \lambda + 2\mu$ is used and Equation 2.5 is formulated as

$$\frac{\partial \sigma_{ij}}{\partial t} = \left(M\left(1+\tau^{\mathrm{P}}\right) - 2\mu\left(1+\tau^{\mathrm{S}}\right)\right)\frac{\partial v_k}{\partial x_k}\delta_{ij} + \mu\left(1+\tau^{\mathrm{S}}\right)\left(\frac{\partial v_i}{\partial x_j} + \frac{\partial v_j}{\partial x_i}\right) + \sum_{l=1}^{L} r_{ijl} \tag{2.9}$$

$$\frac{\partial r_{ijl}}{\partial t} = -\frac{1}{\tau_{\sigma l}}\left(\left(M\tau^{\mathrm{P}} - 2\mu\tau^{\mathrm{S}}\right)\frac{\partial v_k}{\partial x_k}\delta_{ij} + \mu\tau^{\mathrm{S}}\left(\frac{\partial v_i}{\partial x_j} + \frac{\partial v_j}{\partial x_i}\right) + r_{ijl}\right) \tag{2.10}$$

with the memory variable r, $\tau^{\mathrm{P}} = \frac{\tau^{\mathrm{P}}_{\varepsilon l}}{\tau_{\sigma l}} - 1$, and $\tau^{\mathrm{S}} = \frac{\tau^{\mathrm{S}}_{\varepsilon l}}{\tau_{\sigma l}} - 1$. The quality factor Q is employed to specify a level of attenuation within the model space. It is defined by the loss of energy per propagation cycle $\left(Q = 2\pi\frac{E}{\delta E}\right)$ and is approximated with a least-squares approach for a specific frequency range by

$$Q_{\mathrm{P/S}}(\omega, \tau_{\sigma l}, \tau^{\mathrm{P/S}}) = \frac{1 + \sum\limits_{l=1}^{L} \frac{\omega^2\tau_{\sigma l}^2}{1+\omega^2\tau_{\sigma l}^2}\tau^{\mathrm{P/S}}}{\sum\limits_{l=1}^{L} \frac{\omega\tau_{\sigma l}}{1+\omega^2\tau_{\sigma l}^2}\tau^{\mathrm{P/S}}} \tag{2.11}$$

which is dependent on the angular frequency ω. In our approach, the relaxation frequencies $f_L = 2\pi/\tau_{\sigma l}$ are chosen such that Q is approximately constant over the frequency range under consideration.

2.1.3 Acoustic approximation

In media where no shear stresses act ($\mu = 0$), such as fluids and gases, wave propagation is described by an acoustic formulation which can be treated as an approximation to the elastic equations. The stress tensor simplifies to the scalar pressure p which is proportional to the trace of σ. The acoustic second-order wave equation for homogeneous density reads

$$\rho\frac{\partial^2 p}{\partial t^2} = K\nabla^2 p \tag{2.12}$$

with the bulk modulus $K = \lambda$ (elastic case: $K = \lambda + \frac{2}{3}\mu$). K denotes the necessary change in pressure to cause a specific change in volume of a certain medium. Equation 2.12 can be split into a system of first-order equations

$$\frac{\partial v_i}{\partial t} = \frac{1}{\rho}\frac{\partial p}{\partial x_i} \tag{2.13}$$

$$\frac{\partial p}{\partial t} = K\frac{\partial v_i}{\partial x_i} \tag{2.14}$$

which are the acoustic equivalents of Equations 2.1 and 2.5, respectively. Analogous to the elastic approach, attenuation of the P-waves can be incorporated in the acoustic scheme.

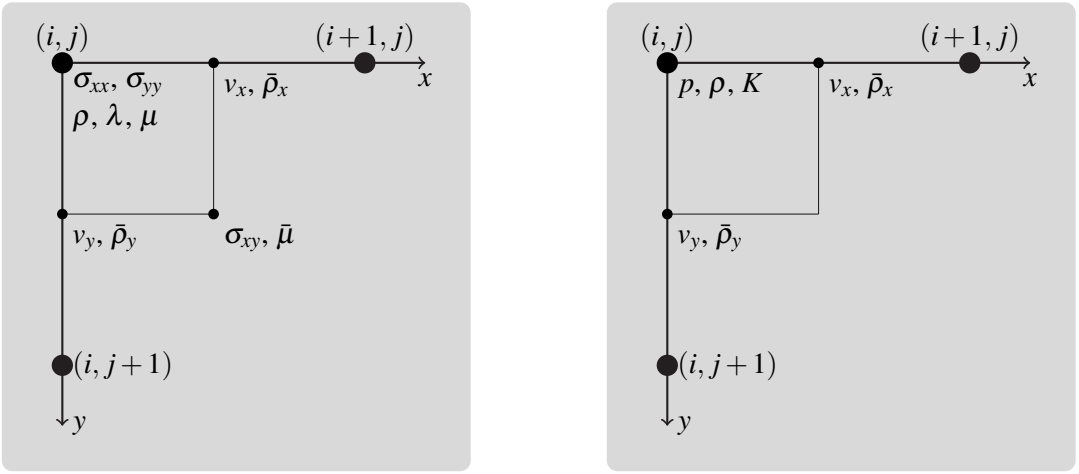

Figure 2.1: 2D standard staggered grid for an elastic (left) and an acoustic (right) medium.

2.1.4 Finite-difference solution

To simulate wave propagation within a discretized model a finite-difference (FD) solution to the underlying set of equations is chosen (e.g., Virieux, 1986). The partial derivatives applied to any continuous function f are approximated by the FD operators

$$\frac{\partial}{\partial x} f(x)|_i = \frac{f(i+\frac{1}{2}\Delta h) - f(i-\frac{1}{2}\Delta h)}{\Delta h} + \mathscr{O}(\Delta h^2) \tag{2.15}$$

$$\frac{\partial}{\partial t} f(t)|_n = \frac{f(n+\frac{1}{2}\Delta t) - f(n-\frac{1}{2}\Delta t)}{\Delta t} + \mathscr{O}(\Delta t^2) \tag{2.16}$$

where the spatial discretization is $x = i\Delta h$ and the temporal discretization $t = n\Delta t$. The subsurface model is described by the parameters λ, μ, and ρ for an elastic medium and K and ρ for an acoustic approach. Values of each parameter are stored at every point of a Cartesian grid. To increase the accuracy of the approximation a standard staggered grid (SSG) is used. Instead of storing all parameters on full grid points only, they are also distributed to half grid points. The SSGs for elastic and acoustic media for a 2D approach are shown in Figure 2.1. The density values at half grid points, $\bar{\rho}_x$, $\bar{\rho}_y$ are averaged from the two neighboring grid points in x and y direction, respectively. In the elastic case, values of the shear modulus at the corner of the cell shifted by a half grid point in each direction, $\bar{\mu}$, are calculated by the harmonic average of the values of the four neighboring grid points. The simulated seismic velocities v_i are stored at half grid points shifted in the respective direction. The pressure p in the acoustic case and the main components of the stress tensor σ_{ii} in the elastic case, are stored at full grid points and the mixed component of the stress tensor is stored at the same corner of the cell as $\bar{\mu}$.

In order to accurately calculate the evolution of a wavefield on an FD grid, criteria for spatial and temporal discretization need to be fulfilled. To guarantee the stability of the simulation the time step Δt needs to be smaller than the time the fastest wave needs to reach the next grid point (Courant-Friedrich-Levy condition). To avoid (i.e., keep minimal) numerical dispersion the spatial discretization needs to be a minimum number of grid points per smallest wavelength (Holberg, 1987). The smallest wavelength

is defined by the lowest wave velocity and the maximum frequency. Through an expansion of Equations 2.15 and 2.16 higher-order schemes can be realized. In this work I use operators of fourth order in space and second order in time.

As an initial condition it is assumed the medium is at rest so the particle velocities and the stresses (or the pressure) are zero at $t = 0$, as well as their first and second time derivatives. Special consideration has to be given to the model boundaries. At the top of the FD grid a free surface condition is applied, i.e. all normal stresses have to be zero. The mirroring technique suggested by Levander (1988) is implemented in the FD code used in this work. Additionally, boundary conditions are needed to suppress reflections from the model edges. Therefore, a coordinate stretch is applied near the lateral and bottom edges by a convolutional perfectly-matched layer (C-PML) approach which prevents the wavefields from reaching the model boundary (Komatitsch and Martin, 2007).

The source implementation is realized in two different approaches. The excitation of force sources is achieved by adding a scaled source signature to the velocity component. The excitation of explosive sources is applied to the stress tensor in the elastic case and to the pressure term in the acoustic case. A derivative in time is applied for the explosive sources, so that the signature is consistent for both source types (Groos, 2013).

2.2 Inversion

The theory of inverse problems is discussed in much detail in many publications, (e.g., Tarantola, 2005), here I give a short overview of the main approach used in this work. Due to the non-linearity of the inverse problem an iterative solution is adopted and a local optimization approach is chosen. This approach is computationally much more efficient for large-scale problems in contrast to global methods using a grid search. However, a priori knowledge is necessary to construct a starting model $\mathbf{m}_0$ which can already explain the measured data well before the inversion is started. In seismic inversion the starting model needs to provide synthetic data which match the recorded data within half a wavelength (cycle skip criterion, Virieux and Operto, 2009). A schematic overview of one iteration of the inversion process is given in Figure 2.2. The different steps of the inversion process are gradually introduced in the following sections.

As a general concept we assume that data $\mathbf{d}$ are obtained from a subsurface model $\mathbf{m}$ by a nonlinear operator g

$$\mathbf{d} = g(\mathbf{m}) \tag{2.17}$$

and the corresponding inverse problem is then denoted by

$$\mathbf{m} = g^{-1}(\mathbf{d}). \tag{2.18}$$

To quantify the discrepancy between the data calculated for an assumed model and the data measured in the field, a misfit or objective function is defined by

$$E(\mathbf{m}) = \frac{1}{2}\Delta\mathbf{d}^{\mathrm{T}}\Delta\mathbf{d} \tag{2.19}$$

which is an L_2-norm of the data residual $\Delta\mathbf{d}$. The residual is calculated from the measured or observed data $\mathbf{d}_{\mathrm{obs}}$ and data simulated for a given model $\mathbf{d}_{\mathrm{sim}}$ by

$$\Delta\mathbf{d}(\mathbf{m}) = \mathbf{d}_{\mathrm{obs}} - \mathbf{d}_{\mathrm{sim}}(\mathbf{m}). \tag{2.20}$$

To derive a correction to the current model $\mathbf{m}$ it is split into two parts, a model perturbation $\Delta\mathbf{m}$ and the unperturbed model $\mathbf{m}_0$

$$\mathbf{m} = \mathbf{m}_0 + \Delta\mathbf{m}. \tag{2.21}$$

A Taylor series expansion up to second-order accuracy is applied to the misfit of the model

$$E(\mathbf{m}_0 + \Delta\mathbf{m}) = E(\mathbf{m}_0) + \frac{\partial E(\mathbf{m}_0)}{\partial \mathbf{m}}\Delta\mathbf{m} + \frac{1}{2}\Delta\mathbf{m}^{\mathrm{T}}\frac{\partial^2 E(\mathbf{m}_0)}{\partial \mathbf{m}^2}\Delta\mathbf{m} + \mathscr{O}(\Delta\mathbf{m}^3) \tag{2.22}$$

so the minimum of the misfit function can be found by

$$\frac{\partial E(\mathbf{m})}{\partial \mathbf{m}} = \frac{\partial E(\mathbf{m}_0)}{\partial \mathbf{m}} + \frac{\partial^2 E(\mathbf{m}_0)}{\partial \mathbf{m}^2}\Delta\mathbf{m} \stackrel{!}{=} 0. \tag{2.23}$$

From Equation 2.23 the model perturbation or update is derived as

$$\Delta\mathbf{m} = -\underbrace{\left(\frac{\partial^2 E(\mathbf{m}_0)}{\partial \mathbf{m}^2}\right)^{-1}}_{\mathbf{H}}\frac{\partial E(\mathbf{m}_0)}{\partial \mathbf{m}}. \tag{2.24}$$

In order to decrease the misfit the model at iteration $n+1$ is acquired from the previous model $\mathbf{m}_n$ and the gradient of the misfit function $\frac{\partial E(\mathbf{m}_n)}{\partial \mathbf{m}_n}$

$$\mathbf{m}_{n+1} = \mathbf{m}_n - \mathbf{H}_n^{-1}\frac{\partial E(\mathbf{m}_n)}{\partial \mathbf{m}_n} \tag{2.25}$$

with the Hessian operator $\mathbf{H}$. This is called the Newton method.

As implied by Equation 2.24 the Hessian operator consists of second-order derivatives of the misfit function and is therefore computationally expensive to obtain. Therefore, Equation 2.25 is approximated by

$$\mathbf{m}_{n+1} = \mathbf{m}_n - \alpha_n\mathbf{P}_n\frac{\partial E(\mathbf{m}_n)}{\partial \mathbf{m}_n} \tag{2.26}$$

with the step length α and a preconditioning operator $\mathbf{P}$. By this simplification we lose information of the second-order derivatives which are beneficial for a successful convergence of the inversion. To mitigate this loss, often approximations to the Hessian, for example by its diagonal elements (Plessix and Mulder, 2004), are applied as a preconditioning.

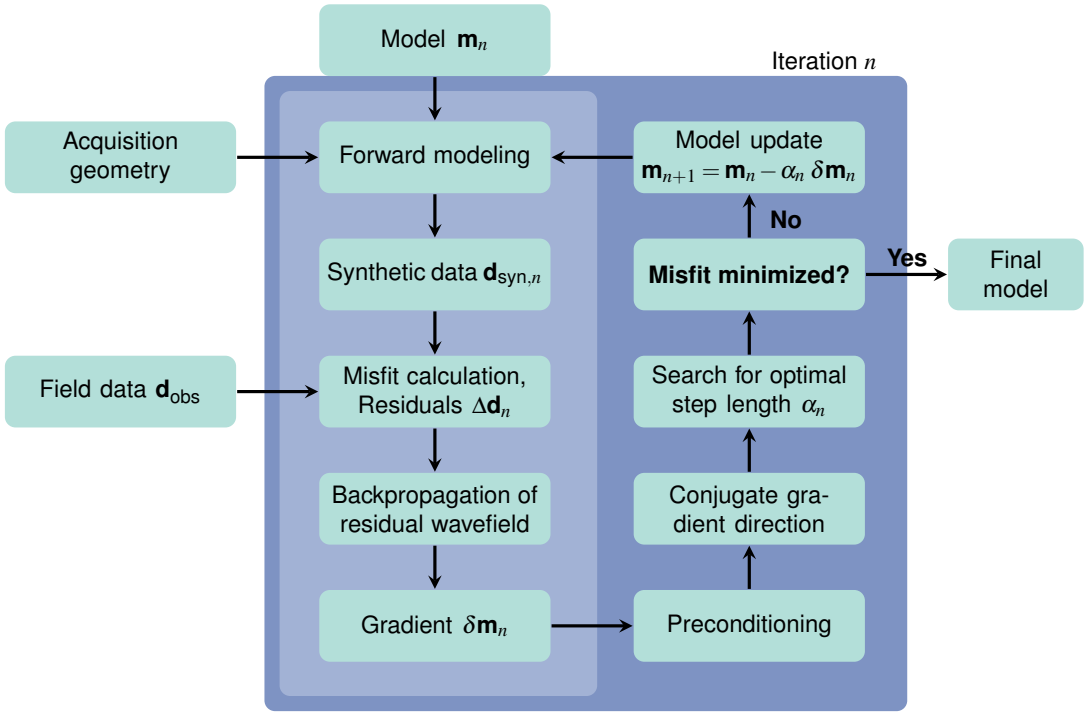

Figure 2.2: Simple scheme of the iterative FWI approach. The blue box shows all components of one iteration. The light blue box marks the steps that are applied for each source and a final gradient for each model parameter is computed by a sum over all shots.

2.2.1 Misfit definition

The L_2-misfit $E(\mathbf{m})$ for simulated seismic data of a certain model $\mathbf{m}$ is calculated by a sum over all sources s and receivers r and an integration over the whole recording time T

$$E(\mathbf{m}) = \sum_{s=1}^{n_{\mathrm{src}}} \sum_{r=1}^{n_{\mathrm{rec}}} \int_0^T \left(d_{\mathrm{obs}}\left(\mathbf{x}_s, \mathbf{x}_r, t\right) - d_{\mathrm{sim}}\left(\mathbf{x}_s, \mathbf{x}_r, \mathbf{m}, t\right) \right)^2 \mathrm{d}t. \tag{2.27}$$

Source and receiver positions are denoted by $\mathbf{x}_s$ and $\mathbf{x}_r$, respectively. A derivation of the misfit in Equation 2.27 yields

$$\frac{\partial E(\mathbf{m})}{\partial \mathbf{m}} = \sum_{s=1}^{n_{\mathrm{src}}} \sum_{r=1}^{n_{\mathrm{rec}}} \int_0^T -2 \left(d_{\mathrm{obs}}\left(\mathbf{x}_s, \mathbf{x}_r, t\right) - d_{\mathrm{sim}}\left(\mathbf{x}_s, \mathbf{x}_r, \mathbf{m}, t\right) \right) \frac{\partial d_{\mathrm{sim}}\left(\mathbf{x}_s, \mathbf{x}_r, \mathbf{m}, t\right)}{\partial \mathbf{m}} \mathrm{d}t. \tag{2.28}$$

Alternatively, an L_2-misfit of normalized seismograms can be defined, which was suggested by Choi and Alkhalifah (2012). Equation 2.27 then becomes

$$E(\mathbf{m}) = \sum_{s=1}^{n_{\mathrm{src}}} \sum_{r=1}^{n_{\mathrm{rec}}} \int_0^T \left(\frac{d_{\mathrm{obs}}\left(\mathbf{x}_s, \mathbf{x}_r, t\right)}{d_{\mathrm{obs,rms}}} - \frac{d_{\mathrm{sim}}\left(\mathbf{x}_s, \mathbf{x}_r, \mathbf{m}, t\right)}{d_{\mathrm{syn,rms}}} \right)^2 \mathrm{d}t \tag{2.29}$$

with

$$d_{\mathrm{rms}} = \left(\frac{1}{T} \int_0^T d^2(\mathbf{x}_s, \mathbf{x}_r, t) \mathrm{d}t \right)^{1/2}. \tag{2.30}$$

The normalization of seismograms is sensible for field data where the physical amplitude of the source signal is often not well enough known to match it within the simulation. Also the amplitude loss over distance might not be fitted by the simulation when effects such as anelasticity or signal conversion are not properly accounted for. The normalization is therefore a measure to mitigate simplifications in the physical assumptions. Furthermore, it reduces the influence of geometrical amplitude loss and allows far-offset data to equally contribute to the misfit. A drawback of this approach is that the sensitivity for a potential inversion for attenuation is reduced.

2.2.2 Adjoint gradients

To derive gradients for a set of initial model parameters a framework is needed which allows to transfer the differences in the observed and simulated data to their origin in the model space. Therefore, we use the concept of adjoint kernels with which data and model space are linked (e.g., Köhn, 2011).

If $\frac{\partial \mathbf{d}}{\partial \mathbf{m}}$, which is called Frechét derivative, is known, we can integrate over all model changes within the volume V by

$$\delta \mathbf{d}(\mathbf{x}_r, t) = \int_V \mathrm{d}V \frac{\partial \mathbf{d}(\mathbf{x}_r, t)}{\partial \mathbf{m}} \delta \mathbf{m} \tag{2.31}$$

to find the perturbation in the data space $\delta \mathbf{d}$. Vice versa by

$$\delta \mathbf{m} = \int \mathrm{d}t \sum_{r=1}^{n_{\mathrm{rec}}} \frac{\partial \mathbf{d}(\mathbf{x}_r, t)}{\partial \mathbf{m}}^{*} \delta \mathbf{d}(\mathbf{x}_r, t) \tag{2.32}$$

all changes in the data space can be integrated to find the corresponding model perturbation. Note that the terms $\delta \mathbf{m}$ and $\delta \mathbf{d}$ are not identical in Equations 2.31 and 2.32. Here, the asterisk indicates that the term in Equation 2.32 is the adjoint to the equivalent term in Equation 2.31. If we consider Equations 2.31 and 2.32 to be linear operations, $\frac{\partial \mathbf{d}}{\partial \mathbf{m}} = \frac{\partial \mathbf{d}}{\partial \mathbf{m}}^{*}$ (Tarantola, 2005).

To derive the adjoint gradients for the inversion of seismic data we start with the elastic wave equation, parameterized in terms of the ground displacement u

$$\rho \frac{\partial^2 u_i}{\partial t^2} = \frac{\partial \sigma_{ij}}{\partial x_j} + f_i \tag{2.33}$$

and the stress-strain relationship (Eq. 2.2). Perturbations are introduced to the following terms

$$u_i \rightarrow u_i + \delta u_i \tag{2.34}$$

$$\rho \rightarrow \rho + \delta \rho \tag{2.35}$$

$$C_{ijkl} \rightarrow C_{ijkl} + \delta C_{ijkl} \tag{2.36}$$

$$\sigma_{ij} \rightarrow \sigma_{ij} + \delta \sigma_{ij} \tag{2.37}$$

$$\varepsilon_{kl} \rightarrow \varepsilon_{kl} + \delta \varepsilon_{kl} \tag{2.38}$$

and are inserted in Equations 2.33 and 2.2. This yields

$$(\rho+\delta\rho)\frac{\partial^2(u_i+\delta u_i)}{\partial t^2}=\frac{\partial(\sigma_{ij}+\delta\sigma_{ij})}{\partial x_j}+f_i \tag{2.39}$$

and

$$\sigma_{ij}+\delta\sigma_{ij}=(C_{ijkl}+\delta C_{ijkl})(\varepsilon_{kl}+\delta\varepsilon_{kl}). \tag{2.40}$$

New body and surface source terms are defined by

$$\Delta f_i=-\delta\rho\frac{\partial^2 u_i}{\partial t^2} \tag{2.41}$$

and

$$\Delta T_{ij}=\delta C_{ijkl}\varepsilon_{kl} \tag{2.42}$$

which simplifies to

$$\Delta T_{ij}=\delta_{ij}\varepsilon_{kk}\delta\lambda+(\varepsilon_{ij}+\varepsilon_{ji})\delta\mu=\delta_{ij}\frac{\partial u_k}{\partial x_k}\delta\lambda+\left(\frac{\partial u_i}{\partial x_j}+\frac{\partial u_j}{\partial x_i}\right)\delta\mu \tag{2.43}$$

for an isotropic medium. A data perturbation then results from the new source terms, which are called secondary or *adjoint sources*. Equations 2.33 and 2.2 then read

$$\rho\frac{\partial^2 u_i}{\partial t^2}=\frac{\partial\sigma_{ij}}{\partial x_j}+\Delta f_i \tag{2.44}$$

and

$$\sigma_{ij}=C_{ijkl}\varepsilon_{kl}+\Delta T_{ij}. \tag{2.45}$$

A solution to Equation 2.44 can be found in terms of Green's functions G_{ij} (Aki and Richards, 2002)

$$\delta u_i(\mathbf{x}_r,t)=\int_V \mathrm{d}V\, G_{ij}(\mathbf{x}_r,t;\mathbf{x},0)*\Delta f_j(\mathbf{x},t)-\int_V \mathrm{d}V\frac{\partial G_{ij}(\mathbf{x}_r,t;\mathbf{x},0)}{\partial \mathbf{x}_k}*\Delta T_{jk}(\mathbf{x},t). \tag{2.46}$$

Here the sum over all shots for the seismic problem is neglected for the sake of clarity. Substitution of Equations 2.41 and 2.43 into Equation 2.46 yields

$$\delta u_i(\mathbf{x}_r,t)=-\int_V \mathrm{d}V\frac{\partial G_{ij}(\mathbf{x}_r,t;\mathbf{x},0)}{\partial t}*\frac{\partial u_j(\mathbf{x},t)}{\partial t}\delta\rho \tag{2.47}$$

$$-\int_V \mathrm{d}V\frac{\partial G_{ij}(\mathbf{x}_r,t;\mathbf{x},0)}{\partial \mathbf{x}_j}*\frac{\partial u_m(\mathbf{x},t)}{\partial x_m}\delta\lambda \tag{2.48}$$

$$-\int_V \mathrm{d}V\frac{\partial G_{ij}(\mathbf{x}_r,t;\mathbf{x},0)}{\partial \mathbf{x}_k}*\left(\frac{\partial u_k(\mathbf{x},t)}{\partial x_j}+\frac{\partial u_j(\mathbf{x},t)}{\partial x_k}\right)\delta\mu. \tag{2.49}$$

Here, we apply the following convolution theorem to the first term

$$\frac{\partial f(\mathbf{x},t)}{\partial t}*g(\mathbf{x},t)=f(\mathbf{x},t)*\frac{\partial g(\mathbf{x},t)}{\partial t}. \tag{2.50}$$

The corresponding adjoint expressions for the elastic model parameters λ, μ and ρ are

$$\delta\lambda(\mathbf{x}) = -\int \mathrm{d}t \sum_r \frac{\partial G_{ij}(\mathbf{x}_r,t;\mathbf{x},0)}{\partial \mathbf{x}_j} * \frac{\partial u_m(\mathbf{x},t)}{\partial x_m} \delta u_i(\mathbf{x}_r,t) \tag{2.51}$$

$$\delta\mu(\mathbf{x}) = -\int \mathrm{d}t \sum_r \frac{\partial G_{ij}(\mathbf{x}_r,t;\mathbf{x},0)}{\partial \mathbf{x}_k} * \left(\frac{\partial u_k(\mathbf{x},t)}{\partial x_j} + \frac{\partial u_j(\mathbf{x},t)}{\partial x_k} \right) \delta u_i(\mathbf{x}_r,t) \tag{2.52}$$

$$\delta\rho(\mathbf{x}) = -\int \mathrm{d}t \sum_r \frac{\partial G_{ij}(\mathbf{x}_r,t;\mathbf{x},0)}{\partial t} * \frac{\partial u_j(\mathbf{x},t)}{\partial t} \delta u_i(\mathbf{x}_r,t). \tag{2.53}$$

To derive the elastic gradients we define the adjoint wavefield

$$\Psi_j(\mathbf{x},t) = \sum_r G_{ij}(\mathbf{x},-t;\mathbf{x}_r,0) * \delta u_i(\mathbf{x}_r,t). \tag{2.54}$$

and make use of the reciprocity of the Green's function expressed by

$$G_{ij}(\mathbf{x}_r,t;\mathbf{x},0) = G_{ij}(\mathbf{x},t;\mathbf{x}_r,0). \tag{2.55}$$

Furthermore, the following convolution and integration theorems are applied

$$\int \mathrm{d}t f(\mathbf{x},t) g(\mathbf{x},t) = \int \mathrm{d}t f(\mathbf{x},-t) g(\mathbf{x},-t), \tag{2.56}$$

and

$$\int \mathrm{d}t (f(\mathbf{x},t) * g(\mathbf{x},t)) h(\mathbf{x},t) = \int \mathrm{d}t f(\mathbf{x},-t) (g(\mathbf{x},t) * h(\mathbf{x},-t)). \tag{2.57}$$

Equation 2.54 implies that a time reversal is introduced, therefore commonly the term *backpropagation* is used when describing the calculation of the adjoint wavefield.

By this the gradients for the parameters λ, μ and ρ can be obtained

$$\frac{\partial E(\mathbf{m})}{\partial \lambda(\mathbf{x})} = \delta\lambda(\mathbf{x}) = -\int \mathrm{d}t \frac{\partial u_m(\mathbf{x},t)}{\partial x_m} \frac{\partial \Psi_j(\mathbf{x},t)}{\partial x_j} \tag{2.58}$$

$$\frac{\partial E(\mathbf{m})}{\partial \mu(\mathbf{x})} = \delta\mu(\mathbf{x}) = -\int \mathrm{d}t \left(\frac{\partial u_j(\mathbf{x},t)}{\partial x_k} + \frac{\partial u_k(\mathbf{x},t)}{\partial x_j} \right) \frac{\partial \Psi_j(\mathbf{x},t)}{\partial x_k} \tag{2.59}$$

$$\frac{\partial E(\mathbf{m})}{\partial \rho(\mathbf{x})} = \delta\rho(\mathbf{x}) = -\int \mathrm{d}t \frac{\partial u_j(\mathbf{x},t)}{\partial t} \frac{\partial \Psi_j(\mathbf{x},t)}{\partial t}. \tag{2.60}$$

A comparison of the resulting gradients with Equation 2.28 shows that the adjoint sources are related to the data residuals and the misfit definition.

The final step is the derivation for a parametrization in terms of the seismic velocities

$$v_\mathrm{P} = \sqrt{\frac{\lambda + 2\mu}{\rho}} \qquad \text{and} \qquad v_\mathrm{S} = \sqrt{\frac{\mu}{\rho}} \tag{2.61}$$

yielding by an application of the chain rule

$$\frac{\partial E(\mathbf{m})}{\partial v_\mathrm{P}(\mathbf{x})} = 2\rho(\mathbf{x})v_\mathrm{P}(\mathbf{x})\frac{\partial E(\mathbf{m})}{\partial \lambda(\mathbf{x})} \tag{2.62}$$

$$\frac{\partial E(\mathbf{m})}{\partial v_\mathrm{S}(\mathbf{x})} = -4\rho(\mathbf{x})v_\mathrm{S}(\mathbf{x})\frac{\partial E(\mathbf{m})}{\partial \lambda(\mathbf{x})} + 2\rho(\mathbf{x})v_\mathrm{S}(\mathbf{x})\frac{\partial E(\mathbf{m})}{\partial \mu(\mathbf{x})} \tag{2.63}$$

$$\frac{\partial E(\mathbf{m})}{\partial \rho_v(\mathbf{x})} = \left(v_\mathrm{P}(\mathbf{x})^2 - 2v_\mathrm{S}(\mathbf{x})^2\right)\frac{\partial E(\mathbf{m})}{\partial \lambda(\mathbf{x})} + v_\mathrm{S}(\mathbf{x})^2\frac{\partial E(\mathbf{m})}{\partial \mu(\mathbf{x})} + \frac{\partial E(\mathbf{m})}{\partial \rho(\mathbf{x})}. \tag{2.64}$$

2.2.3 Steplength estimation

The inversion is executed until the misfit can no longer be decreased significantly. Within each iteration of the inversion process the resulting gradients are applied to the corresponding parameter models with an appropriate step length. A scaling of the gradients with the maximum of each model parameter is applied to ensure a decoupling within the update (Groos, 2013).

The optimal step length α is estimated from a predefined number of test step lengths α_test by a parabolic line search to find the highest misfit reduction from the misfit calculated for each α_test (Kurzmann, 2012).

If the step length estimation fails, i.e. no step length is found which further reduces the misfit, the inversion process is ended.

2.2.4 Conjugate-gradient approach

To improve the convergence of the local optimization scheme a conjugate-gradient approach is utilized (Nocedal and Wright, 2006). It is meant to ensure a smooth convergence which takes the information of the previous gradient into account such that a strong variation of the gradient direction between successive iterations is prevented.

The model update (Eq. 2.26) is modified by the conjugate gradient direction $\delta\mathbf{c}$

$$\mathbf{m}_{n+1} = \mathbf{m}_n + \alpha\delta\mathbf{c}_n \tag{2.65}$$

with

$$\delta\mathbf{c}_n = \delta\mathbf{m}_n + \beta_n\delta\mathbf{c}_{n-1} \tag{2.66}$$

for $n > 1$ with the preconditioned gradient $\delta\mathbf{m} = \mathbf{P}\frac{\partial E(\mathbf{m})}{\partial \mathbf{m}}$. At the first iteration $\delta\mathbf{c}_1 = \delta\mathbf{m}_1$. The Polak-Ribiére coefficient β (Nocedal and Wright, 2006) which is used as a weighting factor is defined as

$$\beta_n^{PR} = \frac{\delta\mathbf{m}_n^\mathrm{T}(\delta\mathbf{m}_n - \delta\mathbf{m}_{n-1})}{\delta\mathbf{m}_{n-1}^\mathrm{T}\delta\mathbf{m}_{n-1}} \tag{2.67}$$

and for the conjugate-gradient scheme we use $\beta_n = \max[0, \beta_n^{PR}]$.

2.3 Data preparation

For field data inversion further steps are necessary to increase the match between measured and simulated data. This includes the transformation of the data to match the output of the simulation algorithm which considers only the propagation of seismic waves in a 2D plane. Furthermore, the characteristic signal content of the seismic source needs to be approximated in order to separate effects of the source signature from signals from the subsurface.

2.3.1 3D-to-2D transformation

So far all derivations are valid for an arbitrary number of spatial dimensions (1…3). Typically, seismic data is acquired along a line leading to a two-dimensional geometry. To save calculation time usually the third dimension is neglected. Therefore, a transformation is necessary to adapt the measured data to these circumstances. The 3D-to-2D transformation for reflected waves as described in Forbriger et al. (2014) consists of two factors F. A convolution of the data with

$$F_{\mathrm{ph}} = \frac{1}{\sqrt{t}} \tag{2.68}$$

matches the phase shift, and a multiplication with

$$F_{\mathrm{amp}} = v_{\mathrm{ph}}\sqrt{2t} \tag{2.69}$$

corrects the amplitudes of the seismic traces.

2.3.2 Source time function inversion

To calculate synthetic data it is necessary to assume a source wavelet f_{stf} which is applied at all source positions. The signals emitted by seismic sources have a characteristic shape and frequency content which is ideally the same over all recorded shots. In field data applications the true source time function (STF) is not known or can only be calculated from a synthetic model. Pratt (1999) suggests to treat the inversion for the STF as a further least-squares optimization problem.

The source signature is obtained by deconvolution of the recorded field data with the synthetic seismograms which corresponds to a division in the frequency domain. It is assumed that the underlying model for the calculation is similar to the true subsurface and the signal difference is attributed to the difference in source signature only. To stabilize the deconvolution Groos et al. (2014) introduce a water-level term which prevents a division by zero.

A correction filter is derived at the beginning of each frequency stage and is therefore adjusted to the model changes already introduced by the inversion.

3 Synthetic study

The application of FWI to field data is a costly process in terms of finding a suitable strategy to obtain the best result. Furthermore, it is necessary to check the feasibility of FWI and the quality of its results for a given survey geometry and data availability. The design of a suitable "toy" or synthetic example is helpful to investigate the limits of a chosen approach. For the setting of hydrate and gas occurrence in a marine environment imaged by an OBS geometry, I choose a simple model with 1.5 km water depth and a constant gradient underneath which includes a BSR signature (increasing hydrate over decreasing gas content) at 400 m below seafloor (mbsf). The hydrate content in this example effects the P- and S-wave velocities, while no change in density is assumed. Density and P-wave velocity are altered by the gas content but no changes to the S-wave velocity are introduced. Typical values of sediment constituents (here quartz, clay, and water) as well as parameters for hydrate and gas are given in Table 3.1.

In the v_P model the maximum velocity above the BSR is 1995 m/s compared to 1700 m/s below, with a velocity of 1840 m/s at BSR depth. The S-wave velocity is 610 m/s at BSR depth and increases up to 795 m/s above. The density value drops from 1850 kg/m^3 at BSR depth to 1800 kg/m^3 below. The parameter distribution is shown in Figure 3.1 with the chosen starting models. One starting model per parameter reflects the background gradient and one homogeneous model each is chosen to examine how the resolution is affected by an insufficient starting model for this parameter. The model dimensions are 12 km in length and 3 km in depth.

For information on the discretization and computing times see Appendix B.1 which also provides details on the chosen parameters for the step length estimation und model parameter limits during the inversion. Each inversion was run for 10 hours on 80 cores.

The seismograms corresponding to the synthetic example are omitted here due to the fact that they can be fitted with no visible discrepancy by all approaches.

Table 3.1: Elastic parameters of sediment constituents after Carcione and Tinivella (2000), Helgerud et al. (2000), Waite et al. (2009) and references therein. Parameters for clay and quartz are taken from Helgerud et al. (2000), values of v_P and v_S from Waite et al. (2009).

	K (GPa)	G (GPa)	ρ (kg/m^3)	v_P (m/s)	v_S (m/s)
Water	2.25	0	1020	1484	0
Methane gas	0.11	0	230	412	0
Methane hydrate	8.27	3.39	920	3770	1960
Quartz	36.6	45	2650	6040	4120
Clay	20.9	6.85	2580	3410	1630

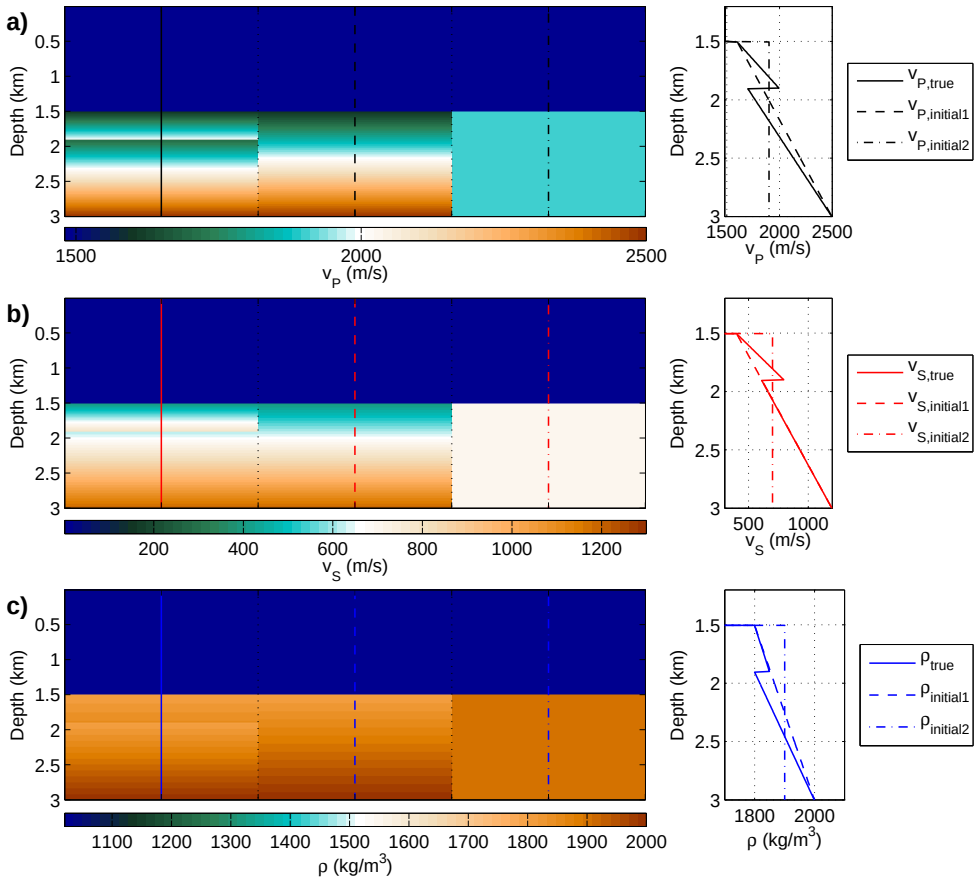

Figure 3.1: Parameter models of (a) P-wave velocity, (b) S-wave velocity, and (c) density.

3.1 Inversion setup

The geometry consists of 5 OBS stations which act as sources due to the reciprocal approach, placed at the seafloor with 1 km separation from 4 km to 8 km profile distance and 111 receivers below the sea surface with 100 m separation starting at 0.5 km profile distance. To simulate pseudo-field data, I apply elastic modeling to the synthetic BSR model and select a total recording time of 6 s. Signals are excited at 4 Hz center frequency with an explosive source signature and data are recorded as pressure at the receivers. I choose a simple L_2-norm without normalization of the data to quantify the misfit between modeled and pseudo-field data and apply a taper to prohibit updates in the water column.

The sensitivity for each parameter with different combinations of starting models is investigated with a focus on the v_P model which also exhibits the strongest parameter variation at BSR depth. All parameters are inverted for simultaneously. In a first step different v_S models are used to evaluate their effect on the inversion of v_P and determine if an additional inversion for v_S at the BSR is possible. In marine studies elastic effects are usually neglected but through the utilization of OBS stations converted shear waves are recorded. In the hydrophone data these waves are only recorded indirectly through another conversion at the seafloor and therefore with lower amplitude. Because of that I expect the v_S model to mainly affect the quality of the v_P recovery and not represent a further interpretable parameter model. The influence of the ρ model mainly concerns the amplitude of the reflections from the layer interfaces and is usually the model parameter which incorporates missing physical information from other parameters.

Furthermore, the effect of the geometry is evaluated as well as the influence of the application of a time window as suggested for the field data. As a reference inversion result the gradient starting model in each parameter class with inversion for v_P only is chosen.

3.2 Parameter sensitivity

To compare the inversion results final parameter models are shown, as well as the mean inverted parameter distribution with depth (averaged over the whole profile distance) to give an impression on the general resolution. For the evaluation of how well the BSR parameter contrast in v_P is resolved, I plot the reconstructed velocity maximum above the BSR as a blue line and the minimum below as a red line over all distances.

3.2.1 S-wave velocity

At first, the S-wave velocity is treated as a passive parameter and the resulting P-wave velocity distribution from monoparameter inversion is compared in Figure 3.2. For reference an inversion with the true v_S model (Fig. 3.2a) is shown as well as the result of a pseudo-acoustic inversion where v_S is set to 0. The BSR v_P distribution is resolved between 2 km and 10 km profile distance independent of the setup of the inversion although with varying quality. As expected, the BSR contrast in v_P is resolved well when using the true v_S model. For the gradient v_S starting model (Fig. 3.2b) the resolution is slightly reduced and some horizontal parameter fluctuations become visible which are symmetric about the source positions. These artifacts become much more pronounced when a homogeneous v_S starting model is used (Fig. 3.2c). With a pseudo-acoustic approach (Fig. 3.2d) the result is comparable to the inversion with the gradient v_S starting model with stronger artifacts around the source positions.

The quality of the resulting v_P models can be compared well when looking at the maximum and minimum velocities above and below the BSR, respectively (Figure 3.3). For the true v_S starting model (Figure 3.3a) the v_P maximum and minimum can be resolved with fluctuations of approximately 50 m/s. A slight overestimation of the maximum, and an underestimation of the minimum is visible. The resulting v_P maximum and minimum with the gradient v_S starting model (Figure 3.3b) exhibits v_P fluctuations of up to 100 m/s with a slight overestimation of the minimum v_P. For a homogeneous v_S starting model (Figure 3.3c) the v_P parameter fluctuations are approximately 150 m/s and a strong underestimation of the maximum v_P values results from the inappropriate v_S model.

When additionally an inversion for the v_S distribution is applied for the gradient and the homogeneous starting models, only very small updates are determined in the v_S model (Figure 3.4). For the gradient v_S starting model a small parameter contrast is determined at BSR depth which cannot be related to the true parameter distribution. In the homogeneous model some parameter changes can be observed close to the seafloor but no meaningful updates are introduced at BSR depth. All in all, a slight improvement can be observed in the resolved v_P parameter distribution (compare Figure 3.5), and the misfit can be decreased further than without inversion for v_S.

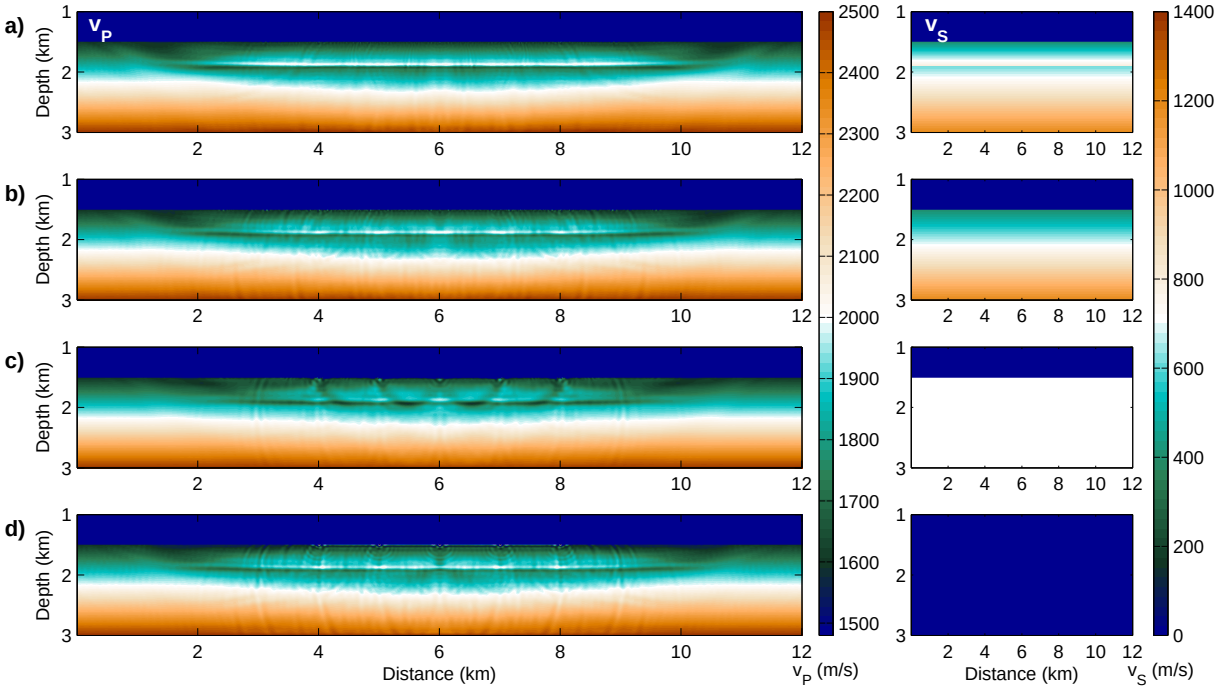

Figure 3.2: Reconstructed v_P models (left) for different v_S starting models (right). (a) True, (b) gradient, (c) homogeneous v_S model, (d) pseudo-acoustic inversion with $v_S = 0$.

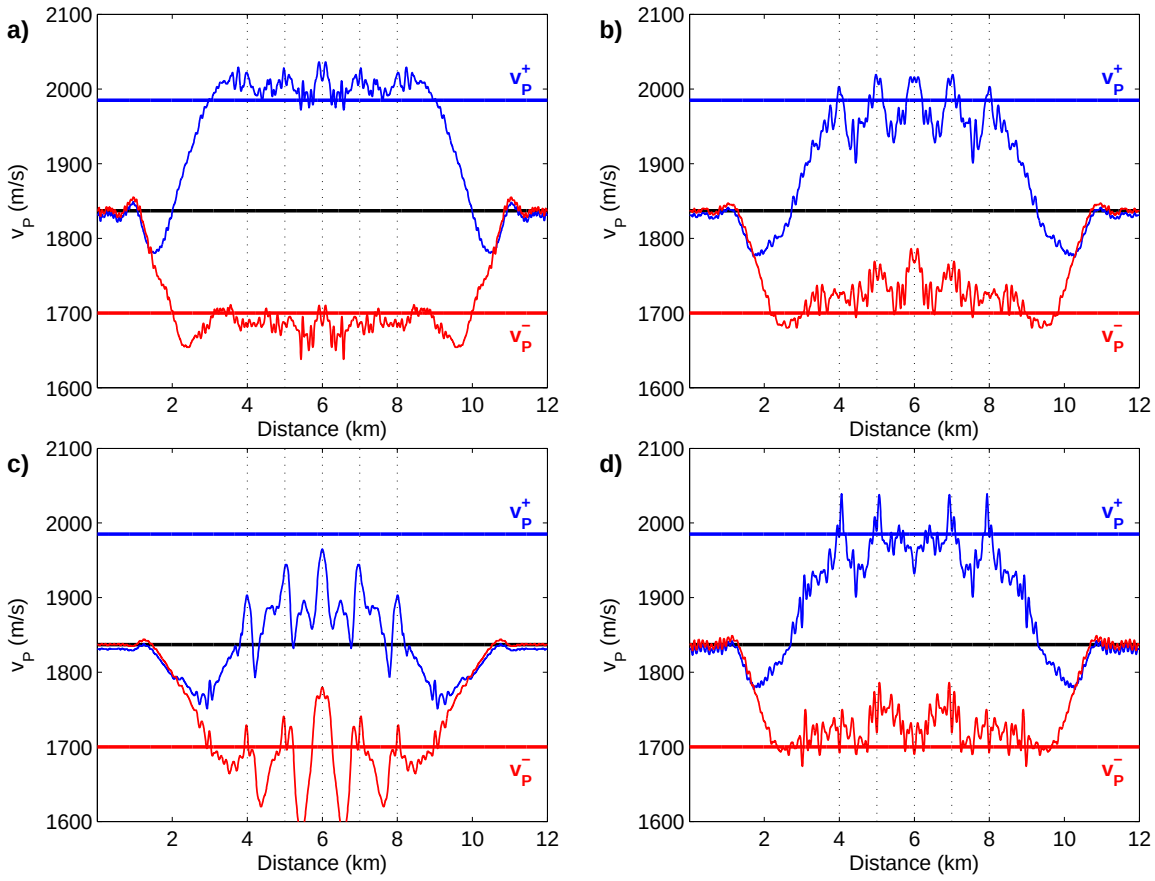

Figure 3.3: Resolution of the BSR contrast in v_P for different v_S starting models. (a) True, (b) gradient, (c) homogeneous v_S starting model, (d) pseudo-acoustic inversion with $v_S = 0$. The vertical dotted lines mark the locations of the OBS stations.

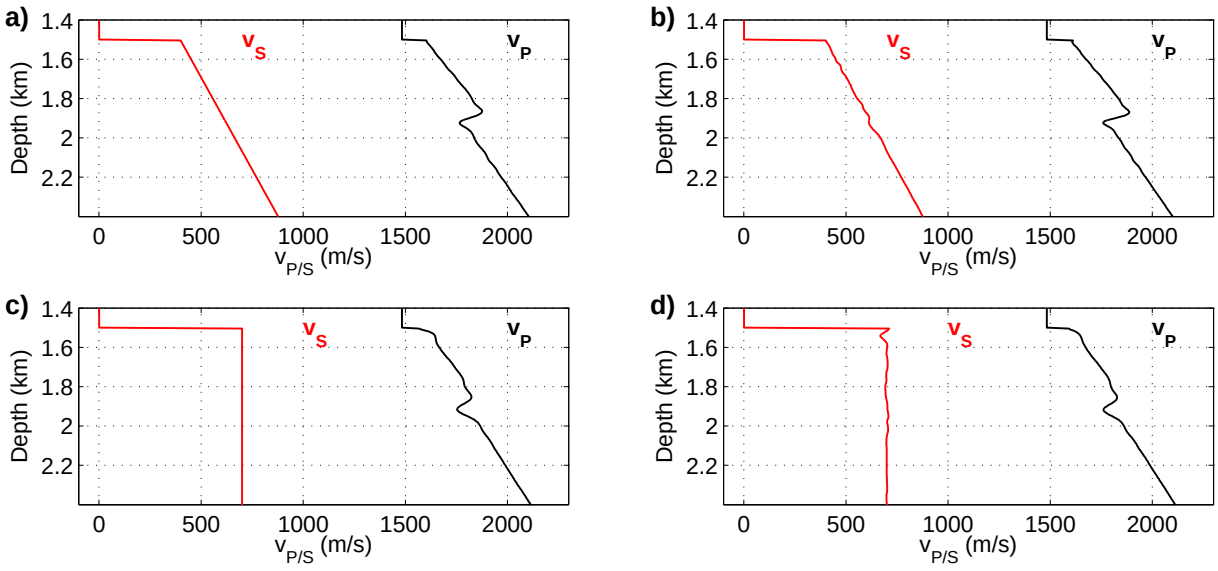

Figure 3.4: Mean v_P and v_S depth distribution for gradient, (a) and (b), and homogeneous, (c) and (d), v_S starting models with additional inversion for v_S applied in (b) and (d).

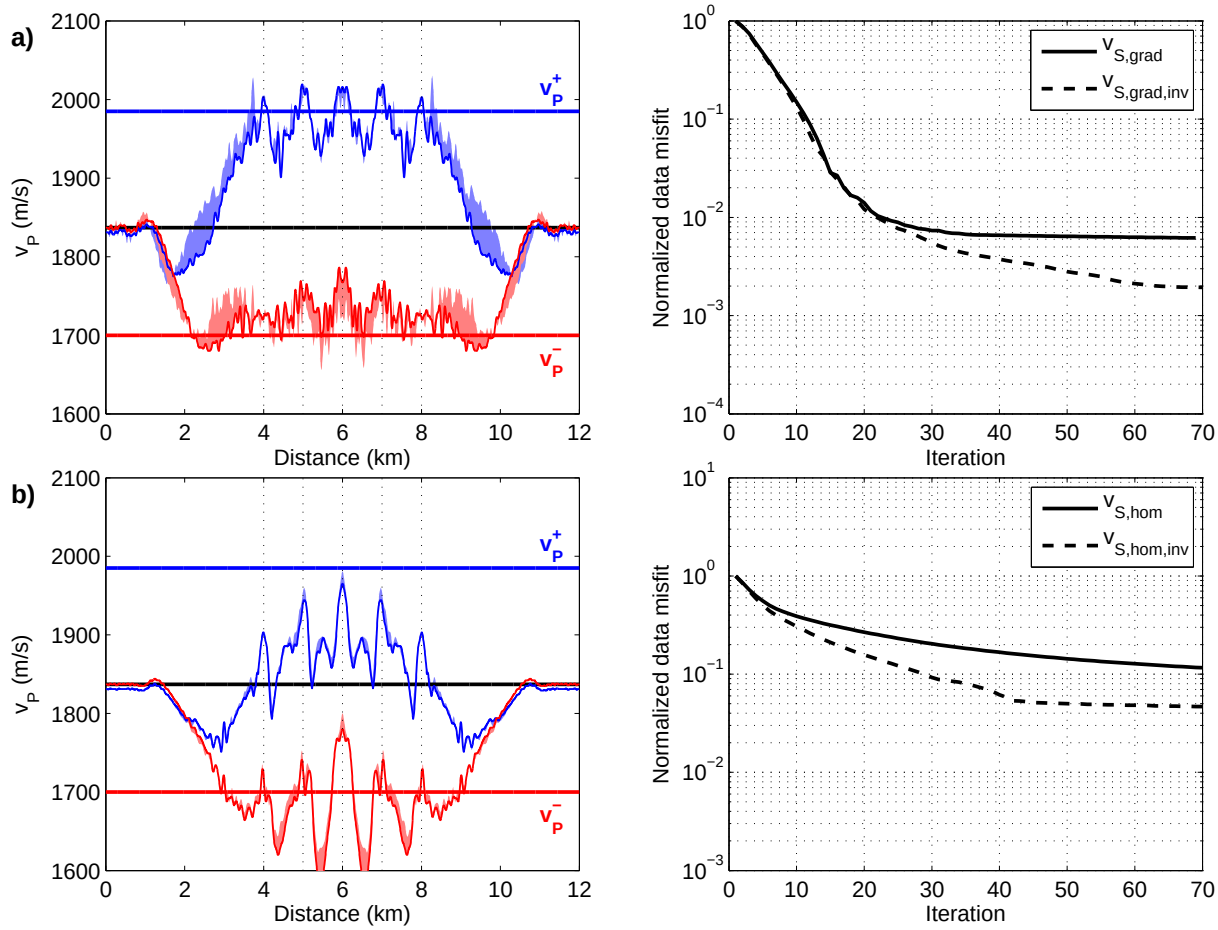

Figure 3.5: Comparison of the resolution of the BSR v_P distribution for different v_S starting models with and without inversion for v_S. (a) Gradient, (b) homogeneous v_S starting models. The shaded area in the left plots shows the difference when applying inversion for v_S (solid blue and red lines: without inversion for v_S). The vertical dotted lines mark the locations of the OBS stations. On the right, the misfit evolution corresponding to each test is shown.

3.2.2 Density

From field measurements density information can only be gathered by probing of the subsurface but usually its distribution is approximated from the P-wave velocity by empirical relations. In marine FWI applications density is either kept constant for all iterations or updated by a relation based on the v_P update. Independent inversion of the density is applied to mitigate missing information for example by neglect of S-wave propagation in the acoustic approximation. Here, I compare results for an inversion of the P-wave velocity distribution with a gradient and a homogeneous density model, with and without an additional inversion for density.

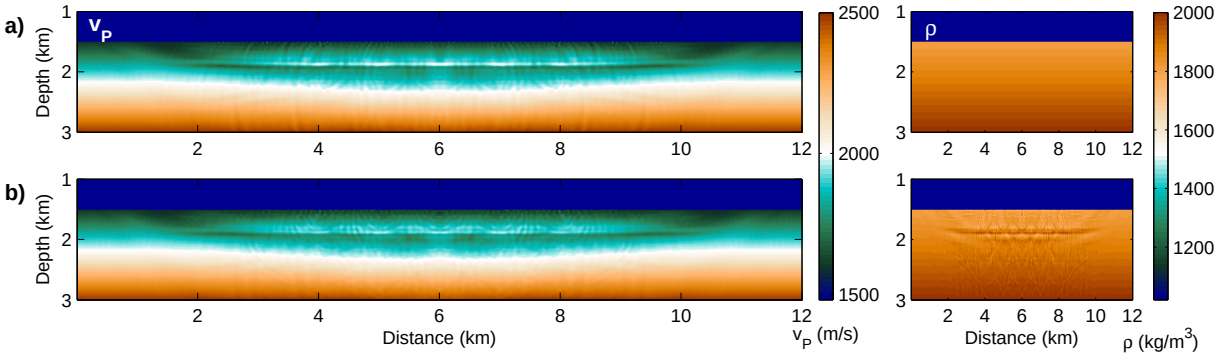

Figure 3.6: Reconstructed v_P models (left) for a gradient ρ starting model, (a) without and (b) with inversion for ρ (right).

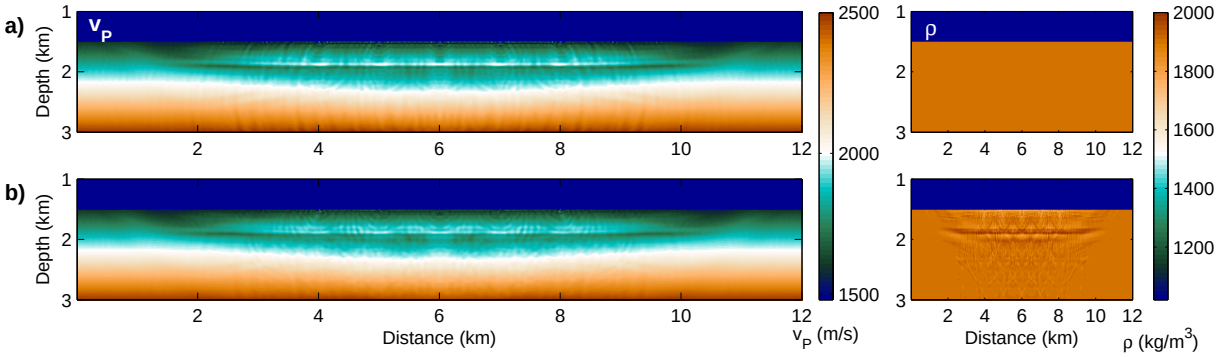

Figure 3.7: Reconstructed v_P models (left) for a homogeneous ρ starting model, (a) without and (b) with inversion for ρ (right).

The resulting P-wave distributions from inversion with the gradient and homogeneous density starting models are very similar in both cases, with and without density inversion (compare Figures 3.6 and 3.7). The main differences are stronger parameter fluctuations in v_P close to the seafloor for the homogeneous density starting model which are reduced when additional inversion for the density distribution is applied (compare Figure 3.8). Additional inversion for density has the main effect that the resolved BSR parameter contrast in v_P is decreased and a similar contrast is introduced in the density model (cross-talk). The introduced parameter contrast in ρ is approximately 60 kg/m^3. The contrast in v_P is decreased by roughly 60 m/s. A comparison of the resolved v_P contrast with and without density inversion is shown in Figure 3.9. The resolution of the v_P contrast is clearly reduced by the additional inversion for ρ. However, the misfit is reduced stronger when additional ρ inversion is applied.

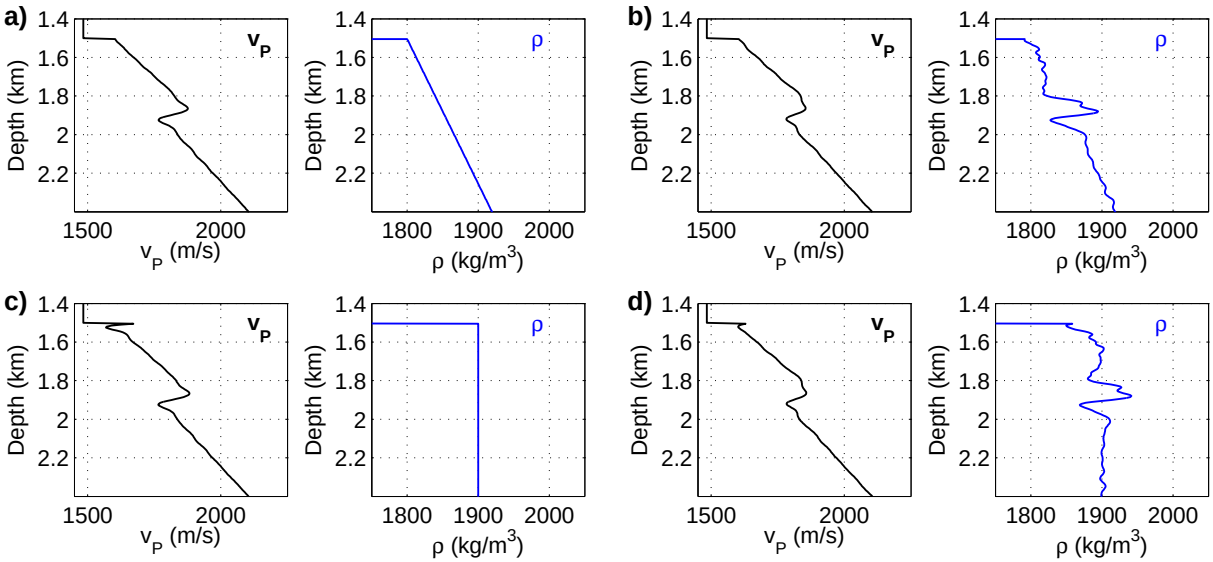

Figure 3.8: Mean v_P and ρ depth distribution for gradient, (a) and (b), and homogeneous, (c) and (d), ρ starting models with additional inversion for ρ applied in (b) and (d).

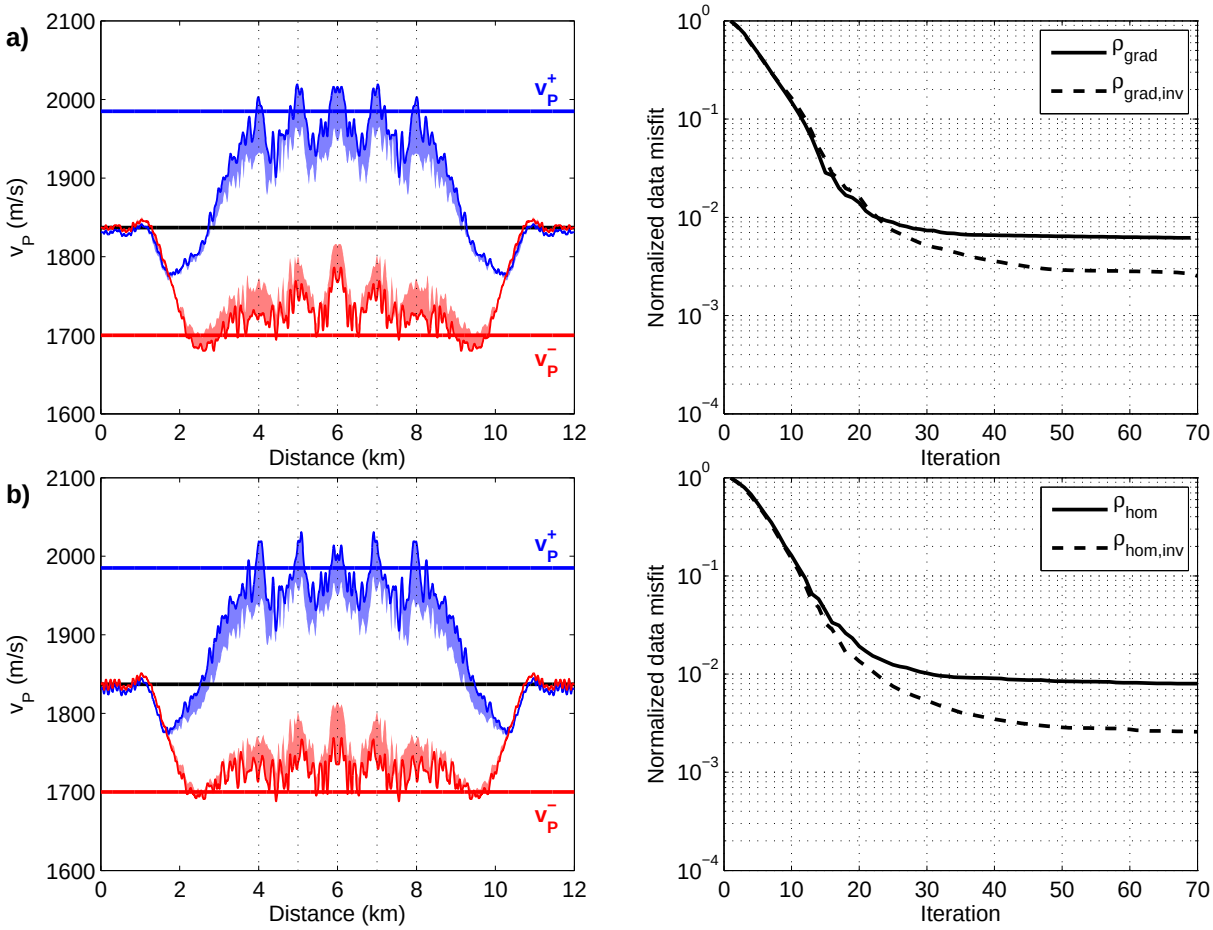

Figure 3.9: Comparison of the resolution of the BSR v_P distribution for different ρ starting models with and without inversion for ρ. (a) Gradient, (b) homogeneous ρ starting models. The shaded area in the left plots shows the difference when applying inversion for ρ (solid blue and red lines: without inversion for ρ). The vertical dotted lines mark the locations of the OBS stations. On the right, the misfit evolution corresponding to each test is shown.

3.2.3 P-wave velocity

So far sensitivity tests confirmed that the P-wave velocity can be resolved well when the v_S distribution is roughly known and independent of the density starting model. Additional inversion for v_S provides a small benefit while inversion for ρ visible decreases the resolution of the BSR contrast in v_P. In all tests a gradient starting model for v_P was used. Here, I compare the resolution in v_P of the reference inversion with gradient starting models for v_S and ρ with the result using a homogeneous v_P starting model (Figure 3.10). It can be seen that the full gradient cannot be resolved below BSR depth and the model stays close to the starting model. Above the BSR the gradient is mostly resolved with a visible shift towards the value of the starting model. The v_P distribution at BSR depth is resolved with a similar contrast as with the gradient starting model, but the signature is introduced at velocities approximately 100 m/s higher than in the true model. In field data applications a starting model with a parameter distribution closer to the true conditions can be expected than in this extreme case.

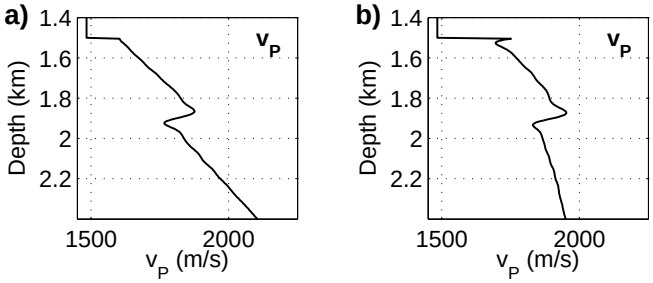

Figure 3.10: Mean v_P depth distribution for different v_P starting models. (a) Gradient, (b) homogeneous v_P starting model.

3.3 Geometry requirements

Typically, OBS stations are distributed along seismic profiles with a spacing in the range of a few hundred meters to several kilometers, depending on the purpose and area of interest. The availability of instruments and the general objective of the measurement are the main factors for the survey design. A regular deployment benefits the application of methods which require a consistent spatial sampling of the subsurface and a close spacing prevents undersampling or aliasing. The spacing of the OBS stations as well as the subsurface velocity distribution are the main factors in the recovery of models with ray-based methods.

For the simple FWI example discussed in this chapter, I study the differences in the resolution of the BSR velocity distribution based on the geometry of field data analyzed in this work. The resolution of different geometries is tested with a monoparameter inversion for v_P with gradient starting models in all three parameters. The same geometry as used in the previous tests is taken as the reference result with five stations in the central model part arranged directly above the seafloor with 1 km station separation. Further tests include a reduced number of OBS stations with their separation increased to 2 km, a reduced number of receivers (shot positions in the field measurement) at the sea surface, and an increased station separation with five OBS stations.

The resulting resolution of the v_P contrast at BSR depth is shown in Figure 3.11. For the geometry which was already considered previously (Figure 3.11a) the v_P maximum is resolved within 50 m/s and the v_P minimum within 100 m/s with slightly higher velocities in the zone where OBS stations are deployed. A reduced number of OBS stations (Figure 3.11b) yields a similar resolution of the v_P maximum and minimum as in the first test. The variation in the maximum values is slightly higher and the variation along the profile is less regular. As in the previous test, the values are highest at the sites of the OBS stations in the v_P maximum. With a reduced number of receivers (Figure 3.11c) and therefore decreased offset the BSR contrast is only resolved closely to the OBS stations. The variation in the maximum and minimum v_P values is lower than in the previous two examples. The error in the maximum v_P value is similar as before and the v_P minimum is overestimated by almost 50 m/s between the three central OBS stations. In the last example (Figure 3.11d) the same number of OBS stations is used as in the reference result but the stations are spread along the whole profile distance with 2 km distance. The resulting v_P model yields a better resolution of the maximum and minimum v_P values with lower parameter variation. The deviation of the values is similar to the other tests. The horizontal extent of the zone where the BSR v_P contrast is resolved is increased to approximately the distance covered by OBS stations.

The tests imply that a further spread of the OBS stations along the profile benefits the recovery of the BSR v_P contrast most while a closer station spacing does not necessarily improve the resolution.

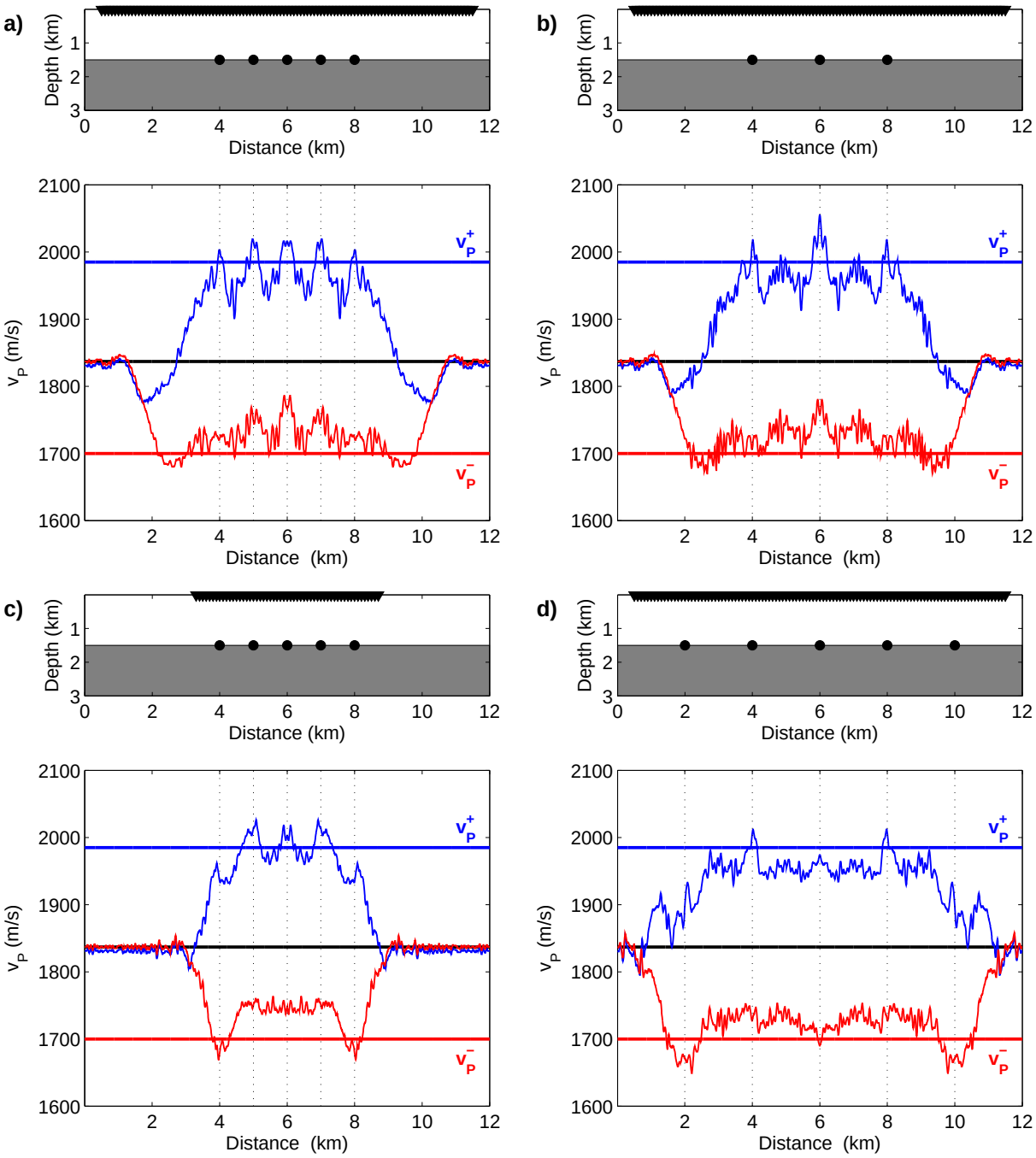

Figure 3.11: Resolution of the BSR v_P distribution for different geometries. (a) Reference geometry with five OBS and 1 km station separation, (b) reduced OBS number with increased station separation, (c) receivers reduced to half of the original offset, (d) station separation increased to 2 km. The vertical dotted lines mark the locations of the OBS stations.

3.4 Influence of approach

In Chapter 5 it is shown that application of time windowing is beneficial for field data inversion due to a mitigation of artifacts from location errors of the OBS positions. Time windowing is used to suppress the direct wave and primary reflections. Here, the previously used reference result with monoparameter v_P inversion and gradient starting models for all three elastic parameters is compared to a result where a time window which excludes the direct wave and primary reflections is applied. Furthermore, the full approach for field data inversion including horizontal smoothing, frequency filtering and the application of a normalized L_2-norm is applied and also compared to a result where additional time windowing is utilized. Horizontal smoothing is applied with a filter size of 8 GPs which corresponds to 40 m. Frequency filtering is applied in four stages with the low-pass frequency of the filter increasing in steps of 4 Hz from 4 Hz to 16 Hz.

The v_P contrast resolved with the described approaches is presented in Figure 3.12 together with the corresponding misfit evolution for all four tests. Figure 3.12a shows the differences caused by the application of time windowing which reduces the input to multiply reflected signals and refracted waves. It is shown that the variation in the v_P maxima and minima is higher and the deviation to the true values reaches 100 m/s. The horizontal resolution of the v_P contrast is slightly increased. The misfit is reduced similarly for both approaches although the final misfit is lower when no time windowing is applied.

When additional smoothing, filtering and normalization is applied (Figure 3.12b) the differences between the inversion of time windowed and full data are much lower than in the previous test. Again, the variation in the result where time windowing is applied is slightly higher than in the result without. In both results the v_P contrast is resolved with smaller amplitude compared to the original contrast with values of the maximum and minimum under- and overestimated by approximately 50 m/s, respectively. The v_P minimum is reconstructed better when time windowing is applied.

In summary, the application of time windowing affects the result of the inversion by introducing slightly higher horizontal parameter variations. The variations are much less significant when additional smoothing, filtering and normalization is applied. The synthetic tests suggest that the influence of time windowing is acceptable when positive effects like a mitigation of large artifacts can be achieved.

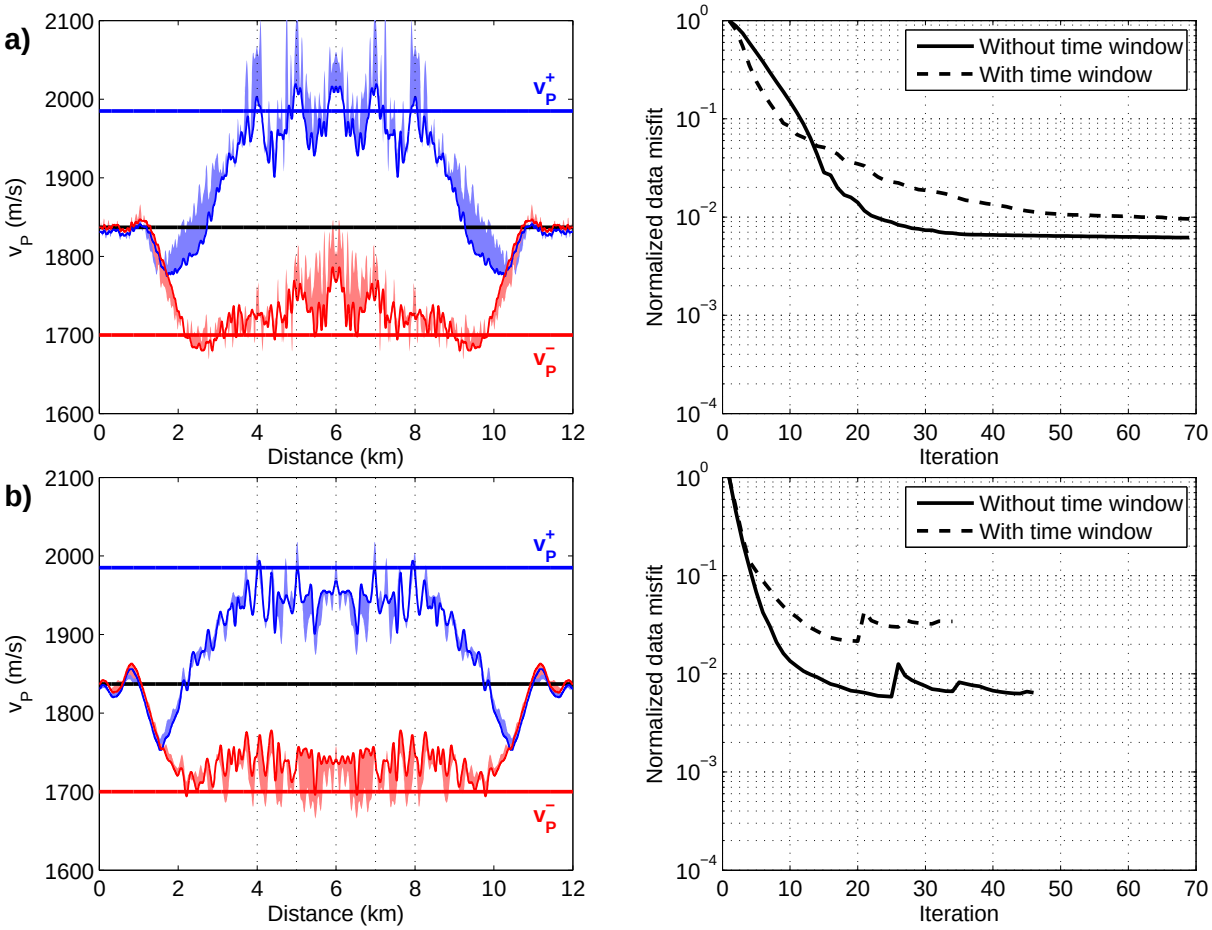

Figure 3.12: Comparison of the resolution of the BSR v_P distribution for different approaches. (a) Without and (b) with horizontal smoothing, increasing high-pass frequency, and a normalized L_2 norm. The shaded area in the left plots shows the difference when applying time windowing (solid blue and red lines: without time windowing). The vertical dotted lines mark the locations of the OBS stations. On the right, the misfit evolution corresponding to each test is shown.

3.5 Summary

Inversion of data calculated for a synthetic or "toy" example provides insight into the potential of FWI in the context of hydrate and gas occurrence for OBS data. Different tests show the applicability for a simple example with an increase of the elastic parameters with depth including an additional increase in v_P and v_S above the BSR and a decrease of v_P and ρ below. The parameter contrast at BSR depth can be robustly reconstructed in the v_P model for most test cases. The P-wave velocity can be resolved well when the v_S model closely resembles the true conditions. An acoustic inversion where v_S is neglected provides similar results in this test setting. Additional inversion for v_S provides a small benefit to the reconstruction of v_P. The density starting model hast little influence on the outcome of the inversion for v_P and inversion for ρ decreases the resolution of the BSR contrast in v_P.

Furthermore, the geometry has a significant effect on the resolution of the v_P distribution at BSR depth. A further spread of OBS stations along the profile benefits the inversion. The OBS spacing in this test setting has a lower influence than the spread of the stations. A reduction of receivers (shot positions in the field measurement) limits the resolved parameter contrast to the area covered.

The application of time windowing and the comparison with an approach where additional smoothing, filtering and normalization is applied show that the setup of FWI also significantly affects the resolved parameter distribution. The v_P maxima and minima are recovered with higher parameter variation when time windowing is applied. With further application of smoothing, filtering and normalization the resolution of the v_P contrast is slightly reduced.

4 Preparation of field data

Within European waters the Black Sea is one of the most promising regions for finding gas hydrate deposits. The Black Sea is a body of water bordering the Ukraine, Russia, Georgia, Turkey, Bulgaria, and Romania (clockwise from north) and covers more than 400 000 km^2. The main part of the Black Sea is a basin structure with water depths reaching up to 2200 m. An extensive shelf region (extending up to 200 km from the coast) exists in its northwestern part where the main fresh water inflow occurs with water depths up to 100 m. The main supply originates from the Danube, Dniester, and Dnieper rivers (from west to east). At the shelf edges complex channel-levee systems exist constituting the deep-sea fans of the Danube and the Dnieper fan (Popescu et al., 2001). They carry turbidite deposits into the deep sea leading to thick sedimentary layers. Due to the inflow of saline water from the Mediterranean via the Sea of Marmara and the Bosporus the deep waters of the Black Sea are anoxic. The main sedimentary body includes fine-grained organic-rich layers which are prone to host methane hydrate. Because of the migration of gas upslope the shelf edges are most likely to contain hydrate deposits. A first detailed study of hydrate and gas saturation at a BSR site in the northwestern part of the Black Sea was accomplished from OBS data by Zillmer et al. (2005) in the vicinity of the Dnieper canyon. Results indicate a hydrated layer with approximately 40 % hydrate saturation of the pore space and low gas saturations (making up

Figure 4.1: Map of the Western Black Sea with the geometry of Area 1 located off the coast of Bulgaria. Data was acquired by with RV Maria S. Merian on cruise MSM34-2 in 2013/2014.

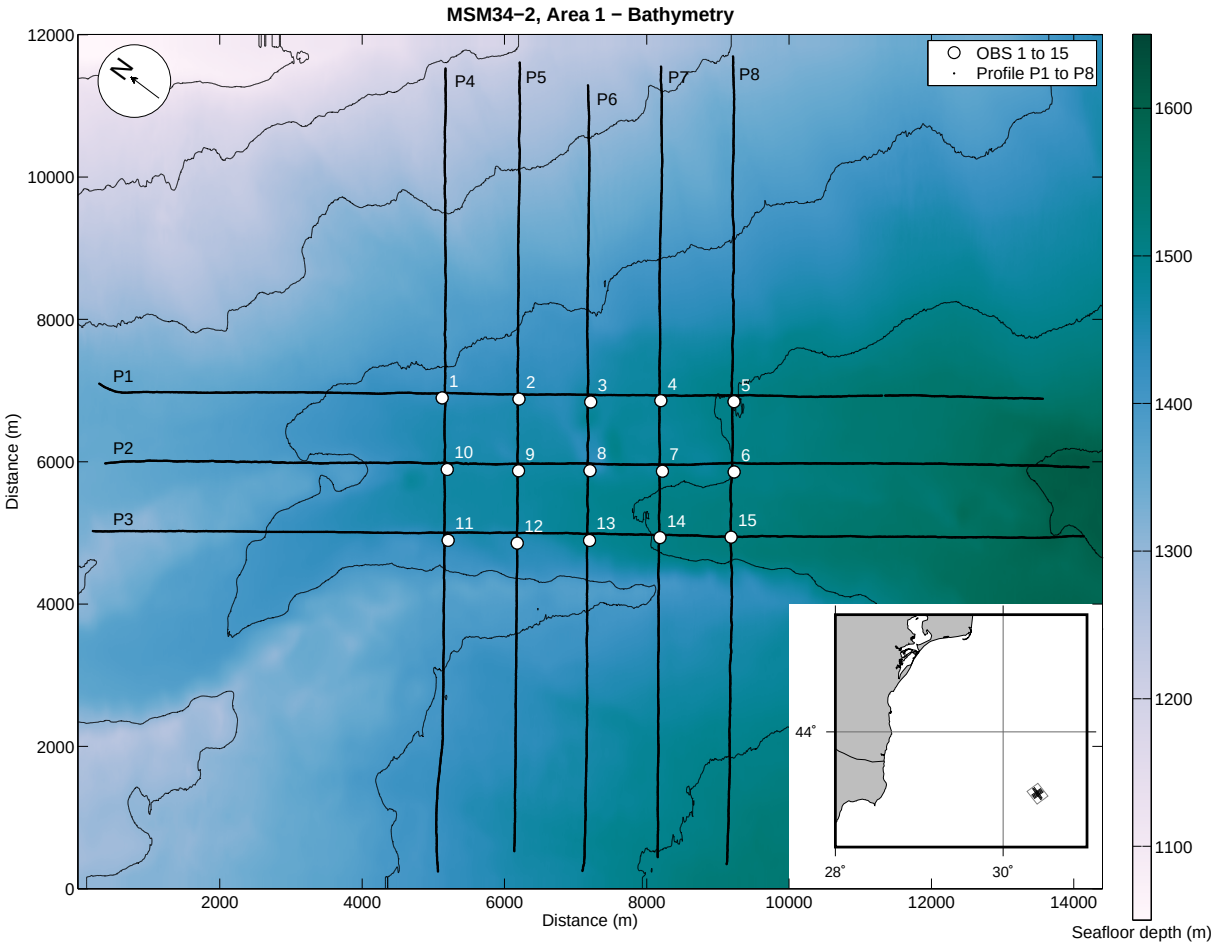

Figure 4.2: Seafloor topography and geometry of the OBS field measurement (coordinates are rotated by 54.5°, the coordinate origin is at 43.5°N / 30.3°E). Inset: Location of the measurement area off the shore of Bulgaria.

less than 1 % of the sediment). An application of FWI to seismic streamer data from the Western Black Sea (WBS) is shown by Routh et al. (2017), who detect gas bodies as potential hazards in exploration but do not interpret any hydrate occurrence in their results.

The data set studied in this work was recorded with RV Maria S. Merian on cruise MSM34-2 in 2013/2014 (Bialas et al., 2014). During the first leg of the cruise (MSM34-1) regional seismic data were acquired along 28 profiles with a total length of 2200 km using a streamer of 1 km length. The area covered was approximately 95 km (SW-NE) by 60 km (NW-SE) and oriented symmetrically about the Danube canyon which connects the shelf region with the deep-sea fan (Popescu et al., 2004). The aim was to map the inactive, partly-buried channel systems of the deep-sea fan where BSRs occur widely. Further high-resolution 2D seismic data with a streamer length of 62.6 m was collected for structural mapping in two areas, together with data from 15 and 12 OBS, respectively. Area 1 was chosen at a channel-levee system southwest and Area 2 to the east of the Danube canyon. While no gas bubbles were identified in the water column in Area 1, gas expulsion was detected by flare imaging in Area 2. An upward-bending BSR was observed in Area 2 which also indicates gas emission. Water depths were 1500 m and 700 m in Areas 1 and 2, respectively. As the sand-rich channel infills in Area 1 are expected

to provide the best conditions for hydrate occurrence and potential recovery, it was chosen for further study in this work.

The location of Area 1 within the Western Black Sea is shown in Figure 4.1. A detailed map of the seafloor topography and the geometry of the OBS and high-resolution seismic measurements is given in Figure 4.2 in a rotated coordinate system. Water depths range from less than 1100 m in the northernmost part of the area to over 1600 m in the southern part. A filled channel structure extends through the center of the measurement area from northwest to southeast with a pronounced levee on the southwestern side. The geometry consists of eight profiles, of which three are oriented along the channel axis and five perpendicular to it. 15 OBS stations were arranged in a three by five grid with 1 km station separation at the crossing points of the eight profiles. Because the OBS are released at the sea surface and reach their final position in free fall through the water column, positions deviate from the point of release. A repositioning was then achieved by analysis of first-arrival signals (A. Dannowski, pers. communication, 2015). The sampling interval for data recording was set to 1 ms and clock correction was applied after the instrument recovery. The coordinates of the shot positions were logged during acquisitions together with water depth. Shots were emitted by a 45/45 in^3 GI gun (e.g., Landrø, 1992) in an interval of 5 s resulting in a shot spacing of about 8 m to 10 m. Each OBS station was equipped with a hydrophone and a three-component geophone (Bialas and Flueh, 1999). Additionally, within the high-resolution and OBS seismic measurement area 3D P-cable (Planke et al., 2009) seismic measurements were performed within a zone of approximately 8 km by 4 km. From these data a BSR horizon was mapped (Figure 4.3, T. Zander, pers. communication, 2015) which extends over most of the area covered by OBS stations with the exception of stations 1 and 2.

A detailed analysis of BSR occurrence and interpretation of multiple BSRs which crosscut strata is given by Zander et al. (2017), with data from MSM34. The observation of multiple BSRs is attributed to sealevel lowstands during the last glacial period and the depth of the BSRs are related to paleo-seafloor depths. Potentially, low amounts of gas are still trapped below the paleo-BSRs. In Figure 4.4 the migrated high-resolution seismic data of profile P7 (2D HMCS line 1107 in Zander et al., 2017) with the interpreted main BSR at approximately 400 mbsf is shown. Zones of weak and sharp BSR reflections are distinguished. In the upper 200 mbsf a pronounced layering can be observed which is disturbed by a chaotic reflection zone towards the center of the channel axis. Differences in the layering are visible between the southwestern and northeastern side of the channel. Above the BSR horizon three distinguishable reflections at approximately 1600 m, 1700 m, and 1800 m depth can be seen on the left-hand side, while they cannot be determined on the right. Two zones of high reflection amplitudes are visible reaching down to 100 m below the BSR underneath OBS 14 and OBS 4. At OBS 14 the reflections are fully below the BSR and orientated parallel to it whereas beneath OBS 4 they continue across the BSR with lower amplitude, which is an indication for the presence of free gas.

To study the distribution of potential hydrate and gas deposits highly detailed models of the elastic parameters of the subsurface need to be obtained. FWI is applied to resolve the subseafloor parameter distribution for the data acquired in the study region.

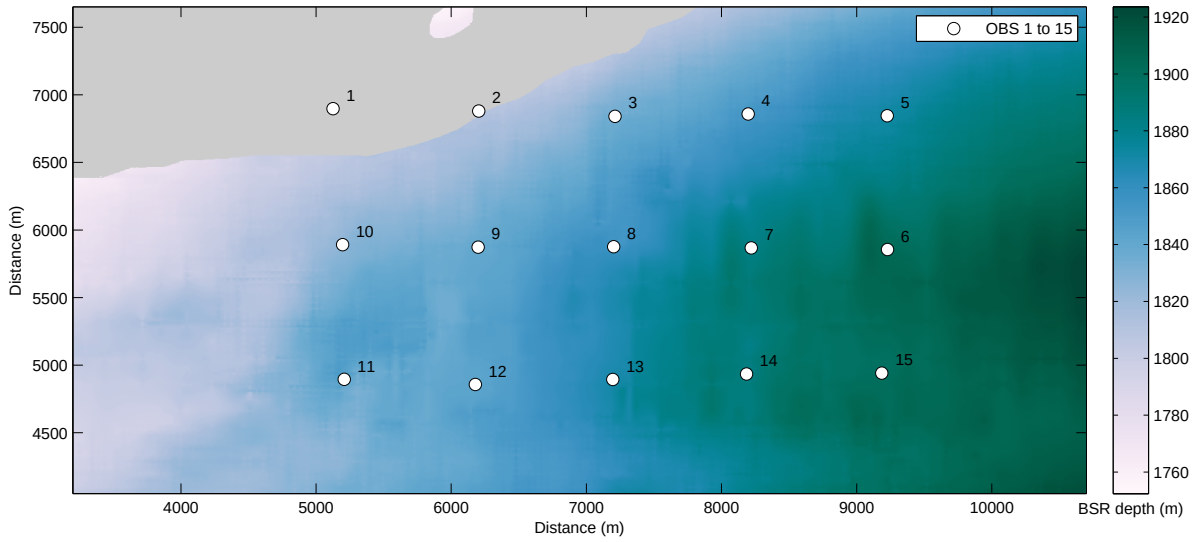

Figure 4.3: BSR depth with OBS locations within the P-cable measurement area. The BSR depth was mapped in the 3D P-cable data. Within the gray area no BSR signature was observed.

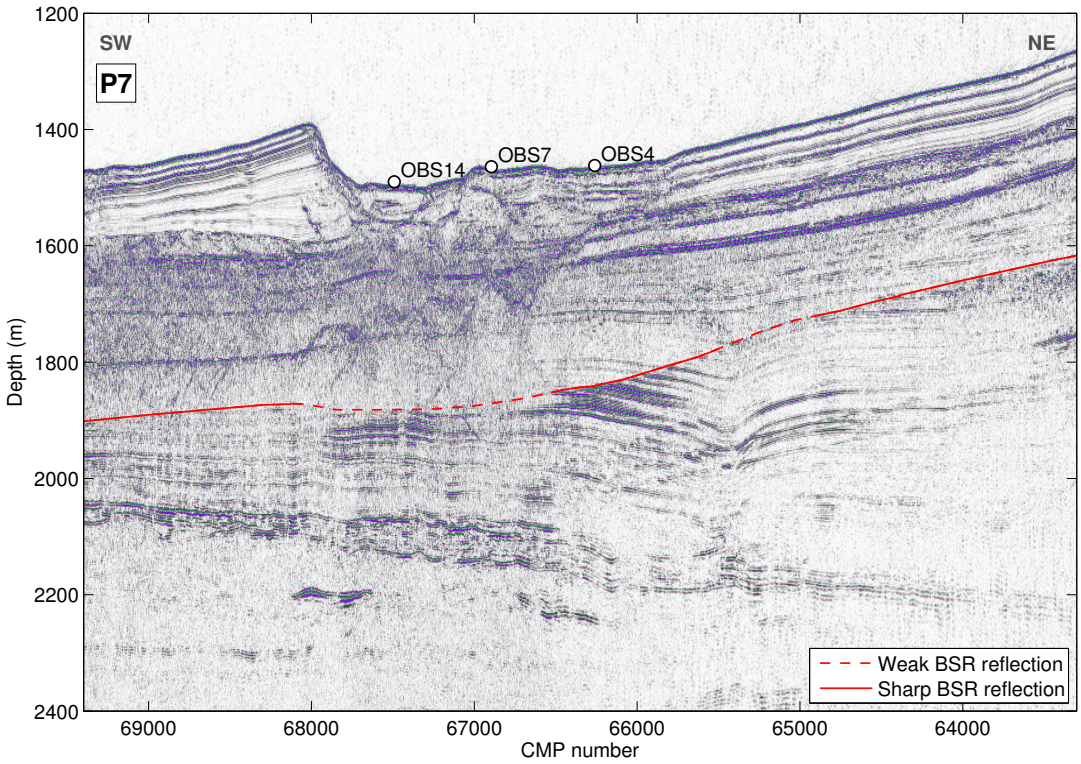

Figure 4.4: Time-migrated seismic data from profile P7 with interpreted BSR horizon by Zander et al., 2017 (red line). Depth conversion was applied using a velocity model from regional seismic measurements. The CMP distance is 1.56 m.

4.1 Starting model generation

Traveltime tomography based on the refracted wave first arrivals was performed following the approach of Zelt and Smith (1992) for each profile in area 1 (A. Dannowski, pers. communication, 2015). From these tomography models the v_P starting models for FWI (Figure 4.5) are constructed by interpolation to an equidistant Cartesian grid. The tomography result is limited by ray coverage (compare Figure 4.6) and therefore, v_P is extrapolated horizontally to the model limits for a profile distance of 14.4 km to include all shot positions. To satisfy spatial discretization criteria, a grid point (GP) distance of 2 m is chosen, resulting in a model size of 7200 GPs by 1500 GPs for a model covering 14.4 km distance and 3 km depth. Approximately half of the model area is made up of the water column. The water velocity is chosen constant at 1484 m/s which matches well with measured water velocities in the area (compare also Leroy et al., 2008) and is found to match observed arrival times of the direct wave. v_P is smoothly increasing with depth up to a maximum P-wave velocity of around 2430 m/s. To derive a model of the density ρ the Gardner relation (Gardner et al., 1974) given as

$$\rho(\mathbf{x}) = 310 \cdot v_P(\mathbf{x})^{0.25} \frac{\text{kg/m}^3}{(\text{m/s})^{0.25}} \tag{4.1}$$

is applied. The resulting density values below the seafloor range from around 1950 kg/m^3 to 2180 kg/m^3. The density in seawater is set to 1020 kg/m^3. A model for the attenuation is given by approximating a constant Q factor below the seafloor, while the Q factor in the water column is set to a high value (e.g., 1000) to simulate an attenuation-free medium. As the value for the model region below the water column I choose $Q = 100$ which was found by Zillmer et al. (2005) to be a good estimate for the sediments of the WBS region. Details on the Q estimation can be found in Appendix B.2.

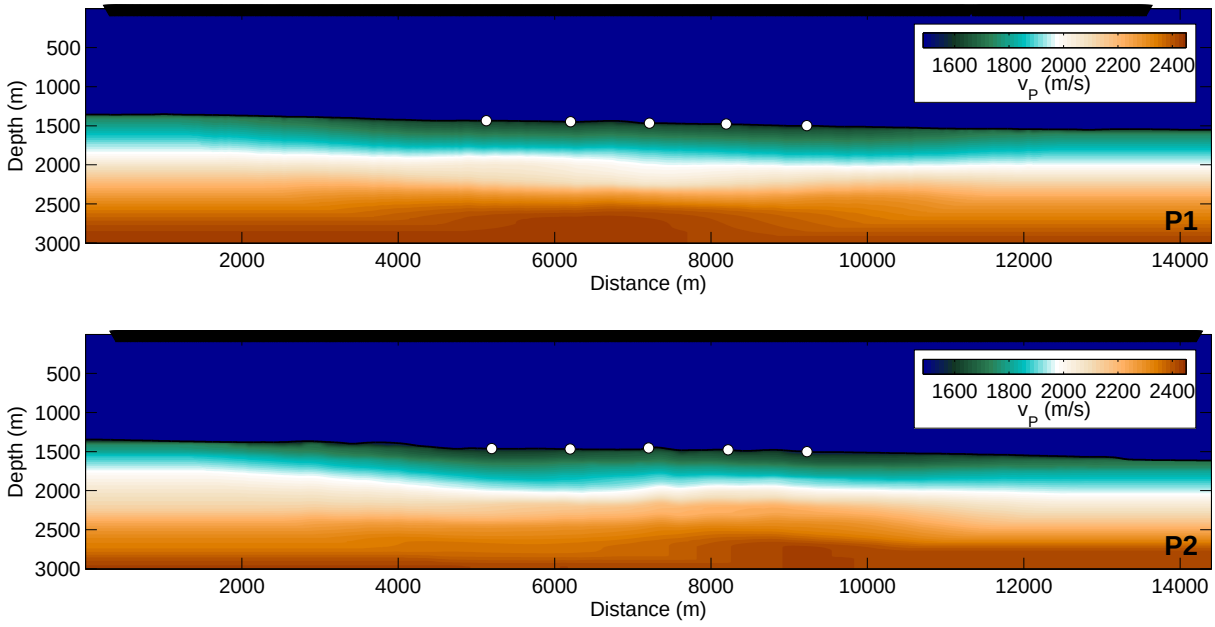

Figure 4.5: Models of P-wave velocity for profiles P1 (top) and P2 (bottom). Shot positions of the field measurement are indicated by black triangles, OBS locations by white circles. The resulting v_P distribution from traveltime tomography was extrapolated horizontally.

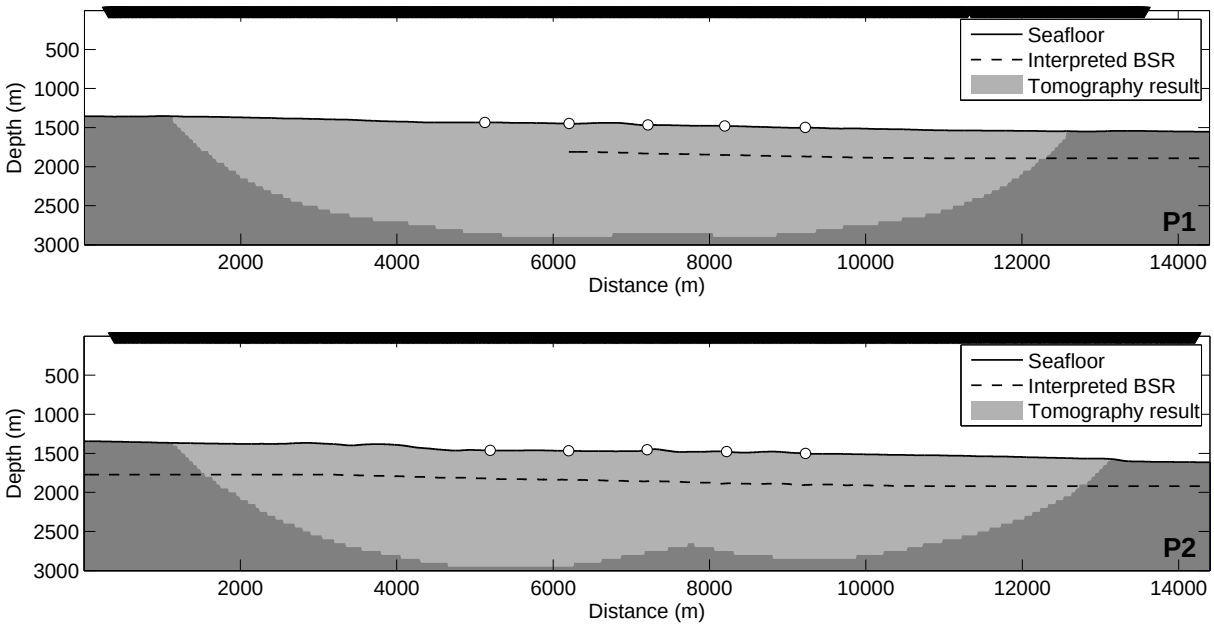

Figure 4.6: Geometry of the OBS survey along profiles P1 (top) and P2 (bottom). Shot positions of the field measurement are indicated by black triangles, OBS locations by white circles. The extent of the tomography results are indicated by the areas shaded in lighter gray and the interpreted BSR horizons by the dashed lines.

4.1.1 Preconditioning

From the bathymetry data (Figure 4.2) a taper is created which follows the seafloor depth of the respective mean OBS location of the profile (compare Figure A.1). It is included in the inversion process to prevent updates in the water column. The taper is applied separately to all parameters updated during the inversion. It includes a squared-cosine type gradient of 60 GPs which increases from zero in the water column to one in the model area with the gradient zone centered at the seafloor. This allows some minor corrections by the inversion in this zone but guarantees a smooth transition.

Additionally, radially symmetric tapers are applied at the OBS positions which are used as the sources in the modeling scheme. Close to the sources the largest updates occur due to the high amplitude of the wavefields. Updates near the source positions are often nonphysical and prevent updates in the remaining model area. The taper reduces the gradient values logarithmically towards the position of the sources.

As previously mentioned, an approximation of the Hessian operator (Equation 2.25) can be used to precondition the gradients. In this work, I apply the scheme developed by Plessix and Mulder (2004). It compensates for amplitude loss caused by geometrical spreading and is applied shot wise.

Furthermore, horizontal smoothing is applied to the gradient after the summation over all shots by a Gaussian filter. The size of the filter used for field data inversion is 20 GPs.

4.2 Data selection and processing

Data from the OBS measurement are chosen for the application of FWI because they provide the longest offsets. Both hydrophone and three-component geophone data are available for all 15 stations with the exception of two geophone components of OBS 10 and OBS 12. Strong interference signals from a nearby industry seismic measurement were recorded from the last third of profile P2 onwards, reducing data quality on all instruments significantly. In Figure 4.7 the RMS of each shot is plotted for each OBS station of profiles P1 and P2. Notably, on profile P2 after shot 1400 distinct sets of high-amplitude shots occur at each station which are delayed from one station to the next resulting from the concurrent industry seismic measurement. Relative to the near-offset RMS values the amplitude of traces with interfering signals is strongest on OBS 6 and decreases along the profile.

On both profiles data from one station are affected by strong noise signals with RMS amplitudes significantly higher than those of the usable signals (OBS 5 on profile P1 and OBS 10 on profile P2). Through the application of a normalization by the RMS for each trace (see section 2.2.1) shots with noise amplitudes exceeding those of the desired signals do not contribute to the model update in FWI because no match of the signal content is possible. Because of the normalization the contribution of bad traces to the misfit is proportional to their relative number. At profile P2 approximately 20% of the data are impaired. Further assessment showed that for both profiles the data quality of the geophone components is much lower than that of the hydrophone for at least half of the instruments in the frequency range below 30 Hz. As the low-frequency portion is the most significant for a successful application of FWI I choose the hydrophone data for further processing.

Due to the high noise level from seismic interference, only data from profiles P1 and P2 are considered for FWI. Details on the location of the OBS stations and the geometry of the profiles are provided in Appendix A.

From the full recordings data are extracted and stored in gathers for each OBS station and for each profile. For each shot a total recording time of 6 s is selected so that the direct wave is included for all offsets. This results in an overlap of 1 s as the shot interval is 5 s. Furthermore, it is necessary to resample the data in order to satisfy the discretization criteria of the FD method. For fourth-order spatial accuracy and 2 m grid-point distance the temporal sampling is set to 0.4 ms compared to an original sampling of 1 ms.

An exemplary OBS gather of the raw hydrophone data is shown in Figure 4.8a with time windowing applied to mute all events before the first arrivals and at 4.5 s after the first arrival. The most prominent signal is the direct wave starting at the nearest offset at about 1 s recording time, with strong reverberations for about 0.5 s. Lower amplitude reflections follow the reverberations. The first-order seafloor multiple arrives at the nearest offset at 3 s followed by a relatively strong reflection after approximately 0.5 s which is related to the BSR. Refracted wave signals represent the first arrival up to 3 km and from 11 km profile distance onwards. Amplitude spectra summed over all shots of the raw hydrophone data are shown in Figure 4.8b, and in detail for frequencies up to 60 Hz in Figure 4.8c. Frequencies up to almost 400 Hz are present in the raw data with strong peaks at particular frequencies with the peaks decreasing in amplitude and broadening in width with increasing frequency. The main signal energy is below 160 Hz. The effect of 3D-to-2D transformation and filtering on an exemplary trace is shown

in Figure 4.8d with the respective spectra shown in Figure 4.8c. It becomes obvious that the transformation increases the amplitude of the lower frequencies and filtering is necessary to suppress the very low-frequency noise. Higher frequencies are damped in amplitude by the transformation compared to the input data. Figure 4.9a shows the field data after processing including the 3D-to-2D transformation with a constant velocity corresponding to the water velocity (see Section 4.1). The application of the transformation results in relative decrease of the higher-frequency amplitudes. The amplitude of noise below 5 Hz is increased dramatically. Therefore, a Butterworth high-pass filter of 4th order with a cut-off frequency of 5 Hz is applied. The resulting frequency spectrum is shown in Figure 4.8c. The main signal energy is now below 30 Hz.

Due to the large signal amplitudes before the first arrival resulting from the dense shot spacing and the strong reverberations following the direct wave arrival I consider the application of time windowing. The main signal energy is transported by the direct wave which has by far the strongest amplitude. Yet it does not contain much information since the water velocity and seafloor topography are fairly well known. Furthermore, the primary reflections following the direct wave are masked by the reverberations. Similar information compared to the primary reflections is carried by the multiply reflected wave signals whereas the amplitude distribution is much more even and also comparable to the refracted wave signals. The frequency content of the separate wave signals of the direct wave and primary reflections, the multiple reflections, and the refracted waves are shown in Figure 4.9c. A sketch of the corresponding ray paths is shown in Figure 4.9d.

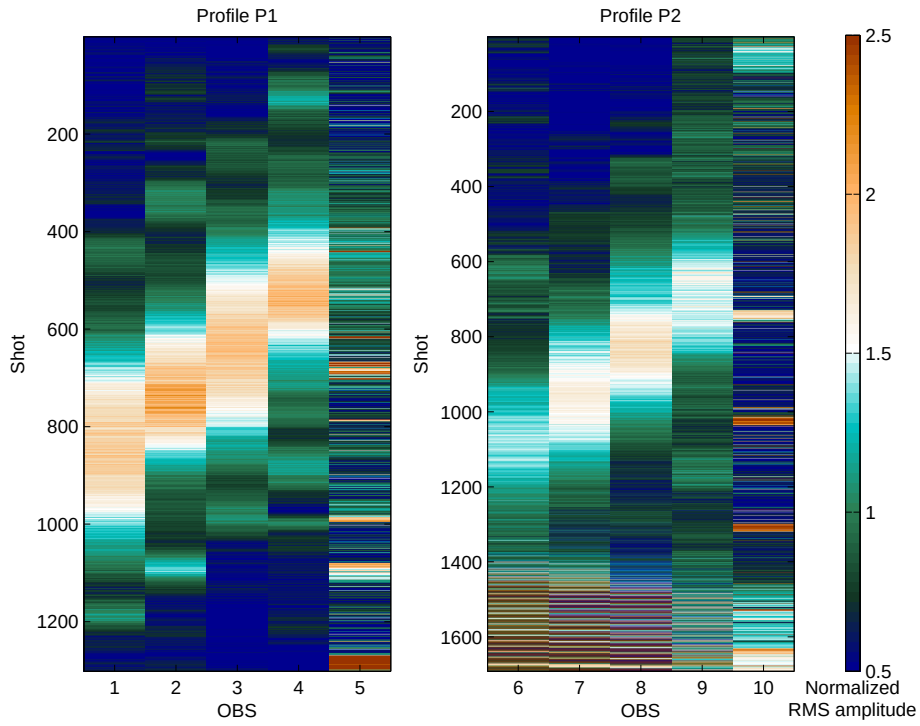

Figure 4.7: RMS amplitudes for all traces of the hydrophone data of profiles P1 (left) and P2 (right). Amplitudes are normalized to the mean value at each OBS station.

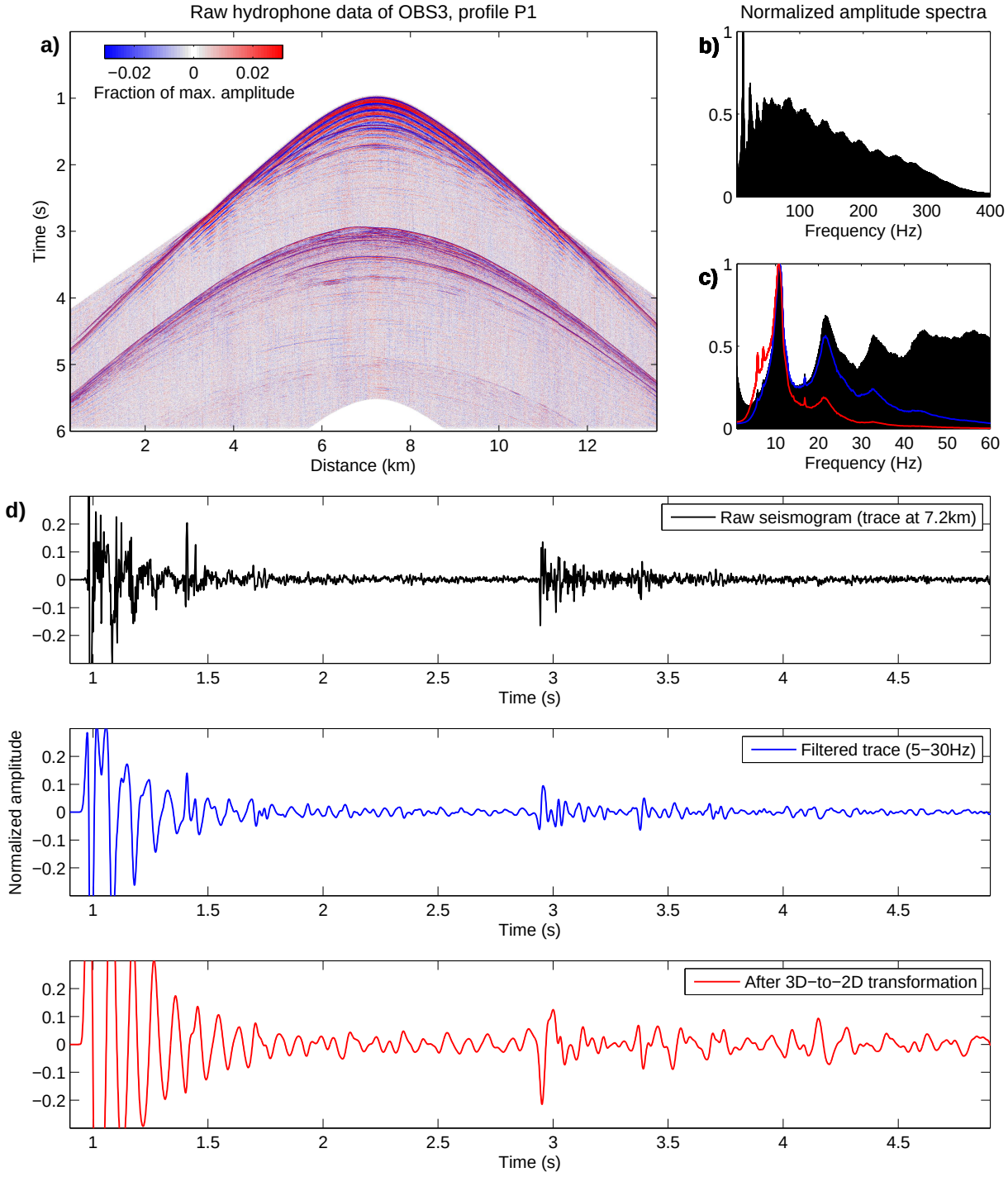

Figure 4.8: Overview of the signal and frequency content of the hydrophone data of OBS 3 for profile P1. (a) Raw field data muted before the first arrival. Refracted wave signals represent the first arrival up to 3 km and from 11 km profile distance onwards. (b) and (c) provide the amplitude spectra of the data shown in (a) for up to 400 Hz and 60 Hz, respectively. (d) Normalized trace at 7.2 km profile distance without processing (black), with a band-pass filter of 5 Hz and 30 Hz corner frequency (blue), and after the application of the 3D-to-2D transformation and the same band-pass filter (red). Corresponding spectra of the processing steps summed over all traces are shown in (c).

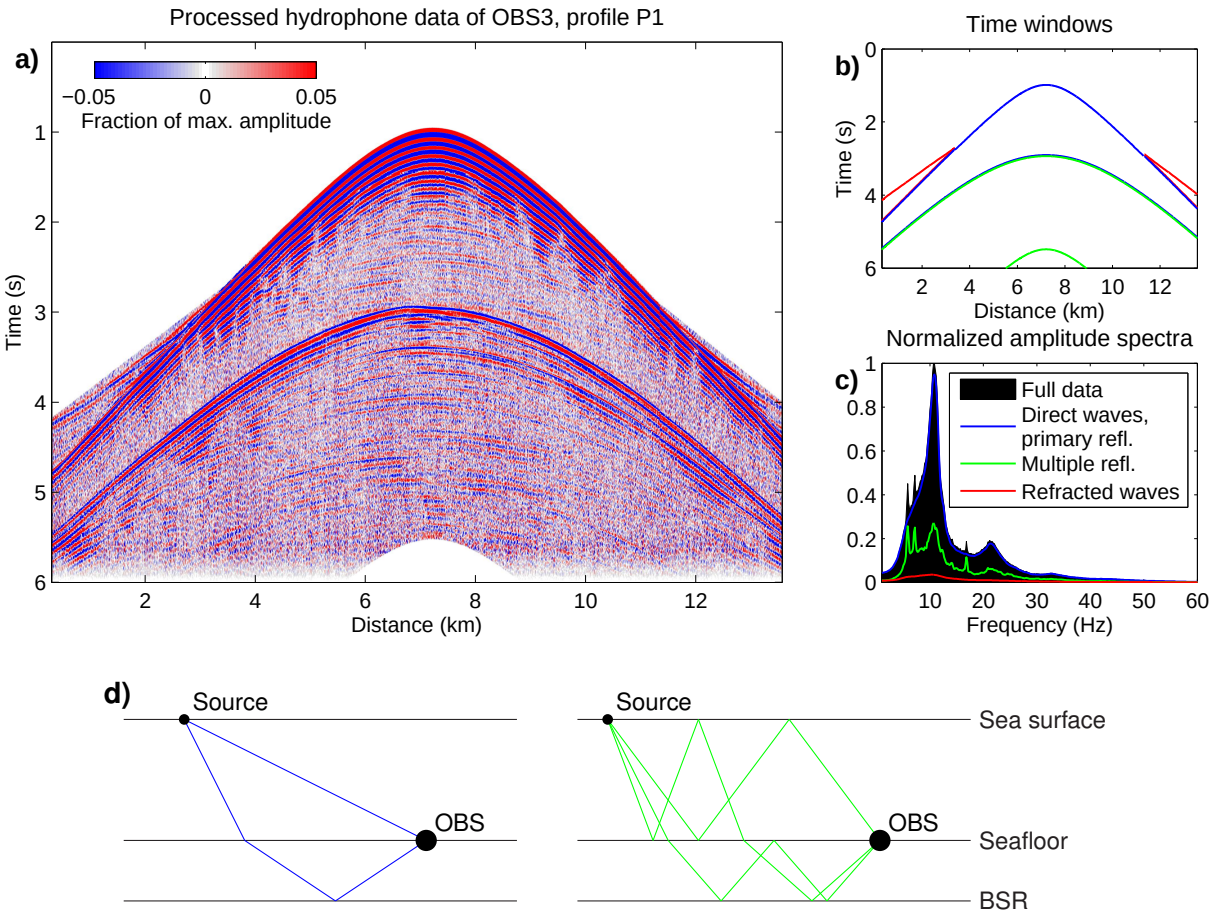

Figure 4.9: (a) Processed field data with the same mute as in Figure 4.8a. Processing includes 3D-to-2D transformation and high-pass filtering with a Butterworth filter of order 4 and a cut-off frequency of 5 Hz. (b) Time windows for the direct waves and primary reflections (blue), multiple reflections (green), and refracted wave signals (red). (c) Frequency distribution for the data shown in (a) in black with the spectra of the specific time windows shown in (b) in blue, green and red. (d) Ray paths of direct wave and primary reflections (left) compared to multiply reflected rays (right).

4.2.1 Time windowing

The taper f_{tw} used to damp the seismograms outside the time window $t \in (t_{\min}, t_{\max})$ is defined by

$$f_{\text{tw}}(t) = \begin{cases} e^{-\gamma(t-t_{\min})^2} & t \leq t_{\min} \\ 1 & t_{\min} < t < t_{\max} \\ e^{-\gamma(t-t_{\max})^2} & t \geq t_{\max}. \end{cases} \tag{4.2}$$

For the presented applications I choose $\gamma = 10^4$. In Figure 4.10 the application of the discussed time windowing approach is shown for an exemplary OBS gather. To define the time windows the theoretical arrival times of the direct wave and first-order seafloor multiple are calculated from the shot-receiver distances with a constant water velocity (see Section 4.1) and assuming a plane seafloor. Before the direct wave an extra of 0.02 s is added and 0.2 s before the arrival of the multiply reflected events.

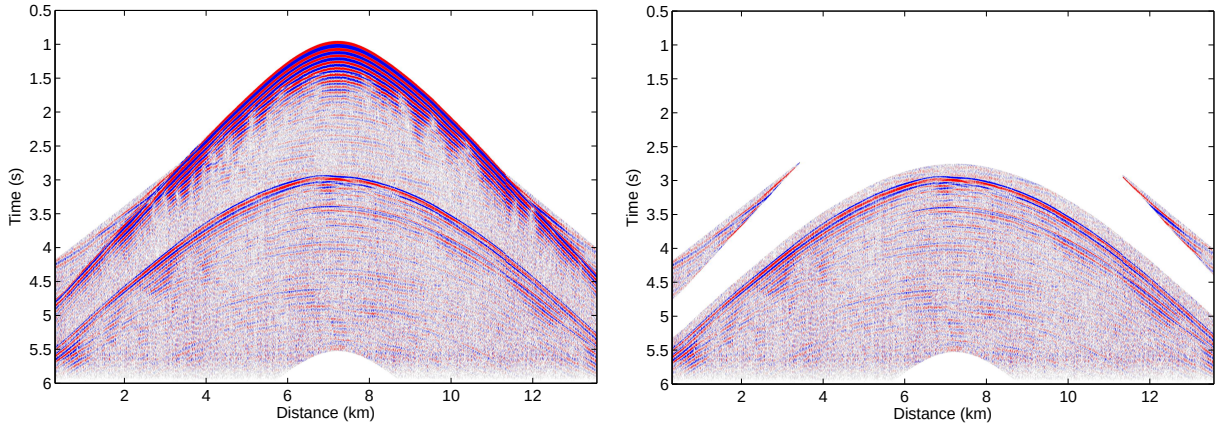

Figure 4.10: Data of OBS 3 for profile P1 (left) without and (right) with time windowing applied.

4.2.2 Initial source time function

An initial source time function needs to be chosen for a first simulation of synthetic data. From the preceding section it becomes obvious that a characteristic ringing following at least the direct wave arrival is visible in the data and assuming a linear behavior of the instrument this characteristic signature is expected to be present for each reflection. Also the frequency spectrum shows a particular appearance with distinct peaks. Through the 3D-to-2D transformation the frequencies beyond 30 Hz have very low amplitudes. To guarantee a good recovery of the source time function by the method presented in Section 2.3.2 a function with a broad spectrum (broader than the respective field data spectrum) has to be provided. For this purpose I utilize a wavelet f_{stf} defined by

$$f_{\text{stf}}(t) = \begin{cases} \sin(2\pi(t-t_d)f_c) - \frac{1}{2}\sin(4\pi(t-t_d)f_c) & t \in [t_d, t_d + 1/f_c] \\ 0 & \text{otherwise.} \end{cases} \tag{4.3}$$

Its shape and the corresponding frequency spectrum for $f_c = 16$ Hz are shown in Figure 4.11.

For the inversion a constant time shift of 0.1 s is applied to the source time function and the data. It is a measure to guarantee that the signal amplitude is zero at the onset of the source time function in case there is any constant mismatch between the modeled and true arrival time. Errors in the processing cannot completely be avoided such that small shifts possibly remain unnoticed. Sources of errors can be the assumption of a constant water velocity which in reality is depth dependent and can lead to deviations in the discussed order of magnitude. The effect would however be offset dependent. Furthermore, the seafloor depth is potentially erroneous as the resolution of the bathymetry data is in the order of 10 m. Shifts between the field and the assumed geometry are also possible. If time shifts are constant they can be mitigated by the source time function inversion.

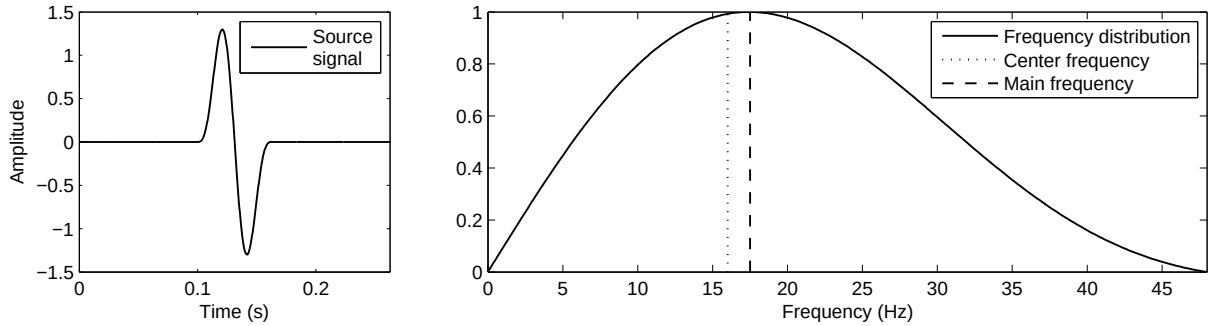

Figure 4.11: Initial source time function (left) with corresponding amplitude spectrum (right).

4.3 Summary

In this chapter the field data set and measurement area, located in the Western Black Sea near the Danube deep-sea fan, are introduced. The data set comprises reflection seismic data measured along the same profiles as the OBS data used in this work. Furthermore, 3D P-cable data was measured in an area enclosing the OBS stations and from this data the extent of the BSR was determined.

With the data set resulting P-wave velocity models from traveltime tomography applied to the OBS data were made available and are prepared as the starting models for FWI. By the application of the Gardner relation density models are calculated from the v_P models. Bathymetry data is used to create tapers for preconditioning which prevent updates in the water column where constant parameters are expected.

Due to the superior data suitability for FWI, hydrophone data are chosen for further use while geophone data are not considered. Signals from a concurrent industry seismic measurement affect all data measured after the first two profiles which is why only these profiles are considered for FWI.

Data processing includes the application of 3D-to-2D transformation, resampling and filtering. The application of time windowing and its assumed benefits are discussed. Results from different time windowing approaches are presented in the following chapter.

5 Field data inversion

In this chapter the results of the acoustic inversion of the data from profiles P1 and P2 are presented. The main focus lies on the inverted models of v_P, although at first also inversion for density is applied which is the standard approach in field data inversion. In a second step monoparameter inversion for v_P is applied. Results with varying time windowing approaches are shown and compared. The misfit evolution and the inverted source time functions are presented as well as a comparison of the data fit at the nearest offset for the central OBS station. Differences between the multiparameter and monoparameter results are visualized by comparing depth profiles and the BSR v_P distribution.

For details on the discretization and computing times see Appendix B.2. There, I also give details on the parameters chosen for step length estimation, Q estimation, and parameter limits. The computation time for a maximum of 25 iterations was 4.5 hours on 480 cores.

5.1 Inversion setup

The progress of the inversion is controlled by a workflow providing the setup for each stage, e.g. different time windows or inversion parameters. In the presented applications the main change in each workflow stage is the increase in the utilized frequency range. I apply four stages comprising low-pass corner frequencies of 10 Hz, 15 Hz, 20 Hz and 30 Hz. A minimum number of three iterations is set allowing the conjugate-gradient scheme to start anew at each workflow stage. As shown in Figure 4.8 the amplitude of the frequency spectrum decreases rapidly beyond 20 Hz, i.e. it is expected that higher frequencies provide only limited information for the inversion. The high-pass corner frequency is kept constant at 5 Hz for each workflow stage, an example with a high-pass corner frequency of 3 Hz can be found in Appendix C for comparison. Resulting parameter models are slightly smoother than the results obtained with 5 Hz high-pass frequency.

In a first step different time windowing approaches are compared. As previously mentioned, the direct wave arrivals are the dominant events and their high-amplitude ringing masks most of the primary reflections. Therefore, I compare approaches discarding the direct wave and most of the primary reflections with results using all events. Furthermore, for the approach using only multiply reflected waves an increasing time window is applied in a third test. The time window following the first multiple is uniformly increased from 0.5 s to 2 s with one specific time window used per frequency stage (i.e., 0.5 s at 10 Hz low-pass frequency, 1.0 s at 15 Hz, and so on).

In the following the sources and receivers of the reciprocal modeling approach in FWI are termed OBS and shot positions, respectively, to meet the description of the true geometry of the field measurement. In the case of the source time function inversion this means that I do not invert for a signature of the true source used in the field but for a characteristic signature corresponding to each OBS station. Therefore,

effects like noise sources near the OBS location, instrument-specific characteristics, and deviations in the positioning will come into play rather than effects from the actual seismic source. Nevertheless, the STFs are a valuable output of the inversion to validate that results are consistent between OBS stations.

5.2 Profile P1

Data from 1301 shot positions from all five OBS stations are used for the first profile with the applied time windows shown in Figure 5.1. In the seismograms the BSR reflection is visible as a major reflection following the first-order seafloor multiple after 0.5 s. The corresponding primary BSR reflection cannot be discerned.

5.2.1 Multiparameter inversion

The resulting P-wave velocity models for the three different time windows (Figure 5.2) show similar results regarding the general trend of the updates. Models are updated to the full depth and towards the edges where the coverage of shot positions ends. Differences in the updates close to the seafloor and at BSR depth, especially in the vicinity of the OBS stations, are most significant. Inversion results using all events (Figure 5.2a) show that close to the OBS stations circular structures are constructed by FWI, which are particularly prominent at OBS stations 1 and 3. As they cannot be interpreted as natural structures they are classified as artifacts. Close to the seafloor a reduction in v_P for approximately 30 m can be observed. However, directly at the seafloor a layer of increased velocity is constructed which is of low amplitude in between the OBS stations. It can be clearly recognized away from the OBS positions. The same observation of such a behavior was found in the synthetic tests when the density values at the seafloor were incorrect. No negative influence of these artifacts on the recovery of the BSR signature was observed, though. Underneath the reduced v_P zone below the seafloor a stronger increase in the velocity with depth is found than assumed in the starting model. At BSR depth a clear drop of velocity by approximately 200 m/s is visible. The zone of reduced v_P is continuous from about 6.3 km to 10.7 km profile distance. Below the low-velocity zone v_P increases mainly with depth.

With a time window disregarding the direct waves and primary reflections the artifacts near the OBS stations vanish (Figure 5.2b). The increase of v_P at the seafloor and its decrease directly below is now distinctly visible also between the OBS stations. In contrast to the result from the inversion of all events, at approximately 150 mbsf a low velocity zone becomes visible between OBS stations 1 and 4. It is more pronounced between the OBS locations and appears to be interrupted beneath OBS 3. Towards BSR depth v_P increases to approximately 2000 m/s. Again, a zone of decreased v_P is constructed below the BSR with an extent very similar to the result using all events. The zones of increased v_P above the BSR and decreased v_P below are of smaller vertical extent compared to the previous result. Below the BSR zone similar behavior of v_P with depth can be observed for both results with the exception of a small-scale low-velocity zone approximately 200 m below the BSR between OBS stations 2 and 3. Its horizontal extent is less than 200 m.

When the time window is increasing with each frequency stage (Figure 5.2c) the result is similar to when a time window of 2 s after the arrival of the first multiple is used. Nevertheless, there are slight differences in the resulting v_P models which become apparent when looking at the shape of the increased v_P

zone above the BSR. In the interpretation of BSR zones (Section 6.1) differences are also notable.

The density which was inverted simultaneously with v_P is shown in Figure 5.3. The ρ models exhibit similar structures when compared to the v_P models. The circular artifacts close to the sources are clearly visible in the first time windowing approach. In all approaches a BSR signature with an increase in ρ above and a decrease below BSR depth is observable. In the second time windowing approach the updates in ρ, i.e., the parameter variations with depth, are stronger than in the first approach. In the result from the third approach the BSR contrast is visible more clearly than in the second. The BSR signature in all ρ models is horizontally more continuous than in the respective v_P model. The v_P distribution close to the seafloor is mimicked for the second and third approach.

To further evaluate the outcome of the different time windowing approaches, I compare the inverted source time functions and the misfit evolution in Figure 5.4. All three results show a high similarity of the STFs among the five OBS stations. The source time functions differ in their signature between the result of the approach using all events and the results of the approach using the reduced signal content. In the case of the inversion of all events the shape consists of one main maximum in the signal enclosed by two smaller minima, for the approach using only multiply reflected waves a smaller minimum is followed by a maximum, and another minimum and smaller maximum. In the case of the time window increasing at each frequency stage, the source time functions show a signal for only 0.5 s length corresponding to the length of the first time window. The misfit evolution shows that for all three approaches the strongest reduction can be achieved in the first frequency stage, where eight and ten iterations are executed for the first two and the third approach, respectively. For the next frequency stages only four iterations are executed with the exception of the last frequency stage in the first approach and the second stage in the third approach.

A similar discrepancy between inverting all events and the reduced signal content is visible in the comparison of the final seismograms (Figure 5.5). For the multiparameter inversion the direct wave signature is fitted well in amplitude when using the full signal content. In the result of inverting the reduced signal content the mismatch in amplitude is more significant although the mismatch in phase is similar to the result of inverting all events. The fit of the multiply reflected signals is better in the inversion with the reduced signal content. The phase of reflections after the first multiple is fitted only by the inversion using the reduced signal content.

5.2.2 Monoparameter inversion

Synthetic tests show that a contrast in v_P only, such as it is typical at the BSR, is also constructed in the density model, when a simultaneous inversion for v_P and ρ is executed (cross talk). Therefore, the same time-windowing approaches as before are executed in three tests with a monoparameter v_P inversion. The resulting v_P models are shown in Figure 5.6. In the first approach the same artifacts around the OBS positions are visible with slightly reduced amplitude. The general v_P behavior with depth is very similar to the result of the simultaneous inversion for v_P and ρ. The BSR signature in v_P is appearing to be more continuous and the vertical extent of the increased and decreased v_P zones is more even along the profile distance. The amplitude of the v_P contrast is similar in both results.

When using only the multiply reflected and the refracted wave signals (both with constant and increasing time window), the differences between simultaneous inversion of v_P and ρ compared to monoparameter v_P inversion are more pronounced. The v_P increase at the seafloor and decrease directly below is much stronger in amplitude. The same holds for the low-velocity zone between OBS stations 1 and 4, and for all other parameter contrasts constructed by FWI. The BSR velocity contrast is now continuously visible and the zones of increased and reduced v_P are more uniform in their vertical extent.

The inverted source time functions (Figure 5.7) are again consistent between all stations for every time windowing approach. The signatures for each approach are almost identical to the ones recovered from simultaneous inversion of v_P and ρ. Comparing the misfit behavior it is apparent that the progress of the inversions is similar to the previously discussed results. In the first frequency stage eight iterations are executed for the constant time windowing approaches and only four iterations in the following stages. For the increasing time windowing approach nine iterations are performed in the first stage, six in the following two and four in the final stage.

Figure 5.8 shows the final seismograms for monoparameter inversion. Similar observations as in the results from multiparameter inversion can be made. Here the amplitude mismatch is more comparable for all approaches in both the direct arrival and the multiples.

5.2.3 Comparison

A comparison of v_P depth profiles from the resulting models of all three time windowing approaches for simultaneous v_P and ρ inversion with monoparameter v_P is shown in Figure 5.9. It becomes apparent that in the approach using all events the differences between simultaneous and monoparameter inversion are much smaller than in the approaches without the direct wave and primary reflected signals. Especially the parameter contrasts near the seafloor become more pronounced. The BSR contrast appears sharper as well.

The corresponding ρ depth profiles are shown in Figure 5.10. For the time windowing approaches where the direct wave and primary reflections are disregarded stronger density variations with depth can be observed in the inversion results. In the two central depth profiles a signature mimicking the v_P BSR distribution is visible.

In Figure 5.11 the maximum velocity above and the minimum velocity below the BSR are compared for all results. Again, the recovered parameter distribution is similar for the approach using the full signal content whereas the other two results show strong differences between simultaneous v_P and ρ and monoparameter v_P inversion. For the first approach the determined v_P maximum above the BSR lies between 1.9 km/s and 2 km/s. For the other two approaches this also applies in the case of simultaneous v_P and ρ inversion whereas the maximum v_P values reach 2.1 km/s for monoparameter inversion. The v_P minimum below the BSR within the zone of a clear negative velocity contrast lies between 1.7 km/s and 1.85 km/s. At 8 km profile distance a v_P minimum of approximately 1.65 km/s is reached. The variation of the maximum and minimum v_P values is quite strong for all results with fluctuations of about 100 m/s within 100 m distance.

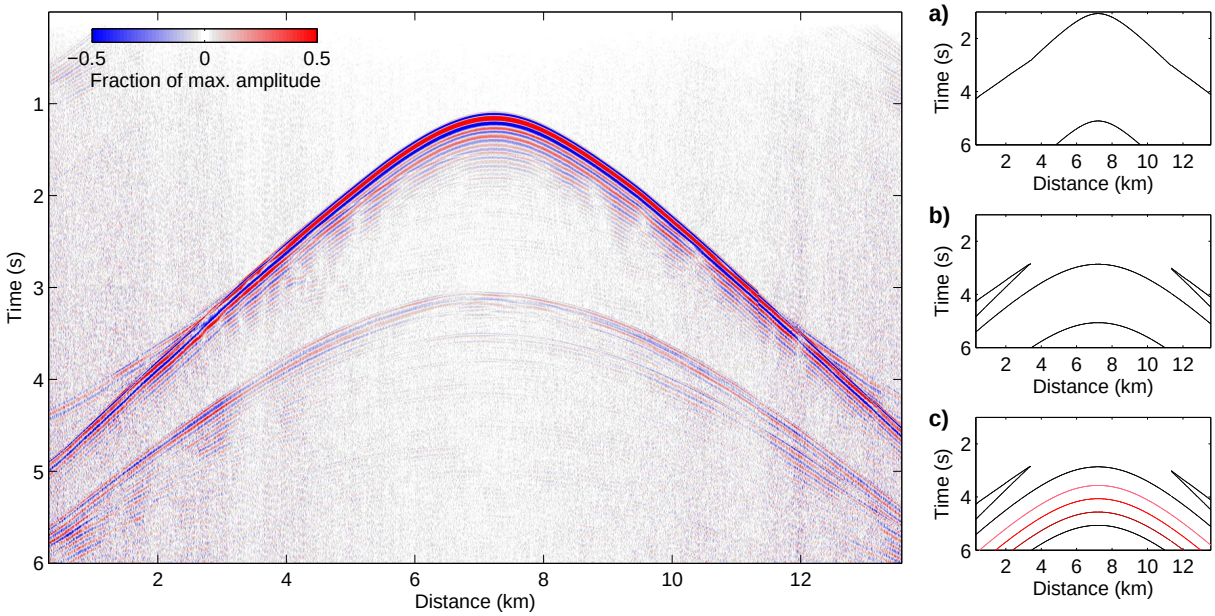

Figure 5.1: Exemplary seismogram (left) and time windows (right) applied in the inversion of data from profile P1. (a) All events, (b) without the direct wave and primary reflections, (c) same as (b) but with increasing time window.

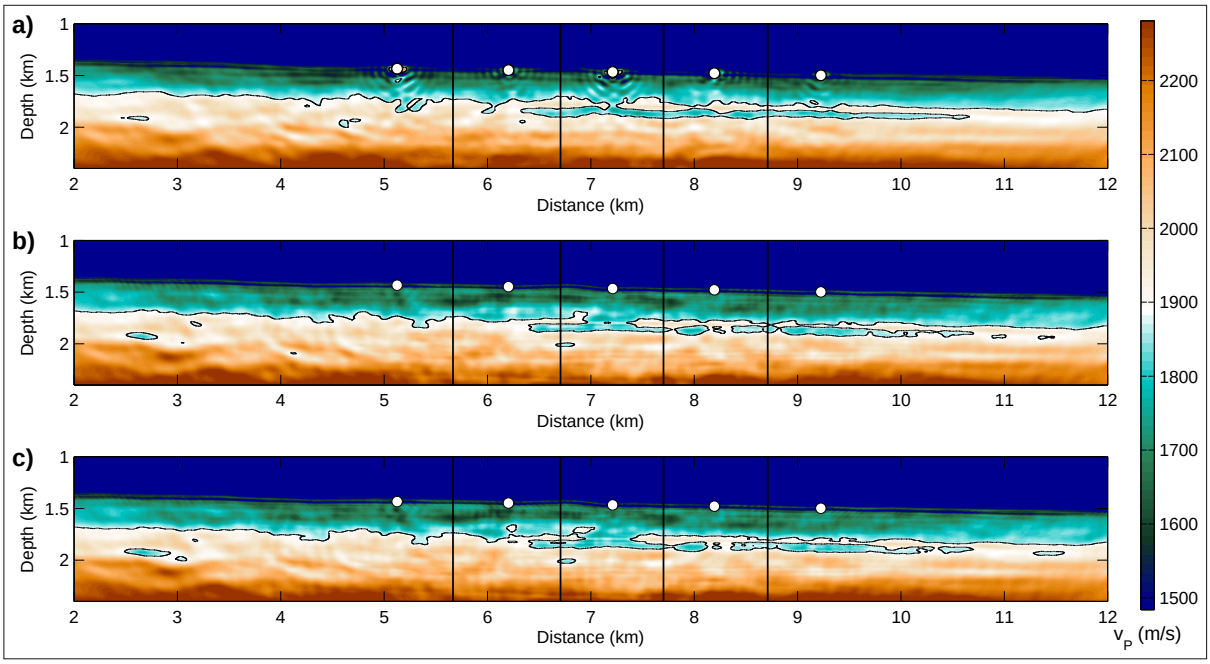

Figure 5.2: Resulting v_P models from inversion of data from profile P1. (a) Inversion with all events, (b) without the direct wave and primary reflections, (c) same as (b) but with increasing time window. Vertical black lines mark the locations of the depth profiles shown in Figure 5.9.

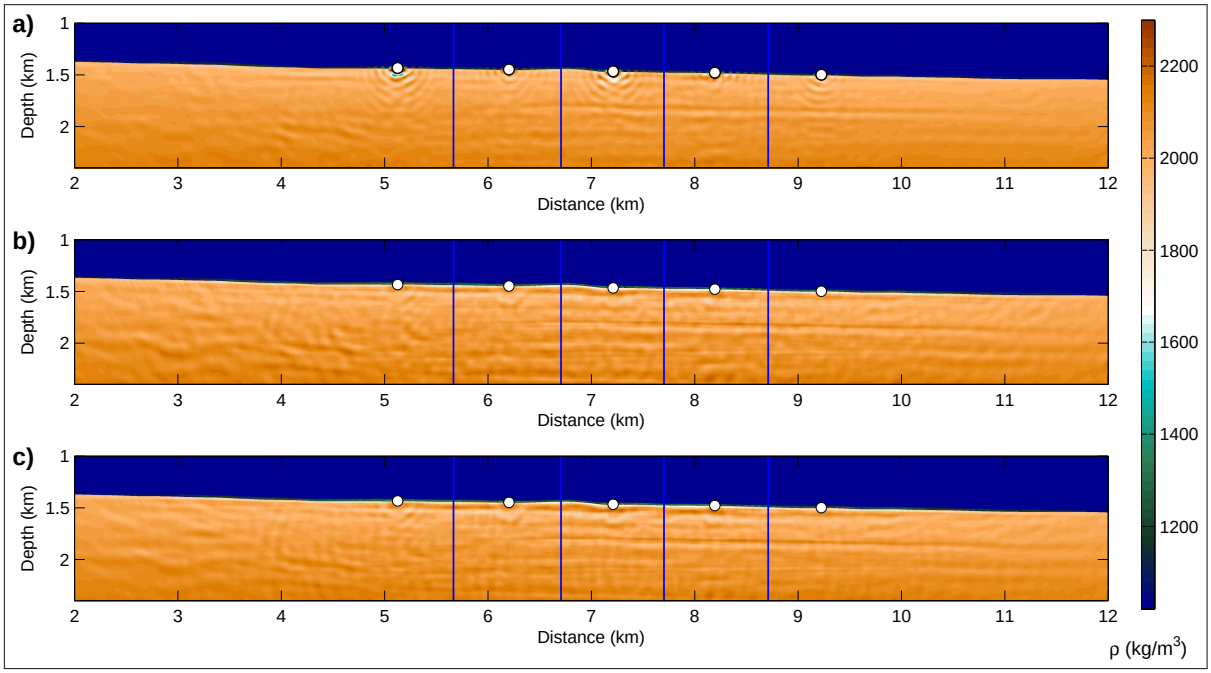

Figure 5.3: Resulting ρ models from inversion of data from profile P1. (a) Inversion with all events, (b) without the direct wave and primary reflections, (c) same as (b) but with increasing time window. Vertical blue lines mark the locations of the depth profiles shown in Figure 5.10.

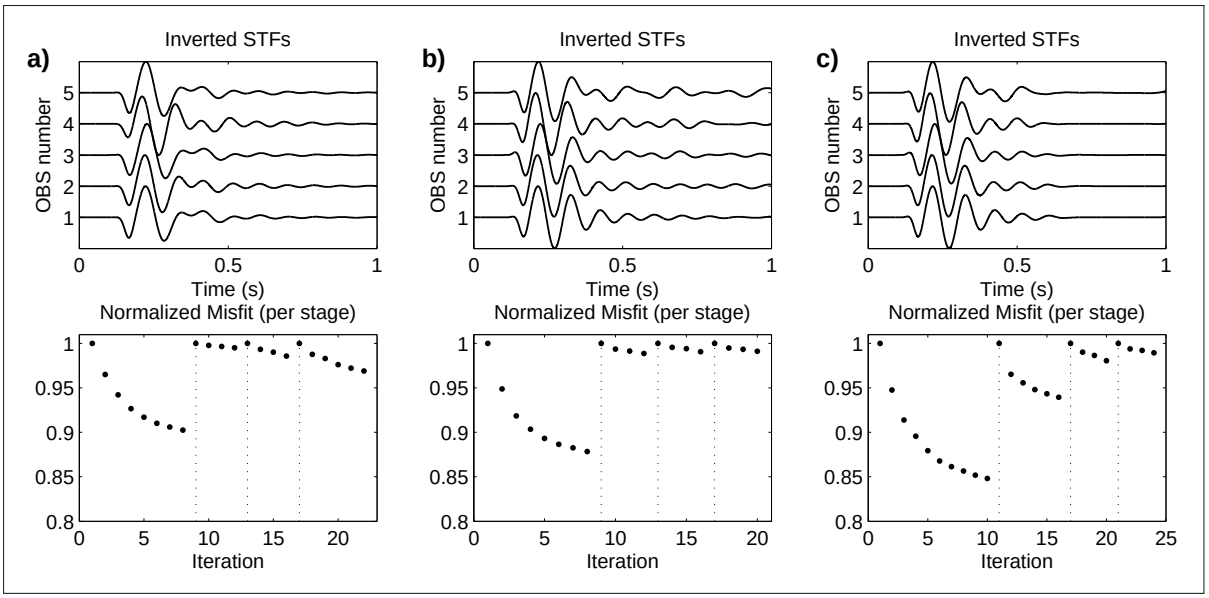

Figure 5.4: Source time functions (top) and misfit evolution (bottom) for profile P1. (a) Inversion with all events, (b) without the direct wave and primary reflections, (c) same as (b) but with increasing time window.

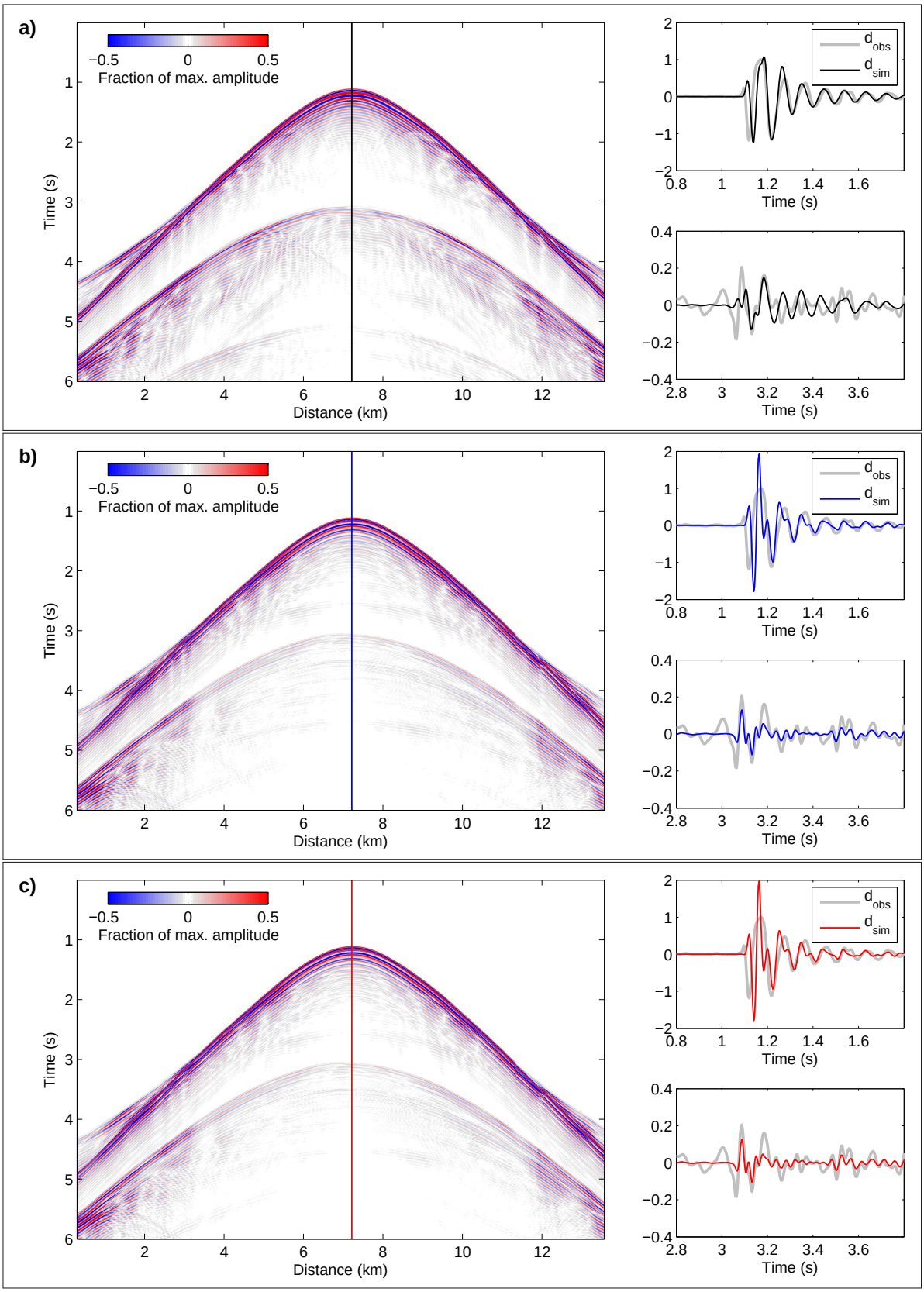

Figure 5.5: Final seismograms of OBS 3 for inversion of data from profile P1. (a) Inversion with all events, (b) without the direct wave and primary reflections, (c) same as (b) but with increasing time window. The vertical line in each seismogram image marks the location of the trace shown on the right.

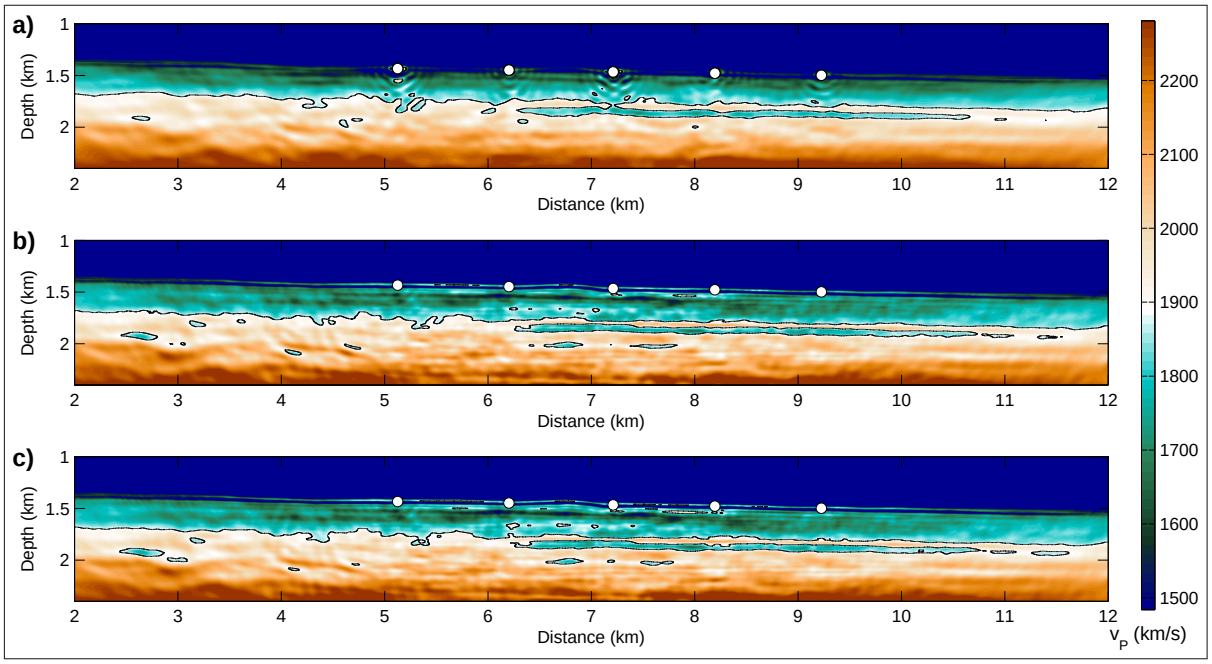

Figure 5.6: Resulting v_P models from monoparameter inversion of data from profile P1. (a) Inversion with all events, (b) without the direct wave and primary reflections, (c) same as (b) but with increasing time window.

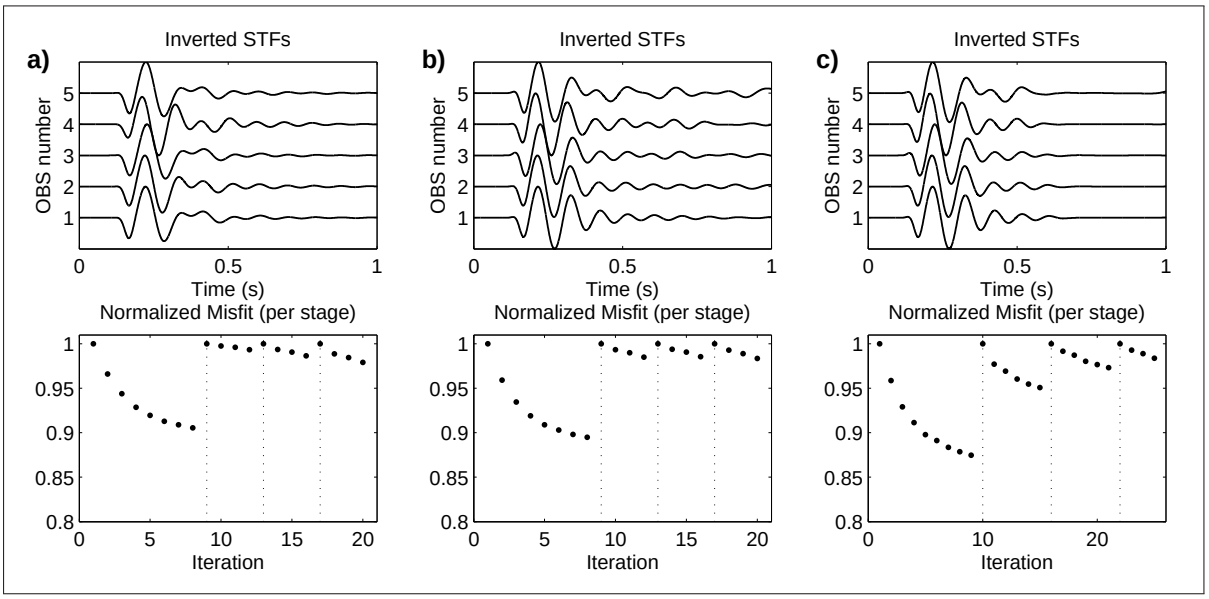

Figure 5.7: Source time functions (top) and misfit evolution (bottom) for monoparameter inversion of profile P1. (a) Inversion with all events, (b) without the direct wave and primary reflections, (c) same as (b) but with increasing time window.

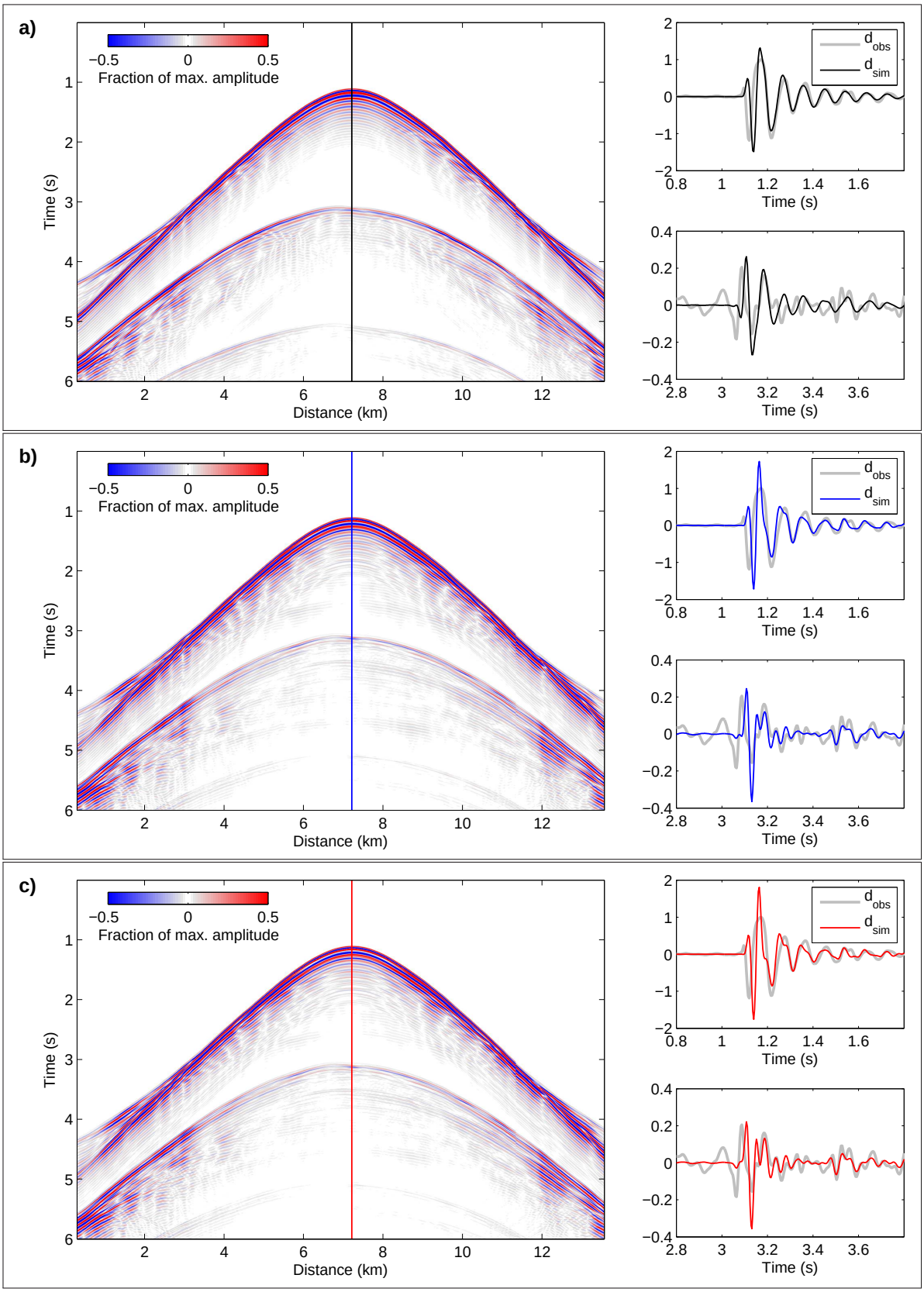

Figure 5.8: Final seismograms of OBS 3 for monoparameter inversion of data from profile P1. (a) Inversion with all events, (b) without the direct wave and primary reflections, (c) same as (b) but with increasing time window. The vertical line in each seismogram image marks the location of the trace shown on the right.

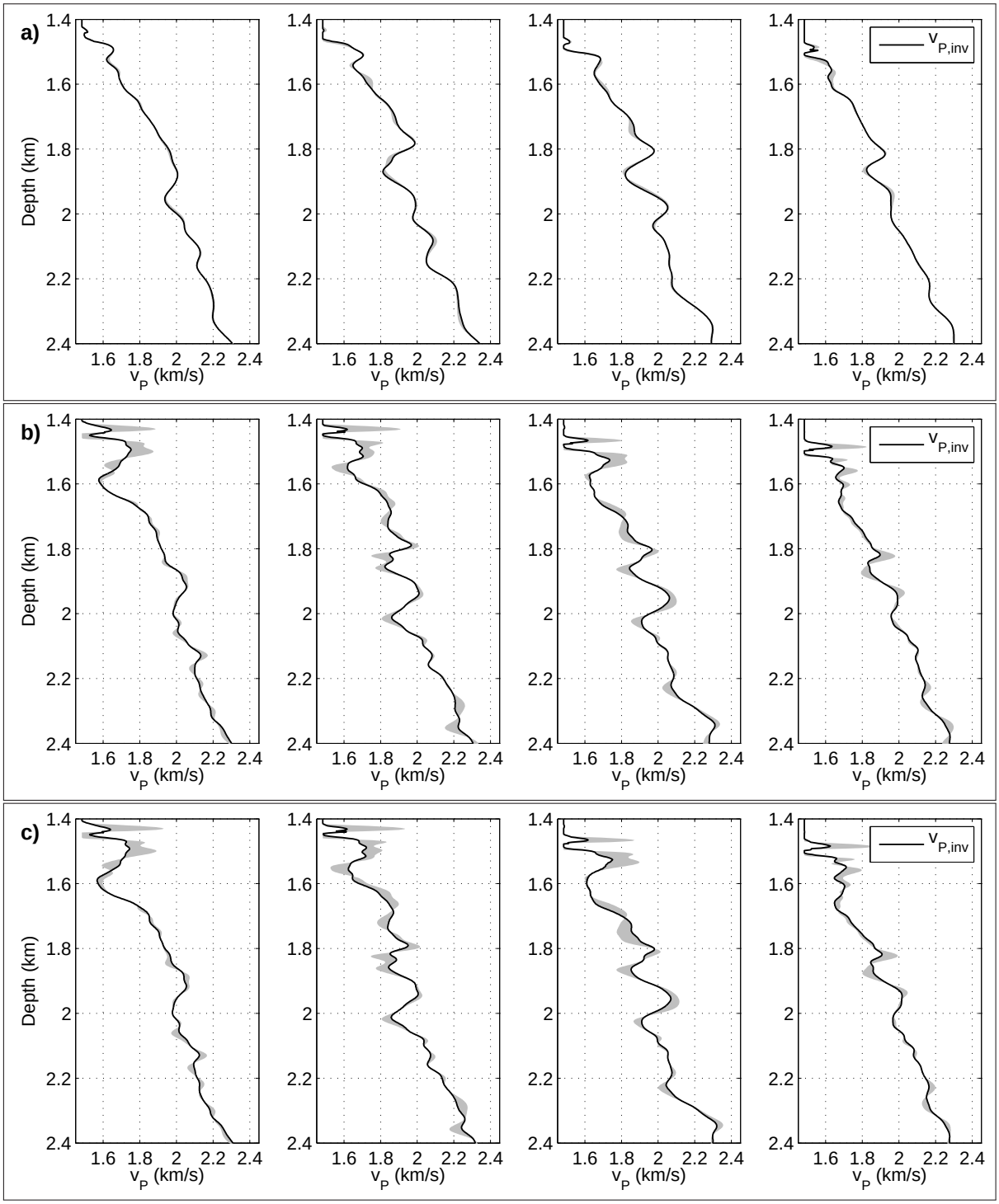

Figure 5.9: Comparison of v_P depth profiles for inversion results of profile P1. (a) Inversion with all events, (b) without the direct wave and primary reflections, (c) same as (b) but with increasing time window. Black lines show the resulting v_P with additional inversion for ρ, the shaded areas mark the differences to the result from monoparameter v_P inversion.

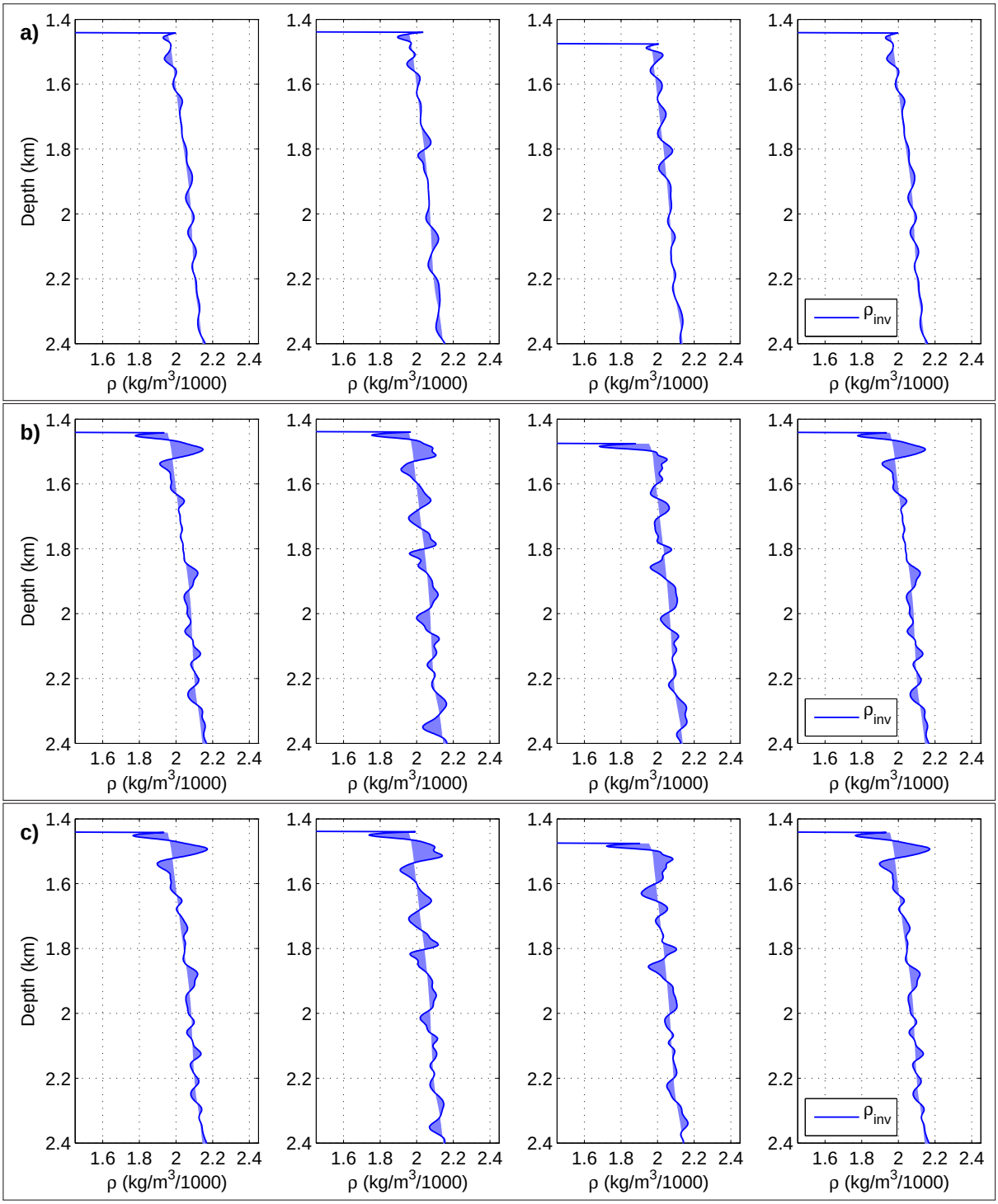

Figure 5.10: Comparison of ρ depth profiles for inversion results of profile P1. (a) Inversion with all events, (b) without the direct wave and primary reflections, (c) same as (b) but with increasing time window. Blue lines show the resulting ρ from inversion, the shaded areas mark the differences to the ρ starting model.

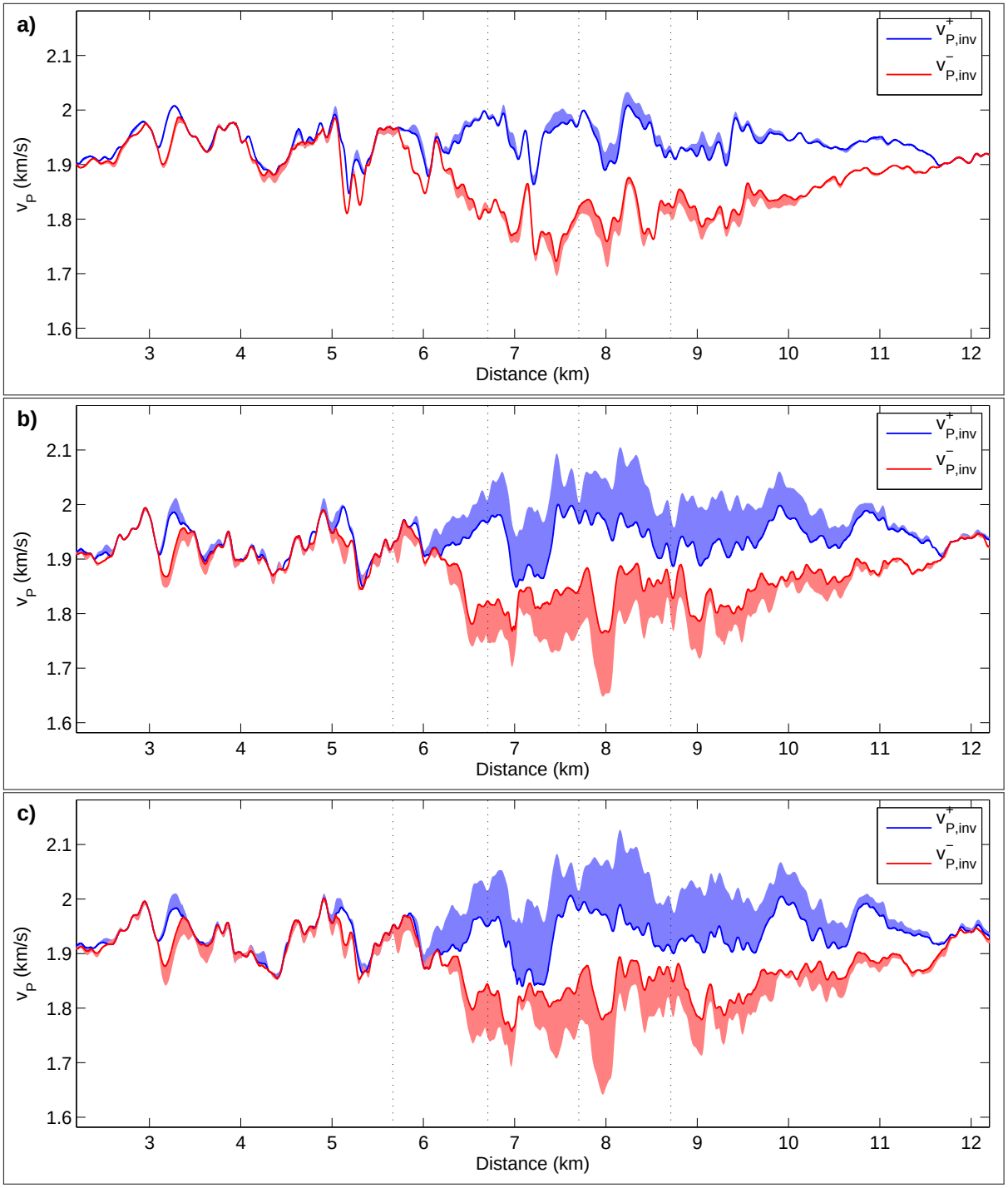

Figure 5.11: Comparison of BSR v_P distribution for inversion results for profile P1. (a) Inversion with all events, (b) without the direct wave and primary reflections, (c) same as (b) but with increasing time window. The blue and red lines show values for simultaneous inversion of v_P and ρ, the shaded areas mark the differences to the result from monoparameter v_P inversion. Vertical dotted lines mark the locations of the depth profiles shown in Figure 5.9 and 5.10.

5.3 Profile P2

At profile P2 data from 1691 shot positions were recorded at the same number of OBS stations as on profile P1 over a similar profile length. The shot spacing was 8 m on average compared to 10 m at profile P1. Towards the end of profile P2 the interfering signals from the concurrent commercial survey reduce the data quality significantly. The applied time windows for profile P2 are shown in Figure 5.12.

5.3.1 Multiparameter inversion

The resulting v_P models (Figure 5.13) show updates with similar characteristics as observed in the inversion results of profile P1. When using all events circular artifacts are constructed by FWI near some of the OBS positions as seen before. On profile P2 this is most noticeable at OBS stations 7 and 8. Similar to the results from profile P1, at the seafloor a slight v_P increase is constructed by FWI followed by a velocity drop underneath. Again this is more pronounced when using multiply reflected signals. In the shallow part of the model, again distinct low velocity zones are visible in the results of the time windowing approaches without the direct wave and primary reflected signals. On this profile they are located at approximately 200 mbsf between OBS stations 10 and 8 with some shallower zones with a lower v_P decrease between stations 8 and 6. At the expected BSR depth no distinct extended zones of increased velocity above and decreased velocity below are observed. For the approach using the full signal content (Figure 5.13 a)) a negative velocity contrast is constructed in the vicinity of OBS station 10 which appears to be continuous for a horizontal extent of approximately 1.5 km. The velocity contrast is less pronounced in the other results. For all three approaches a stronger increase of v_P towards the predicted BSR depth than in the starting model is observed, although there is no clear and continuous drop in v_P at this depth. Below the expected BSR v_P values remain at approximately 2 km/s down to 2.1 km to 2.2 km depth where a relatively consistent increase to 2.2 km/s can be observed along the profile.

Inverted ρ models (Figure 5.14) show again similar structures as constructed in the v_P models. The source artifacts in the approach using all events are clearly visible as well as parameter fluctuations similar to the structures of the inverted v_P. In contrast to the results from profile P1 no BSR signature can be observed at the predicted depth.

A comparison of the inverted STFs for profile P2 (Figure 5.15) shows that the signatures are less consistent than for profile P1. The signature of station 6 is shifted by almost half a period and differs in its general appearance from those of the other stations. The difference in signature between the approach using all events compared to the approaches with reduced signal content is the same as for profile P1. For the approach without the direct wave and primary reflected signals the signature of OBS 10 is inconsistent with those of stations 7 to 9. The signal-to-noise ratio is much lower for the data of station 10 compared to the other stations. Therefore, the source signature actually incorporates interference noise because the multiply reflected signals are of lower amplitude than the direct wave and primary reflections. The misfit progress is similar for all approaches, with the strongest decrease in the first frequency stage for six iterations with the all events and eight iterations with multiply reflected signals only. For the further frequency stages only in the second stage of the increasing time window approach more than four iterations are executed.

The seismogram fit for all approaches (Figure 5.16) yields comparable observations as for profile P1. Again, the phase fit of the multiply reflected wave signals is significantly better with the reduced signal content. A difference in the amplitude match of the direct wave arrival is visible when comparing the results from inverting all events and the time windowed data.

5.3.2 Monoparameter inversion

Inversion for v_P only for profile P2 shows similar results of the three approaches compared to those with a simultaneous inversion of v_P and ρ (Figure 5.17). In the results from the inversion of all events the artifacts near the OBS positions are slightly increased in amplitude. At the seafloor no significant changes of the v_P distribution between both approaches are visible. The zone with a BSR-like signature between 4.5 km and 6 km profile distance also appears to be similar in its extent and amplitude. When using the reduced signal content as input differences between the simultaneous and monoparameter inversion approaches become more apparent. Especially the velocity increase at the seafloor and the reduction below are more pronounced in the inversion result for v_P only. Furthermore, the shallow low-velocity zones are more distinctly visible. In general, parameter variations are of higher amplitude and zones with increased or reduced velocities compared to their surroundings are of increased horizontal extent.

Inverted STFs are again very similar to the results from the multiparameter inversion (Figure 5.18) with differences between the signatures of the all events compared to the reduced signal content and the deviation of the signature for OBS station 6 and, in the case of the reduced signal content, station 10. The misfit progress is also comparable to the multiparameter result with a significant decrease in the first frequency stage while in the later stages only four iterations each are executed.

Figure 5.19 shows the final seismograms from monoparameter inversion. The amplitude match of the direct wave arrival is more similar when comparing the approach using all events with the approaches using the reduced signal content than in the results from multiparameter inversion.

5.3.3 Comparison

A comparison of v_P depth profiles (Figure 5.20) shows that differences between both approaches are small when using all events. The difference in v_P is less than 50 m/s close to the seafloor and less than 10 m/s in the deeper part of the model. In the results from the reduced signal content differences in v_P are up to 200 m/s in the vicinity of the seafloor and reach approximately 50 m/s below 200 mbsf. The same observations hold for an increasing time window approach with the reduced signal content.

In Figure 5.21 the ρ depth profiles are shown. Again, stronger density variations with depth can be observed for the time windowing approaches where the direct wave and primary reflections are disregarded than in the inversion result from using all events. No signature mimicking the v_P BSR distribution can be found as at profile P1.

The determined v_P maxima and minima, above and below the BSR, respectively, show differences of up to 30 m/s for the v_P maxima and up to 20 m/s for the v_P minima when using the all events (Figure 5.22). Results from the reduced signal content lead to differences in the v_P maxima and minima of up to 80 m/s for the constant time window and up to 50 m/s for the increasing time window.

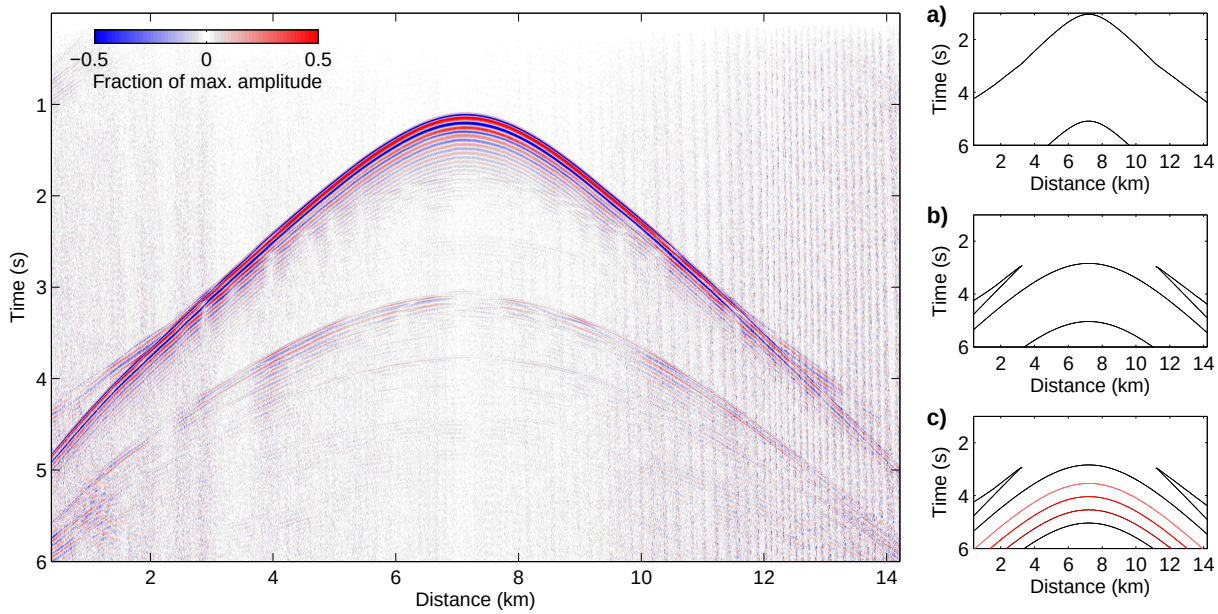

Figure 5.12: Exemplary seismogram (left) and time windows (right) applied in the inversion of data from profile P2. (a) All events, (b) without the direct wave and primary reflections, (c) same as (b) but with increasing time window.

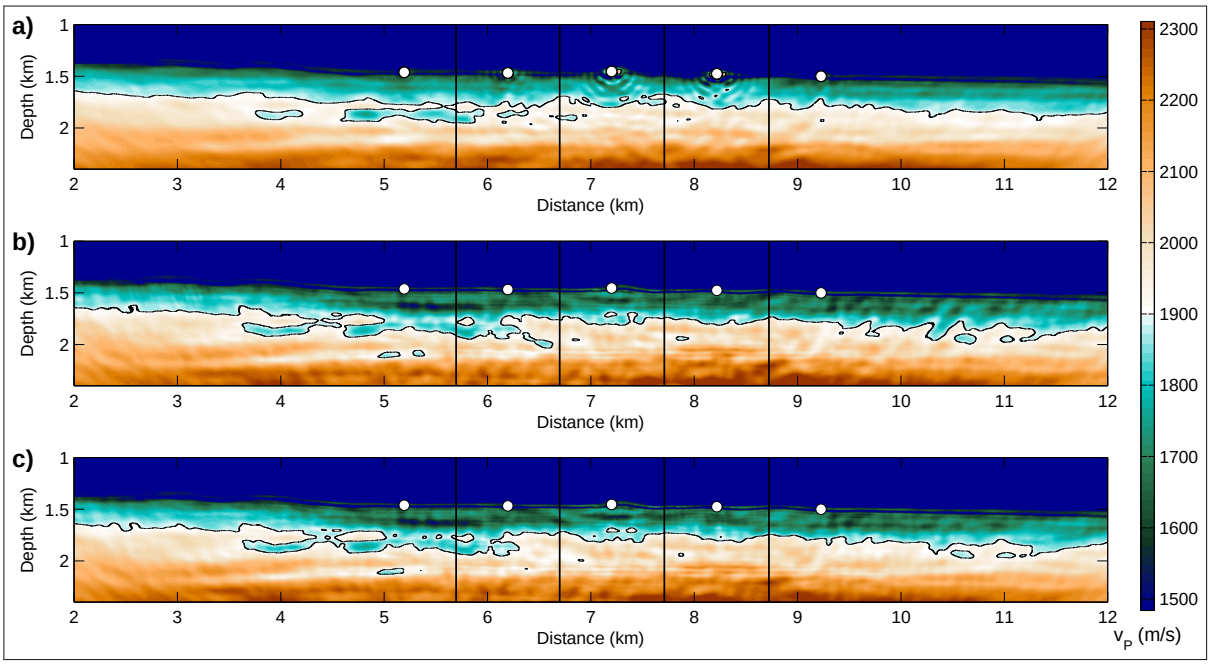

Figure 5.13: Resulting v_P models from inversion of data from profile P2. (a) Inversion with all events, (b) without the direct wave and primary reflections, (c) same as (b) but with increasing time window. Vertical black lines mark the locations of the depth profiles shown in Figure 5.20.

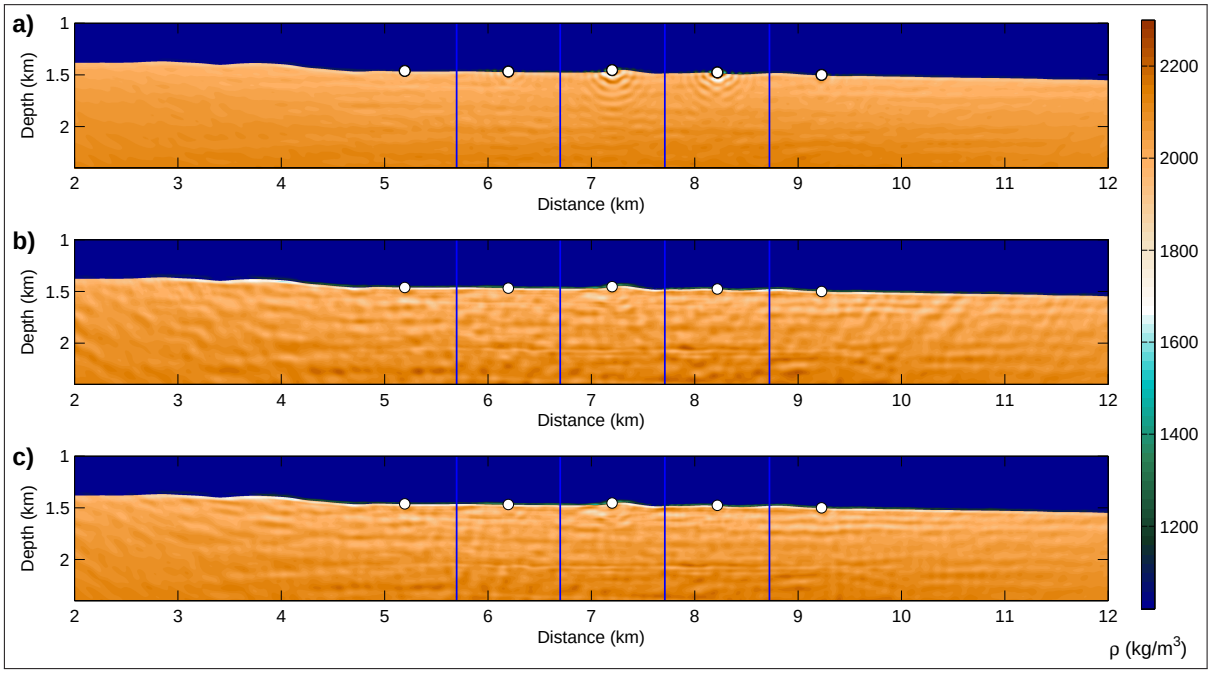

Figure 5.14: Resulting ρ models from inversion of data from profile P2. (a) Inversion with all events, (b) without the direct wave and primary reflections, (c) same as (b) but with increasing time window. Vertical blue lines mark the locations of the depth profiles shown in Figure 5.21.

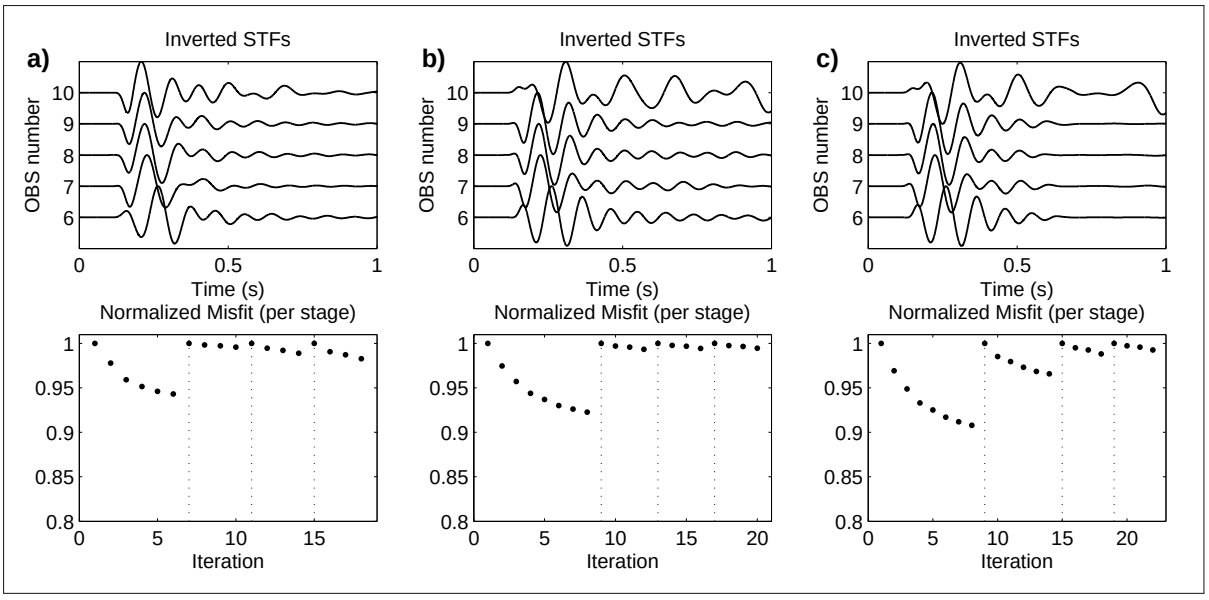

Figure 5.15: Source time functions (top) and misfit evolution (bottom) for profile P2. (a) Inversion with all events, (b) without the direct wave and primary reflections, (c) same as (b) but with increasing time window.

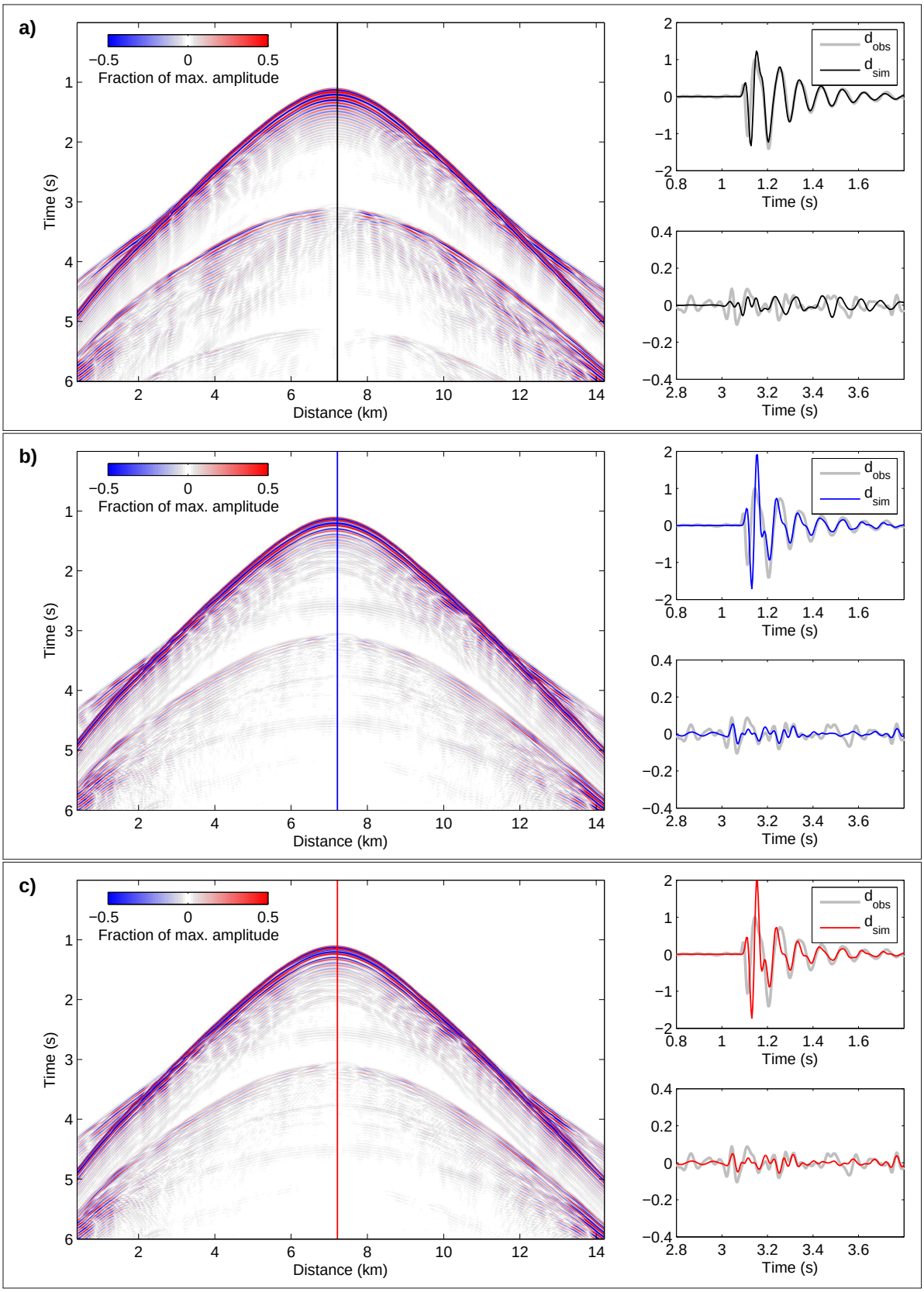

Figure 5.16: Final seismograms of OBS 8 for inversion of data from profile P2. (a) Inversion with all events, (b) without the direct wave and primary reflections, (c) same as (b) but with increasing time window. The vertical line in each seismogram image marks the location of the trace shown on the right.

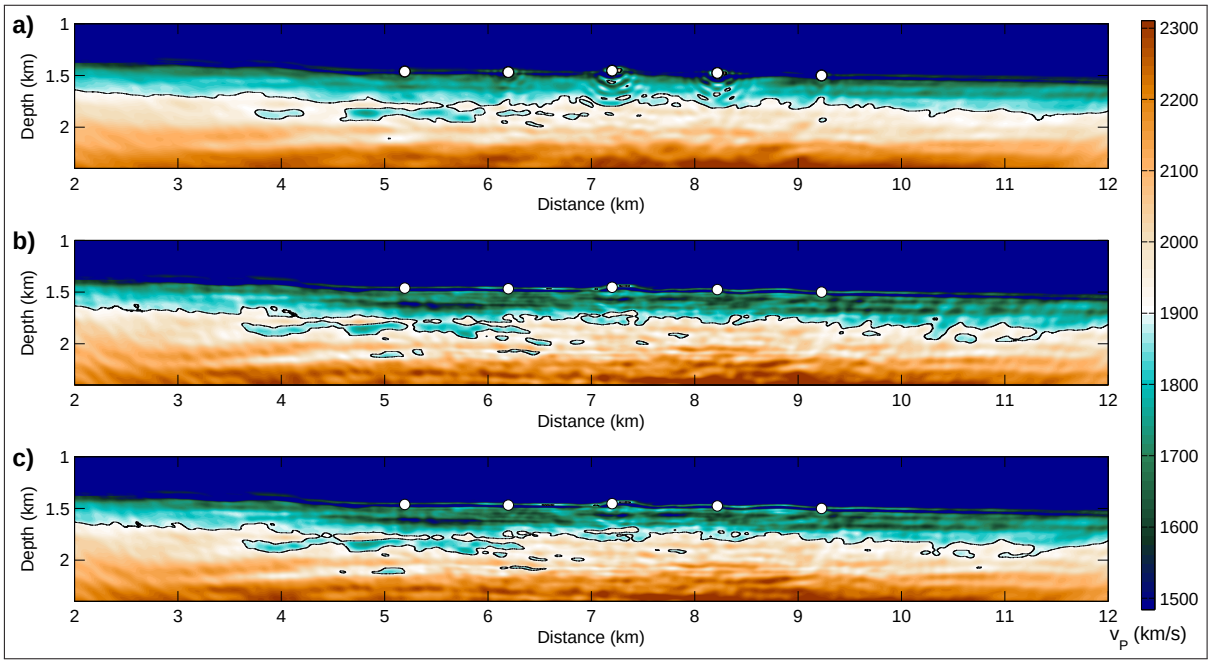

Figure 5.17: Resulting v_P models from monoparameter inversion of data from profile P2. (a) Inversion with all events, (b) without the direct wave and primary reflections, (c) same as (b) but with increasing time window.

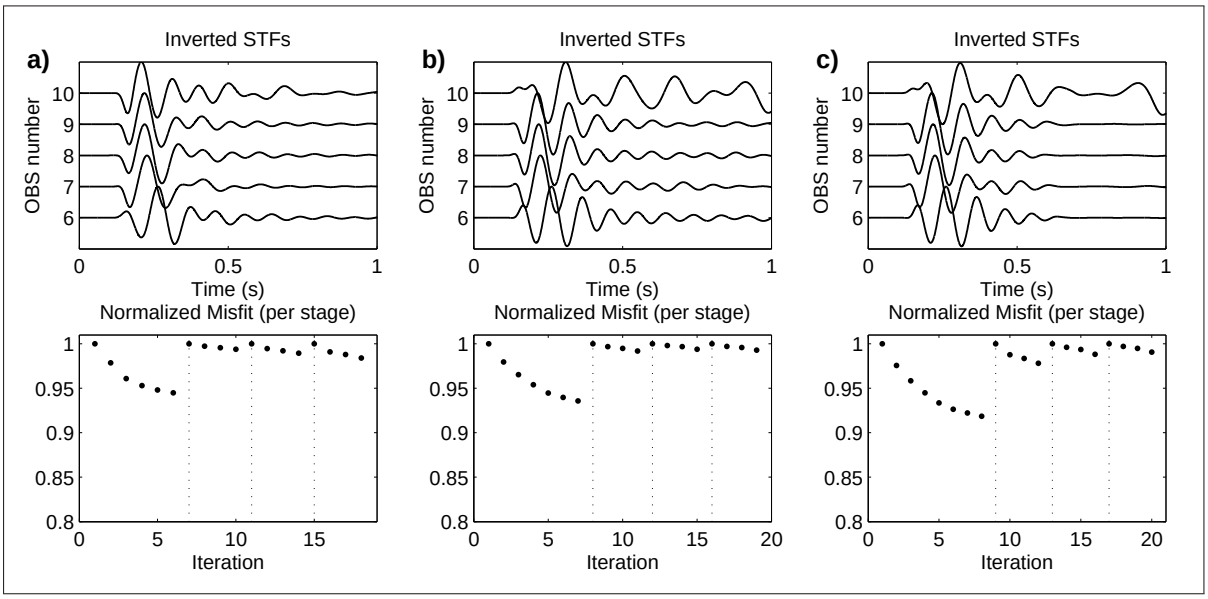

Figure 5.18: Source time functions (top) and misfit evolution (bottom) for monoparameter inversion of profile P2. (a) Inversion with all events, (b) without the direct wave and primary reflections, (c) same as (b) but with increasing time window.

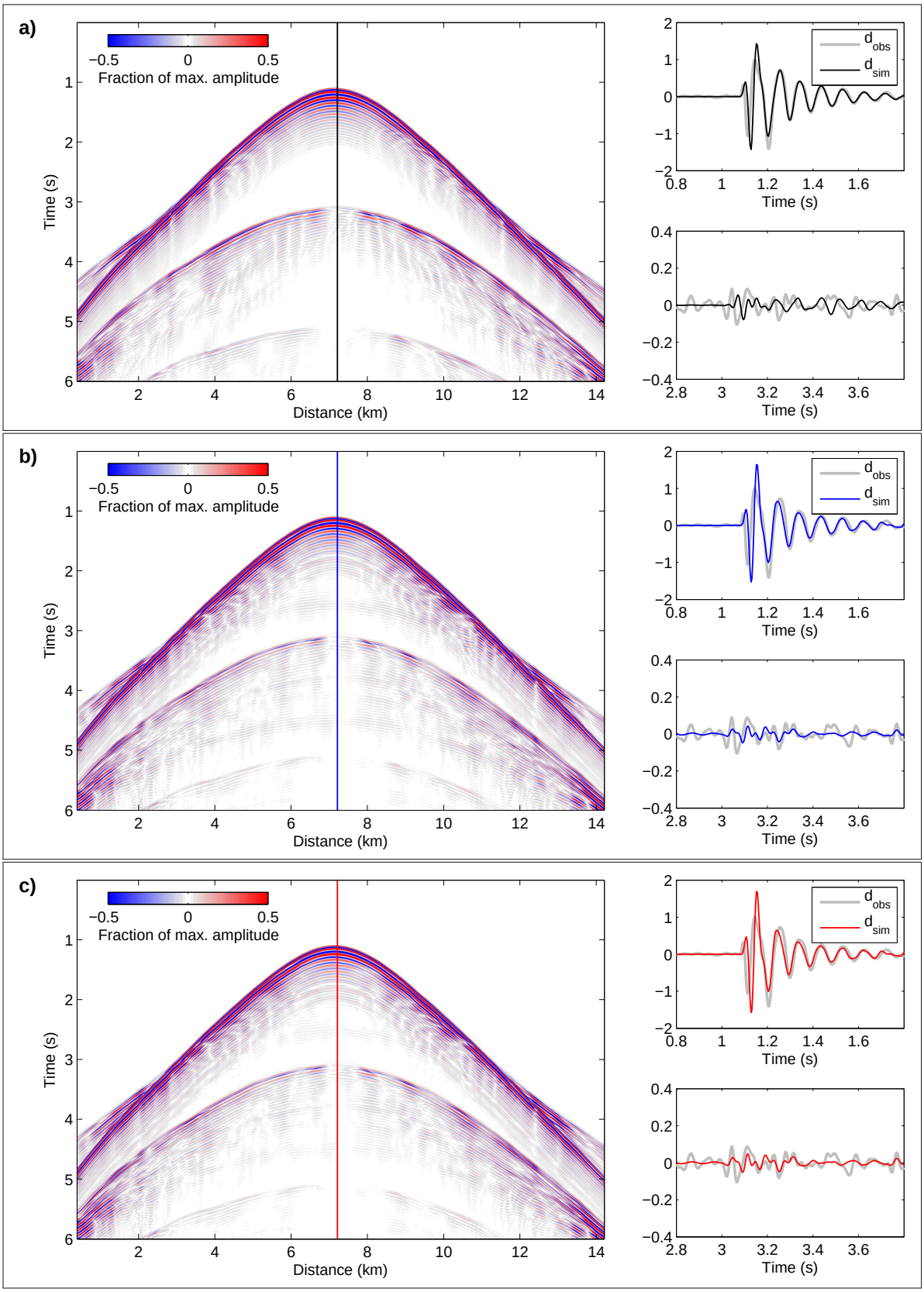

Figure 5.19: Final seismograms of OBS 8 for monoparameter inversion of data from profile P2. (a) Inversion with all events, (b) without the direct wave and primary reflections, (c) same as (b) but with increasing time window. The vertical line in each seismogram image marks the location of the trace shown on the right.

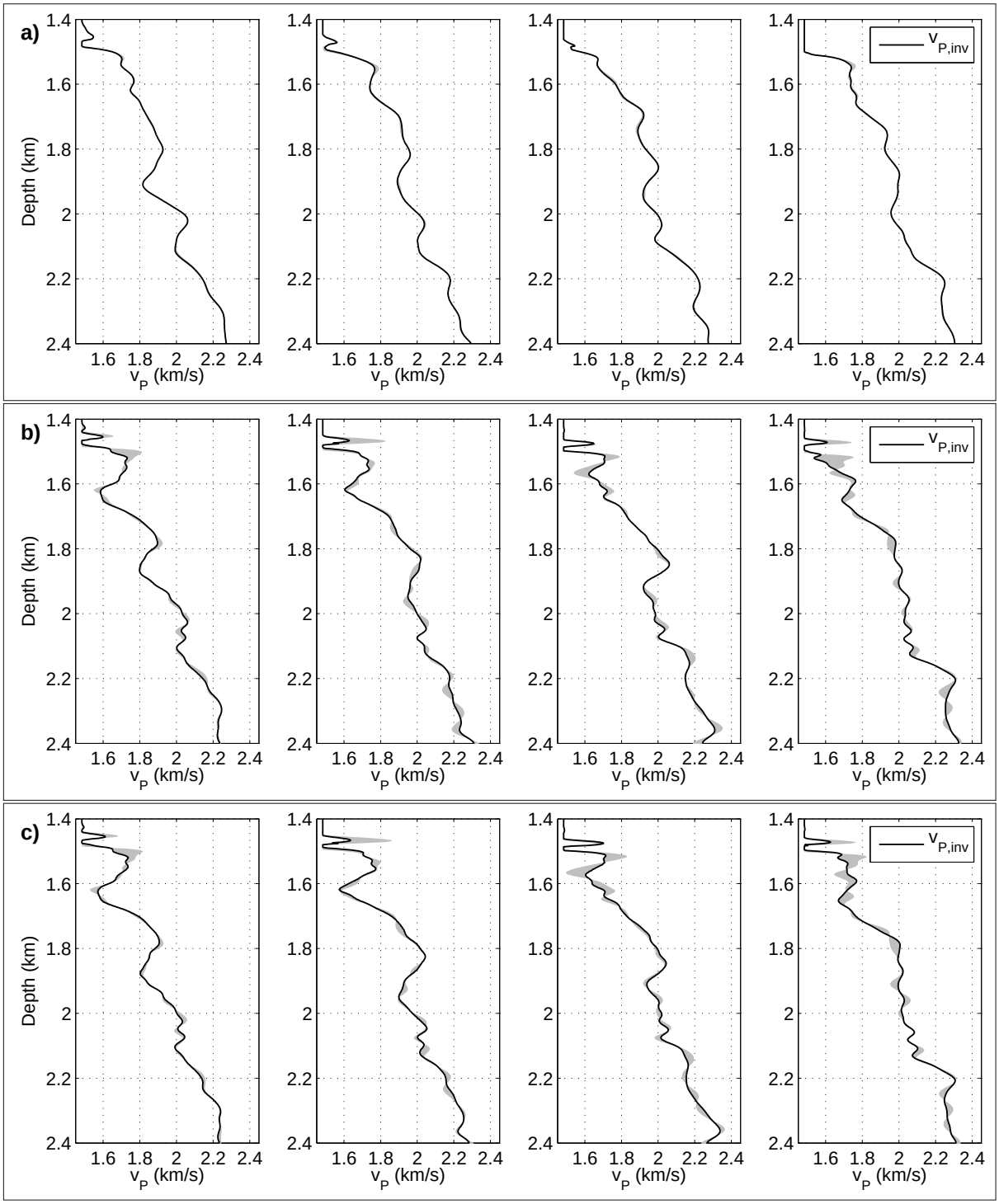

Figure 5.20: Comparison of v_P depth profiles for inversion results of profile P2. (a) Inversion with all events, (b) without the direct wave and primary reflections, (c) same as (b) but with increasing time window. Black lines show the resulting v_P with additional inversion for ρ, the shaded areas mark the differences to the result from monoparameter v_P inversion.

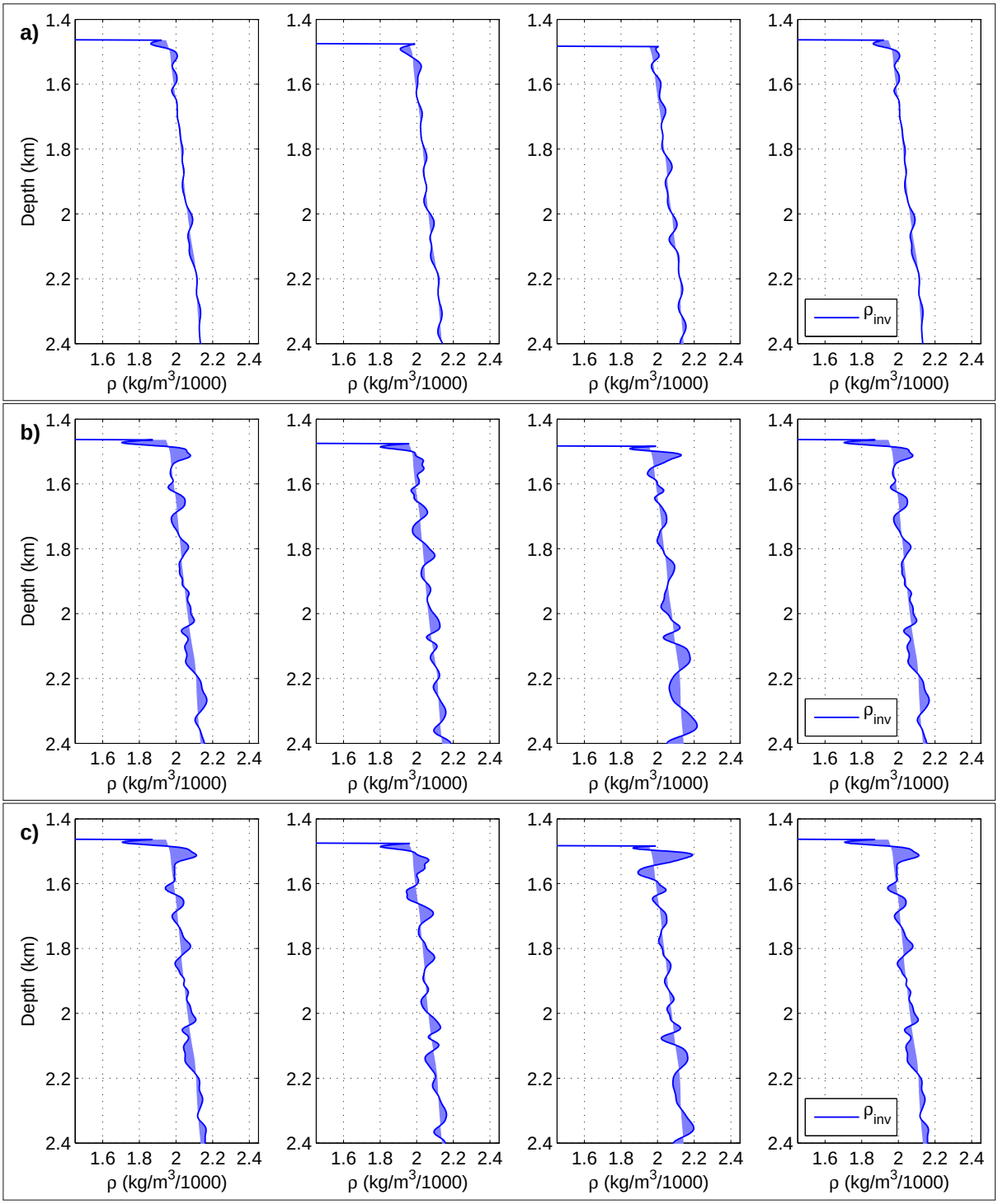

Figure 5.21: Comparison of ρ depth profiles for inversion results of profile P2. (a) Inversion with all events, (b) without the direct wave and primary reflections, (c) same as (b) but with increasing time window. Blue lines show the resulting ρ from inversion, the shaded areas mark the differences to the ρ starting model.

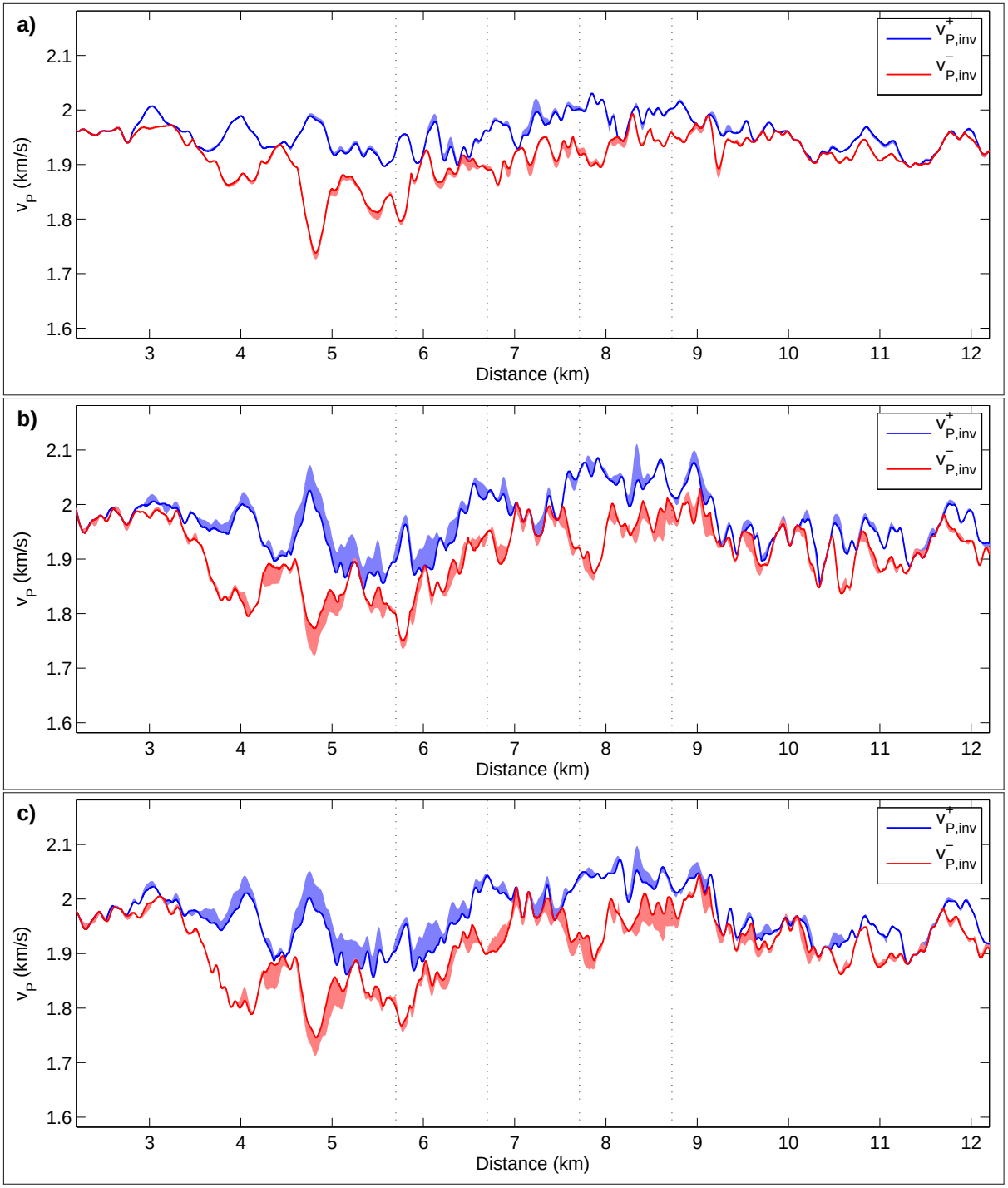

Figure 5.22: Comparison of BSR v_P distribution for inversion results for profile P2. (a) Inversion with all events, (b) without the direct wave and primary reflections, (c) same as (b) but with increasing time window. The blue and red lines show values for simultaneous inversion of v_P and ρ, the shaded areas mark the differences to the result from monoparameter v_P inversion. Vertical dotted lines mark the locations of the depth profiles shown in Figure 5.20 and 5.21.

5.4 Summary

In conclusion, I observe significant differences in the inversion results for the applied time windowing approaches and multi- versus monoparameter inversion. Comparing inversion results for all events against the reduced signal content I notice stronger parameter fluctuations at the seafloor with reduced signal content. Obviously, the multiply reflected signals are more sensitive to the parameter contrast at the seafloor and stronger model changes are introduced by the inversion. When using all events circular artifacts at the OBS positions can be observed which are stronger for stations where potentially a larger deviation in the true location compared to the projection on the profile and corresponding seafloor depth are present. Even around stations where the circular artifacts are of lower amplitude the shallow subseafloor parameter models are very homogeneous. The inversions with the reduced signal content reveal shallow low-velocity zones which occur on both profiles with v_P reduced by 100 m/s to 200 m/s. The occurrence of a BSR signature in the inverted models, as largely observed on profile P1, is independent of the approach while the vertical extent of high- and low-velocity zones as well as the amplitude of the velocity contrast is noticeably influenced. At profile P2 no indications for an extended hydrate and gas zone are observed. Differences in the resolution of the BSR signature are also related to the different signatures of the inverted source time functions. They also clearly affect the data fit. A drawback from using the reduced signal content is the failure in recovering a reliable source time function with data which is highly affected by noise because of lower signal amplitudes compared to the direct waves and primary reflections as observed on profile P2 for OBS 10.

The third proposed time windowing approach includes an increasing time window, providing a slightly better misfit reduction, and leads to shorter source time functions which show less reverberations. All in all, the resulting models from the increasing time window approach are comparable with those from the constant time window approach. Small differences in the amplitudes of parameter variations and the shape of structures can be observed. These observations can be used to evaluate the reliability of smaller structures.

Comparing the result of v_P from multiparameter inversion with the monoparameter inversion model it becomes apparent that the differences between both approaches are more pronounced in the results from the reduced signal content. The differences between results with the full signal content are small and mostly below 50 m/s. The strongest differences from the inversion with the reduced signal content exceed 300 m/s at the seafloor and reach approximately 150 m/s at the BSR at profile P1. Differences at BSR depth are slightly lower with less than 80 m/s for profile P2.

6 Evaluation

Results from FWI are influenced by assumptions made on the physics describing wave propagation, starting parameter models, and the chosen settings controlling the inversion process. Following an independent evaluation of the results, it is therefore necessary to cross-check the outcome with further available information and verify the recovered parameter changes quantitatively.

At first, based on the BSR horizons from the reflection seismic streamer data zones of likely hydrate and gas occurrence are determined. Then, a plausibility check of the inverted models is performed by comparing them to the seismic streamer sections which were recorded in parallel to the OBS data. An image of the reflectivity of the underground for both analyzed profiles was calculated from streamer data by true-amplitude time migration and depth conversion was achieved using a velocity model from regional seismic measurements (T. Zander, pers. communication, 2015, also compare Zander et al., 2017). The reflectors are compared to parameter changes in the models resulting from acoustic FWI.

In a further step the inverted models are analyzed in terms of potential hydrate and gas occurrence. Empirical relations are employed to link the final parameter models with hydrate and gas saturation.

6.1 Delineation of hydrate and gas zones

In this section an evaluation of the resulting parameter models is developed for the approaches discussed in Sections 5.2 and 5.3. To determine potential sites of hydrate and gas occurrence the BSR depth interpreted from the reflection seismic measurements is utilized. Along the profile for each distance the maximum and minimum v_P values are identified in the inversion result within 100 m above and below the BSR depth, respectively. Assuming the v_P maximum and minimum are located symmetrical to the BSR, a new BSR depth is determined at the midpoint between both. To determine the vertical extent of the potential hydrate and gas zones, the velocity value at the newly defined BSR depth is identified. The depth at which this value is reached again is found above the v_P maximum and below the minimum and is taken as the vertical limit for the respective zone.

Although it cannot be ruled out that hydrate and gas occur in patches, it is most likely that an uninterrupted zone of both is present as suggested by the continuous reflectors visible in the seismic streamer sections. Therefore, from both profiles a continuous zone is determined in which a negative velocity contrast at BSR depth is present. Starting at the position of the maximum contrast in v_P, the next position at which the v_P contrast decreases to zero is searched for to find the horizontal limit of the hydrate and gas zone.

An illustration of the determined potential hydrate and gas zones is shown in Figure 6.1. It implies that in the result of profile P1 the locations of the maximum and minimum v_P values are evenly distributed above and below the BSR from a profile distance of approximately 6 km on. The determined maximum

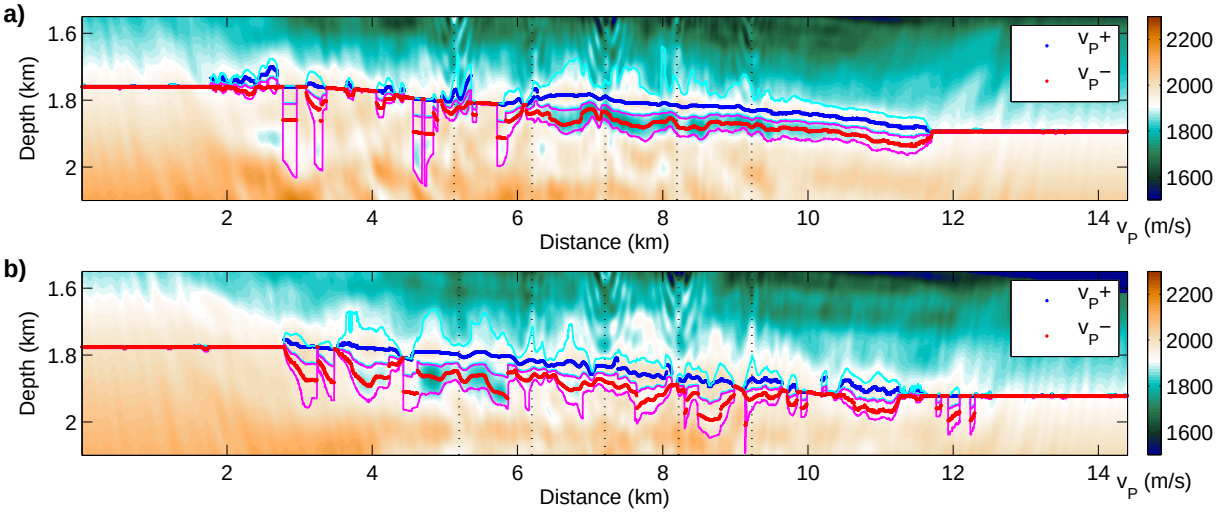

Figure 6.1: Delineation of potential hydrate and gas zones for profiles P1 (top) and P2 (bottom) for the multiparameter inversion results with the full signal content. The blue and red dots mark the determined v_P maxima and minima, above and below the BSR, respectively. The vertical extent of both zones is marked by cyan and magenta lines. Vertical dotted lines mark the locations of the OBS stations.

and minimum v_P values vary much more in depth at profile P2. The resulting zones of potential hydrate and gas occurrence and their overlap for the different approaches is shown in Figures 6.2 and 6.3 for profile P1 and P2, respectively.

The resulting values of the estimation of the horizontal and mean vertical extent of potential hydrate and gas zones can be found in Table 6.1 for profile P1 and in Table 6.2 for profile P2. In general, I find that the determined horizontal extent of both zones is clearly defined for profile P1 from approximately 6 km to 12 km profile distance while on profile P2 potential zones vary largely in horizontal extent and location with only little overlap in between results. The mean vertical extent of the potential hydrate and gas zones on profile P1 is largest for the inversion with the full signal content and is approximately 10 m smaller when using the reduced signal content. Results between multi- and monoparameter inversion are similar for the full signal content and vary up to 10 m between results with the same time windowing approach for the reduced signal content. The hydrate zone has an approximately 25 m higher vertical extent than the gas zone for the multiparameter inversion results and 20 m and 10 m higher in the monoparameter results for full and reduced signal contents, respectively. At profile P2 resulting hydrate zones have a higher mean vertical extent than the estimated gas zones but no consistent deviations between time windowing and inversion parameter approaches can be observed as also the location and horizontal extent of the zones differ between results. At both profiles the mean vertical extent of potential hydrate zones consistently varies between 60 m and 80 m and that of the gas zone between 40 m and 60 m.

Within the determined potential hydrate and gas zones the mean changes in v_P compared to the starting model are estimated from all grid points within the zones. In the hydrate zone v_P is increased by 50 m/s to 70 m/s for the multiparameter inversion of profile P1 and by up to 80 m/s for the monoparameter inversion. The decrease in v_P in the potential gas zone is between 25 m/s and 40 m/s for the multiparameter approach and approximately 50 m/s to 55 m/s for the monoparameter inversion. For the full

signal content the changes in v_P are stronger than from the reduced signal content in the multiparameter approach but similar to the other results from monoparameter inversion. At profile P2 the increase in v_P within the potential hydrate zone lies between 57 m/s and 85 m/s and the decrease in the estimated gas zone between 10 m/s and 45 m/s. Again, the results do not change consistently between approaches because of the difference in the location and horizontal extent of the potential hydrate and gas zones.

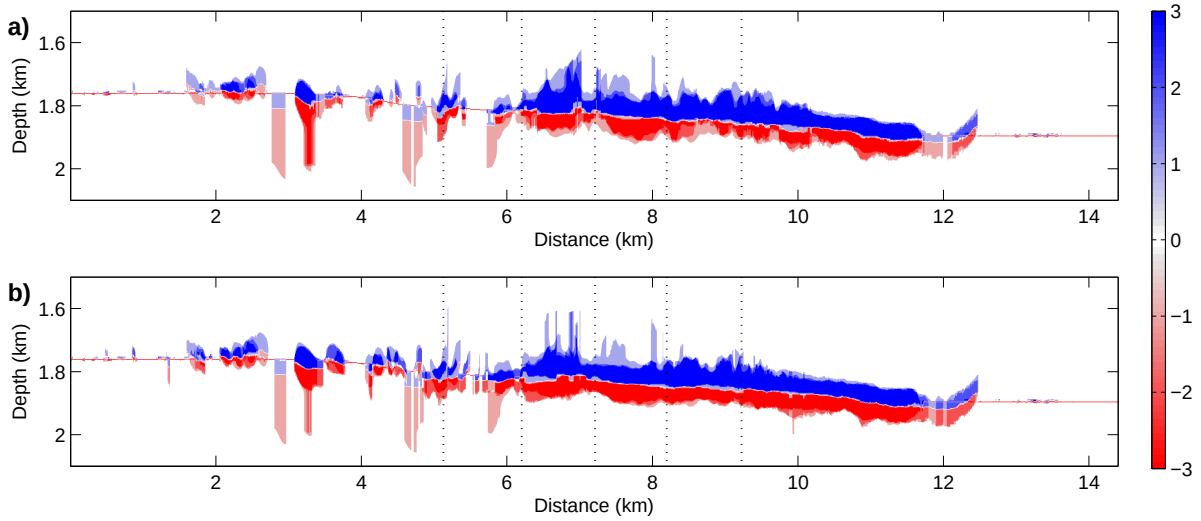

Figure 6.2: Evaluation of potential hydrate and gas zones for profile P1 for the (a) multiparameter and (b) monoparameter inversion. The blue and red areas show where hydrate and gas zones are estimated for the different approaches. The shade of color indicates the number of results contributing to the estimation.

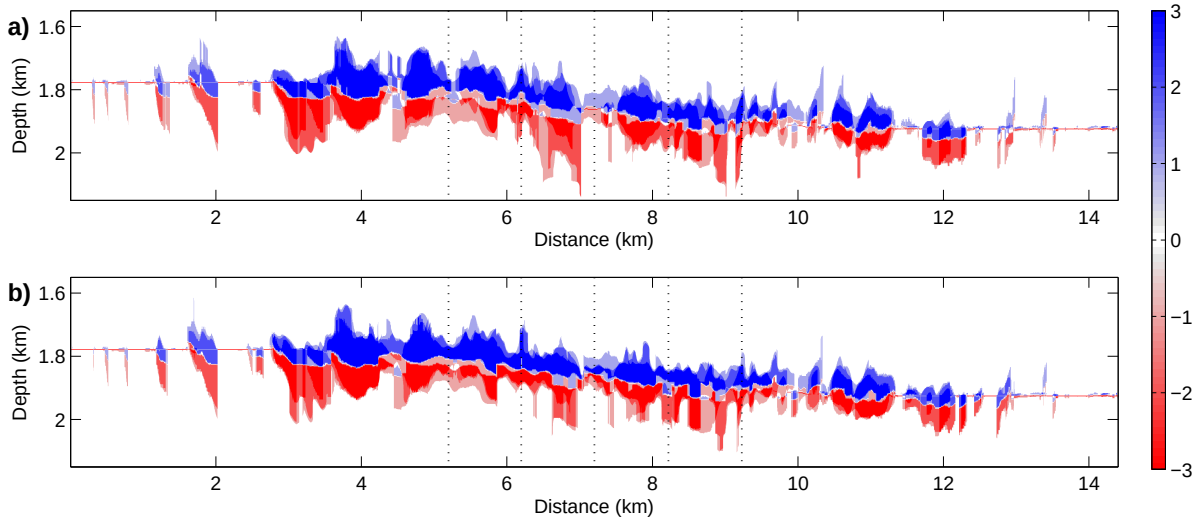

Figure 6.3: Evaluation of potential hydrate and gas zones for profile P2 for the (a) multiparameter and (b) monoparameter inversion. The blue and red areas show where hydrate and gas zones are estimated for the different approaches. The shade of color indicates the number of results contributing to the estimation.

Table 6.1: Interpretation of potential hydrate and gas zones at BSR depth for profile P1. Comparison between different time-windowing approaches (labeled (a), (b), (c) according to Chapter 5) and multiparameter (top three rows) versus monoparameter (bottom three rows) inversion.

	Horizontal extent (m)		Mean vertical extent (m)		Mean v_P change (m/s)		Extremal v_P values (m/s)	
	Start	End	Hydrate	Gas	Hydrate	Gas	$v_{P,max}$	$v_{P,min}$
(a)	6116	11710	82.4	56.0	69.5	-39.9	2008.5	1723.3
(b)	5774	11702	69.0	42.6	55.5	-26.3	2000.2	1765.0
(c)	6136	11986	69.8	45.2	52.6	-29.4	2006.7	1757.8
(a)	6176	11676	80.9	58.0	75.5	-48.4	2033.4	1695.7
(b)	5656	11786	63.4	50.0	79.8	-54.8	2105.5	1648.0
(c)	5664	12470	58.6	47.0	74.4	-51.2	2127.5	1641.5

Table 6.2: Interpretation of potential hydrate and gas zones at BSR depth for profile P2. Comparison between different time-windowing approaches (labeled (a), (b), (c) according to Chapter 5) and multiparameter (top three rows) versus monoparameter (bottom three rows) inversion.

	Horizontal extent (m)		Mean vertical extent (m)		Mean v_P change (m/s)		Extremal v_P values (m/s)	
	Start	End	Hydrate	Gas	Hydrate	Gas	$v_{P,max}$	$v_{P,min}$
(a)	4426	8128	68.9	52.4	77.5	-8.9	2030.5	1738.0
(b)	2722	5238	65.2	61.6	57.5	-36.0	2026.1	1773.2
(c)	3156	5228	80.8	62.5	60.5	-46.4	2011.4	1746.2
(a)	3518	7020	71.4	52.2	71.7	-20.4	1994.4	1726.4
(b)	5784	11722	69.3	44.7	57.5	-22.1	2005.5	1776.9
(c)	3192	9946	65.3	55.2	85.1	-11.1	2097.4	1712.7

The minimum and maximum v_P values within the respective zones lie between 2 km/s and 2.13 km/s for the hydrate and 1.64 km/s to 1.77 km/s for the estimated gas zone. At profile P1 the extremal values are similar for all time windowing approaches for the multiparameter inversion and differ in the monoparameter inversion by up to 100 m/s in the hydrate and by approximately 55 m/s in the gas zone. Differences between multiparameter and monoparameter inversion exceed 100 m/s in both zones for the inversions with the reduced signal content and are approximately 30 m/s to 35 m/s in the results gained from the inversion of the full signal content.

6.2 Comparison with seismic streamer sections

The reflectivity behavior in the seismic streamer data differs significantly between profiles P1 and P2 (compare Figure 6.4). In the first 200 mbsf of profile P1 a clear horizontal layering can be observed with less visible structures beneath this zone. A layer of approximately 60 m thickness characterized by parallel high-reflectivity amplitudes is starting at a profile distance of 6 km and continues up to 10 km at 400 mbsf. Down to 2.2 km depth additional layered structures of weak amplitude can be observed. At profile P2 the upper 200 m are characterized by more chaotic reflectivity patterns with a continuous horizon at 200 mbsf. Intermediate reflectivity amplitudes without discernible layering follow beneath. Horizontal layering is visible from 1.8 km depth at 4 km profile distance and from 1.9 km depth at 10 km profile distance. A zone of high-amplitude parallel reflections is visible above 2.2 km depth.

To compare the zones of different elastic parameters constructed by acoustic FWI to the reflectivity image, contour lines of specific v_P values of the previously discussed FWI results are overlain. The values chosen are 1700 m/s, 1900 m/s, and 2100 m/s. They align with different zones of characteristic reflectivity, the upper 200 mbsf, the vicinity of the interpreted BSR horizon and the depth of 2.2 km where a transition from stronger reflectivity amplitudes to significantly lower amplitudes occur. For comparison to the respective inversion results contour lines of the selected values are shown for the starting models of profiles P1 and P2 in Figure 6.5.

At profile P1 (Figure 6.6) the zones outlined by the three contour line values agree well with zones of different reflectivity behavior. For the results with the full signal content (Figure 6.6a) the high-amplitude reflector at 200 mbsf is approximately coincident with the 1700 m/s contour line but additional patches are outlined near the OBS positions. At OBS 1 and OBS 3 velocity values of 2100 m/s are exceeded in small areas. At the other stations smaller zones where velocities exceed 1700 m/s are visible. At BSR depth the 1900 m/s contour line marks the base of the high-amplitude reflectivity layer and horizontally extended patches above. The patches are disrupted below each OBS station for the result from multi-parameter inversion but is continuous from OBS 3 to OBS 5 for the monoparameter inversion result. The contour line of 2100 m/s follows a reflector at 2.2 km depth below which hardly any reflections are visible. The velocity contour does not fit the reflector below OBS 2 where a zone of higher amplitude reflections above the reflector is enclosed and below OBS 4 where the contour line fluctuates for approximately 1 km length.

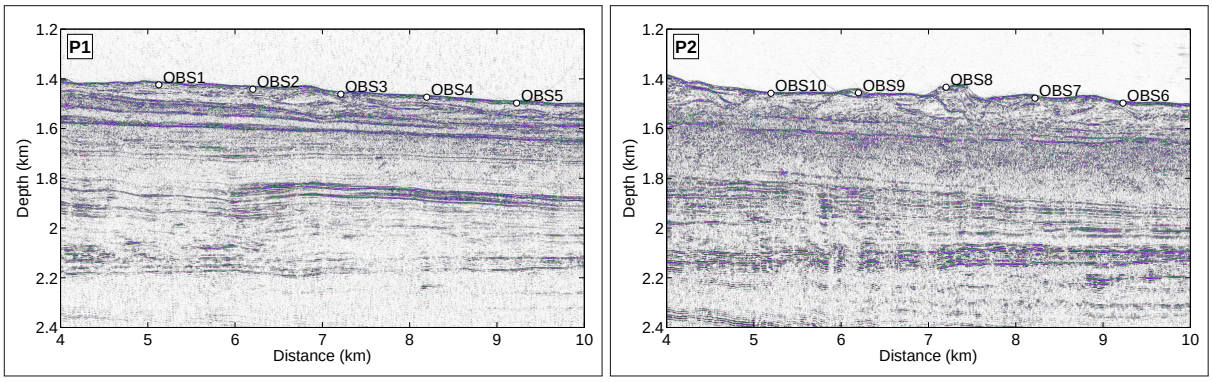

Figure 6.4: Migrated seismic streamer data of profiles P1 (left) and P2 (right).

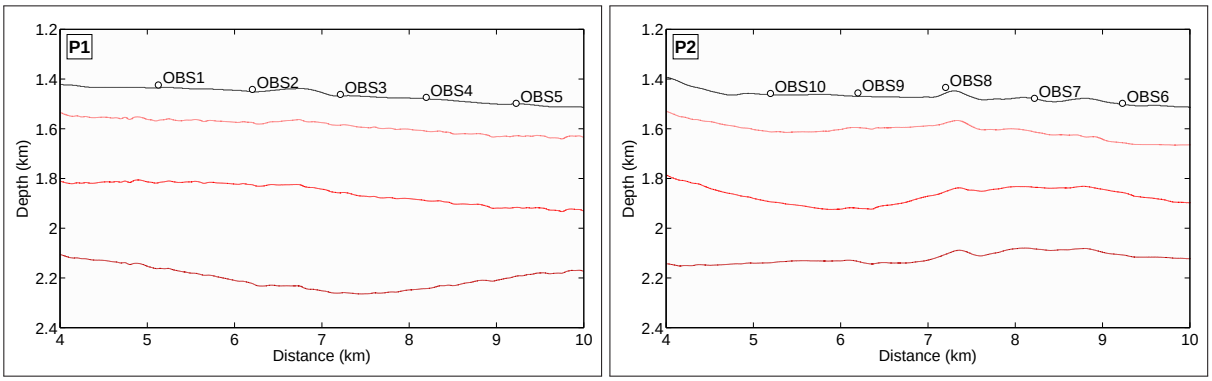

Figure 6.5: Contour lines of the starting v_P models of profiles P1 (left) and P2 (right). Light red: 1700 m/s, red: 1900 m/s, dark red: 2100 m/s.

When a time window is applied suppressing the direct wave and primary reflections (Figure 6.6b) more zones are outlined by the 1700 m/s contour line in the shallow model part. These zones are not continuous but align partly with some of the shallow reflectors for the multiparameter inversion. In the result from monoparameter inversion the zones outlined agree well with the shallow reflectors and are also consistent in their horizontal extent. The fit of the contour line with the high-amplitude reflector at 200 mbsf is inferior to the result from the full signal content. The high-amplitude reflections beneath the BSR are again outlined by the 1900 m/s velocity contour. Above the BSR the zones are more horizontally continuous than in the result from the full signal content for the multiparameter inversion. In the monoparameter inversion result the zone is uninterrupted from OBS 2 to OBS 5. The deepest visible horizontally continuous reflection at 2.2 km depth is again approximately followed by the 2100 m/s contour line. Beneath OBS 3 and OBS 4 the contour line lies deeper than the reflector. In the monoparameter inversion result more patches are outlined by the 1900 m/s and 2100 m/s contour lines between the BSR depth and the reflector marking the bottom of the visible reflections.

The results from an increasing time window approach without the direct wave and primary reflections (Figure 6.6c) is similar to the constant time window approach.

At profile P2 (Figure 6.7) the match between the contour lines and reflectors visible in the seismic streamer data is not as consistent as it is at profile P1. In the results with the full signal content (Figure 6.7a) the contour line at 1700 m/s is located approximately 100 mbsf and is only loosely aligned with visible reflections which are mostly discontinuous in this zone. Similar to the results for profile P1 close to OBS 7 and OBS 8 patches with velocities exceeding 2100 m/s are present and smaller patches reaching 1700 m/s are all oriented towards the OBS positions. The contour line at 1900 m/s fluctuates at approximately 300 mbsf with stronger vertical variation than at profile P1. Beneath OBS 10 it outlines a zone of 100 m vertical extent and 1.3 km length at 400 mbsf to 500 mbsf. Above this zone the contour lines roughly align with two reflectors. The contour line at 2100 m/s is in good agreement with the reflector at approximately 2.2 km depth, below which low-amplitude reflections occur.

Results from the inversion with the reduced signal content (Figure 6.7b) show a better agreement of the 1700 m/s contour line with the reflector at 200 mbsf. More patches are outlined in the shallow model region above it which do not align with the visible reflectivity patterns for the result from multiparameter

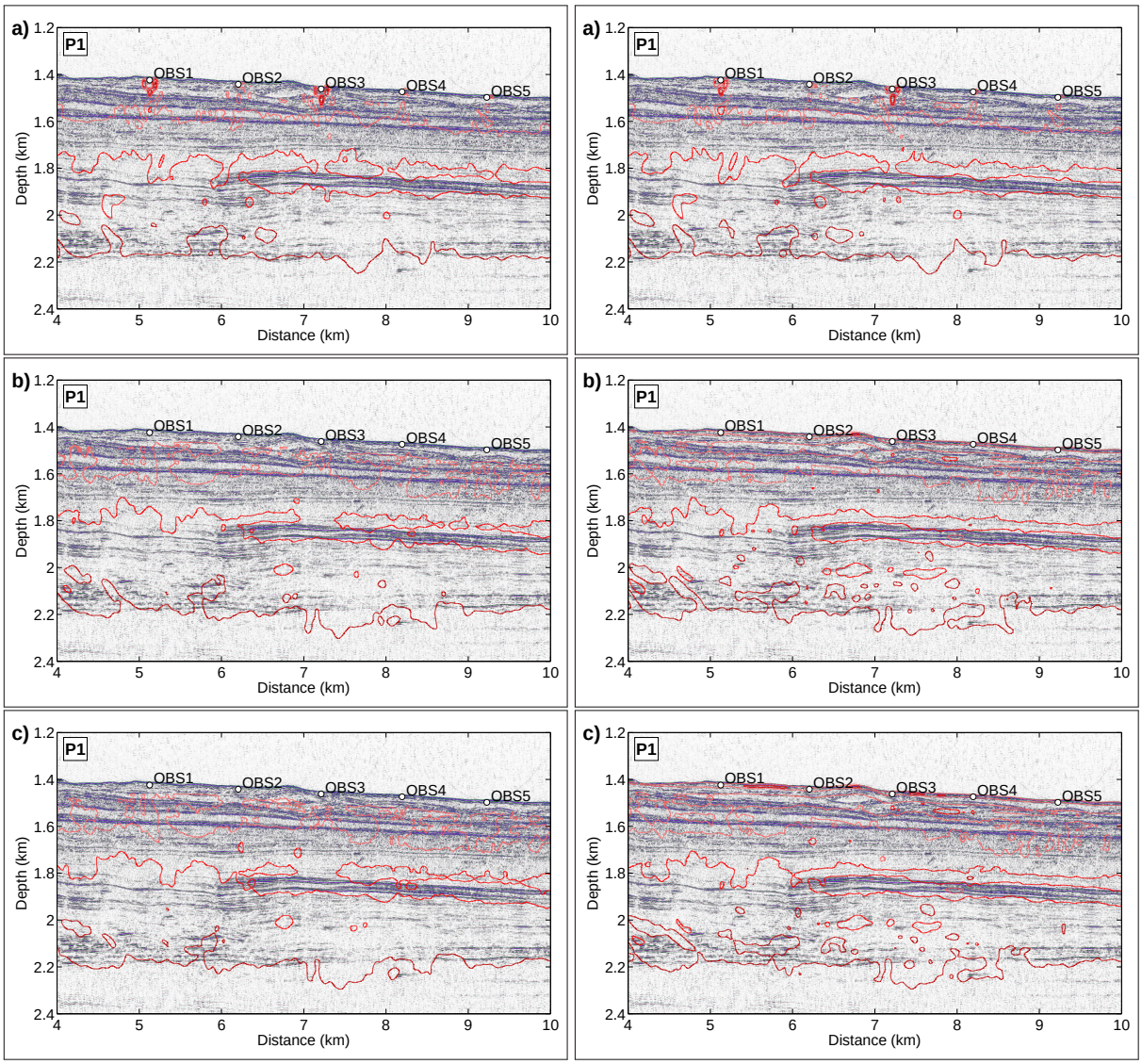

Figure 6.6: Inverted P-wave velocities from multiparameter (left) and monoparameter inversion (right) of profile P1 compared to seismic streamer data. (a) Inversion with full signals, (b) without direct wave and primary reflected signals, (c) same as (b) but with increasing time window.

inversion. In the result from monoparameter inversion the shallow patches are of higher horizontal continuity and partly align with reflectors. The 1900 m/s contour line exhibits similar properties than the one obtained from the result of the full signal content. In the multiparameter result the vertical fluctuations are smaller and there is no clear zone outlined beneath OBS 10 although the line lies deeper as well. In the monoparameter result the variation in the depth of the 1900 m/s contour line is higher than in the multiparameter result. It roughly follows visible reflections in the region below OBS 10. The agreement of the contour line at 2100 m/s with the reflector at approximately 2.2 km depth is lower than in the results with the full signal content with slightly increased vertical variation and a zone below OBS 7 where the contour line extends to include a 700 m long zone at 2 km to 2.1 km depth. This is consistent between the multi- and monoparameter result.

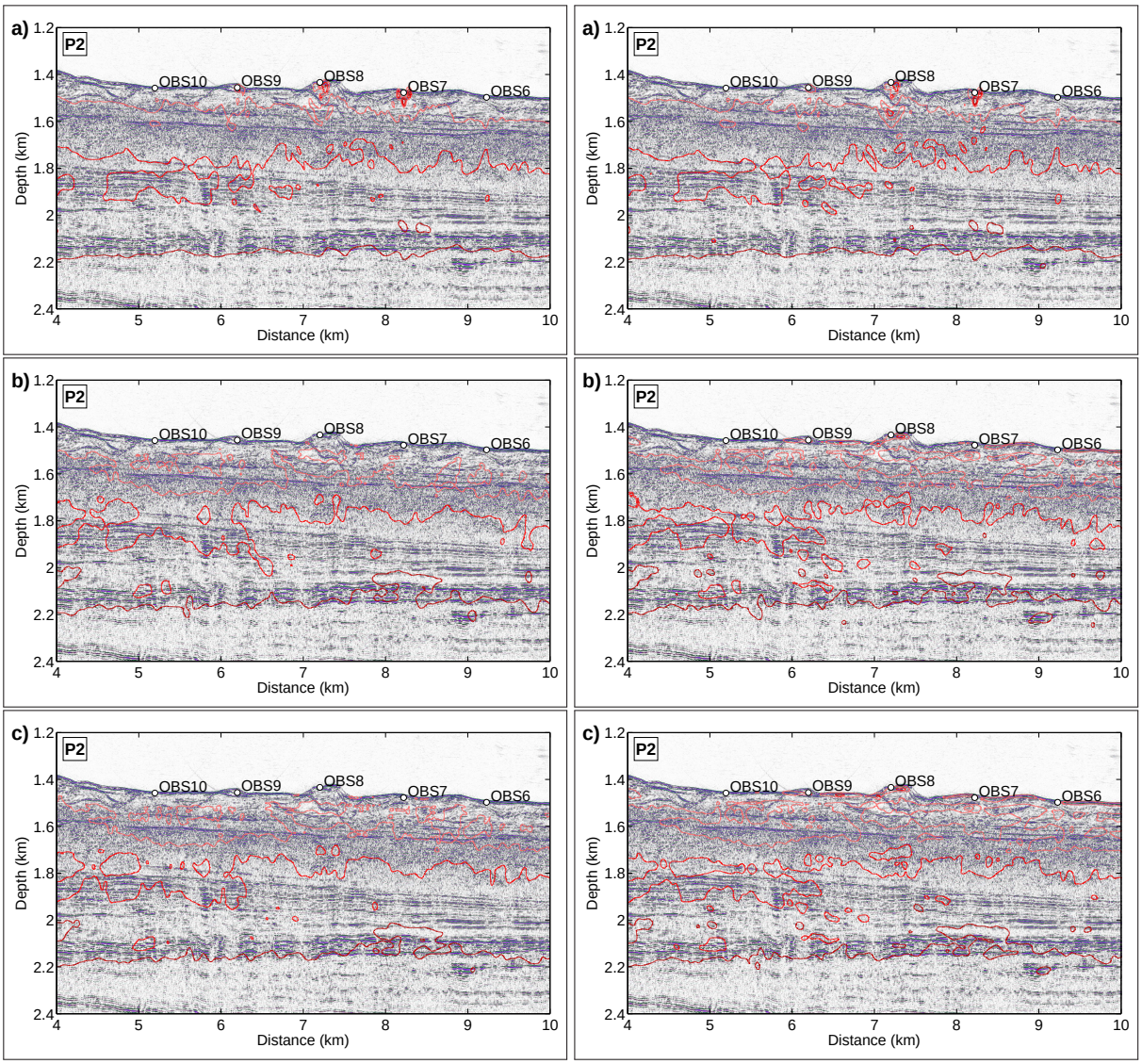

Figure 6.7: Inverted P-wave velocities from multiparameter (left) and monoparameter inversion (right) of profile P2 compared to seismic streamer data. (a) Inversion with full signals, (b) without direct wave and primary reflected signals, (c) same as (b) but with increasing time window.

With an increasing time window approach and reduced signal content (Figure 6.7c) the results are again similar to the results with a constant time window approach. Noticeable differences occur in the 1900 m/s contour line in the region below OBS 10.

In general, the differences between multi- and monoparameter inversion are much less pronounced than at profile P1.

6.3 Estimation of hydrate and gas saturation

Highly resolved parameter models of the elastic or acoustic parameters promise to provide detail on the amount of hydrate and gas that can be found in the subsurface. Saturation values can either be directly calculated from absolute parameter values by empirical relations (e.g. Helgerud et al., 1999; Ecker et al., 2000; Crutchley et al., 2011) or, alternatively, by methods translating reflection coefficients (or AVO) into saturation values (Carcione and Tinivella, 2000) using reflection seismic data.

For direct interpretation of the elastic parameters detailed knowledge on the composition of the subsurface is necessary. Typically, borehole logs provide this kind of information and can also be used to verify or calibrate the near-surface parameters. If no borehole data are available assumptions have to be made from comparable settings.

6.3.1 Theoretical approach

Different approaches are based on either the v_P model only (time-average equation) or on the P-wave modulus $M = \rho v_P^2$ (Wood equation). Hydrate and gas are expected to be hosted by clay- or sand-dominated sediment in a porefilling mode and therefore replacing a part of the fluid fraction f_{fl}. The fluid fraction is used analogously to the porosity in the following. For a data set in the Western Black Sea Winguth et al. (2000) give an interpretation of the different reflection types and for a zone of high-amplitude reflections like it is present at profile P1 they interpret a composition dominated by sand. Nevertheless, I compare results for both materials. For details on the parameters of the sediment constituents see Table 6.3.

The set of time-average equations (Wyllie et al., 1958) is given by

$$\frac{1}{v_P} = \frac{f_{fl}}{v_{P,fl}} + \frac{(1-f_{fl})}{v_{P,mat}}, \tag{6.1}$$

$$\frac{1}{v_P^+} = \frac{f_{fl}(1-S_{hyd})}{v_{P,fl}} + \frac{f_{fl}S_{hyd}}{v_{P,hyd}} + \frac{(1-f_{fl})}{v_{P,mat}}, \tag{6.2}$$

$$\frac{1}{v_P^-} = \frac{f_{fl}(1-S_{gas})}{v_{P,fl}} + \frac{f_{fl}S_{gas}}{v_{P,gas}} + \frac{(1-f_{fl})}{v_{P,mat}}, \tag{6.3}$$

and the set of Wood equations (Wood, 1941) by

$$\frac{1}{M} = \frac{f_{fl}}{M_{fl}} + \frac{(1-f_{fl})}{M_{mat}}, \tag{6.4}$$

$$\frac{1}{M^+} = \frac{f_{fl}(1-S_{hyd})}{M_{fl}} + \frac{f_{fl}S_{hyd}}{M_{hyd}} + \frac{(1-f_{fl})}{M_{mat}}, \tag{6.5}$$

$$\frac{1}{M^-} = \frac{f_{fl}(1-S_{gas})}{M_{fl}} + \frac{f_{fl}S_{gas}}{M_{gas}} + \frac{(1-f_{fl})}{M_{mat}}. \tag{6.6}$$

The saturation is denoted by S and all parameters are labeled by the subscripts $_{hyd}$ for methane hydrate, $_{gas}$ for methane gas, $_{fl}$ for water, and $_{mat}$ for the sediment matrix composed of sand (quartz) and clay.

For the typical range of parameters of the models utilized for acoustic FWI I estimate fluid fractions for a water-saturated sediment body of sand and clay composition. The P-wave velocity at BSR depth is approximately 1880 m/s, the respective density is 2040 kg/m^3, and the P-wave modulus is 7.2 GPa. For these values fluid fractions of 62.4 % for clay and 72 % for sand are estimated from the time-average equation. Application of the Wood equation yields 25.7 % for clay and 29.6 % for sand. All values differ significantly from the expected values of around 50 %.

Zillmer et al. (2005) estimate the porosity at BSR depth to be 57 ± 7 % in their study region with the porosity near the seafloor 78 ± 1 %. For the composition of the subsurface they use 60 % clay, 20 % quartz and 20 % carbonate. Considering the data set analyzed in this work Zander et al. (2017) use porosities ranging from 70 % at the seafloor to 38 % at the base of sediment and a relationship with an exponential decrease with depth. From their approach 39 % porosity at BSR depth can be estimated.

The saturation values calculated with Equations 6.1 to 6.3 for different fluid fractions and P-wave velocities are shown in Figure 6.8a. The respective results for Equations 6.4 to 6.6 are shown in Figure 6.8b for different values of the P-wave modulus. It can be observed that the set of time-average equations yields higher porosity values than the set of Wood equations. It also give a stronger overlap in the estimated saturation values for varying sediment matrix composition. For the time-average equations unrealistically high values of f_{fl} are necessary to explain a significant hydrate saturation for the v_{P} values resulting from FWI. A maximum of approximately $v_{\mathrm{P}} = 2100$ m/s is reached above the BSR (compare Table 6.1) which would result in a hydrate saturation of 30 % for $f_{\mathrm{fl}} = 0.7$ and a pure clay sediment matrix. With $f_{\mathrm{fl}} = 0.5$ a gas saturation of more than 20 % is estimated for $v_{\mathrm{P}} = 1700$ m/s. Zillmer et al. (2005) estimate realistic gas saturation values to be in the range of a few percent. Applying the Wood equations yields hydrate saturations exceeding 40 % for $f_{\mathrm{fl}} = 0.4$ and gas saturations below 6 % for $f_{\mathrm{fl}} = 0.2$.

In general, results show that for higher porosities higher hydrate and lower gas saturations are estimated. For a sediment matrix composed of sand saturation values of gas are higher than with a clay matrix and vice versa for the hydrate saturation. The difference in the estimated fluid fractions has a higher influence on the saturation values than the range of parameters estimated by FWI can indicate. Although providing slightly lower values for the fluid fraction the most realistic estimation of hydrate and gas saturation values can be achieved by assuming a pure sand composition and applying the Wood equation.

Table 6.3: Acoustic parameters of sediment constituents after Carcione and Tinivella (2000), Helgerud et al. (2000), Waite et al. (2009) and references therein. Parameters for clay and quartz are taken from Helgerud et al. (2000), values of v_{P} from Waite et al. (2009).

	M (GPa)	v_{P} (m/s)	ρ (kg/m^3)
Water	2.25	1484	1020
Methane gas	0.11	412	230
Methane hydrate	12.8	3770	920
Quartz	96.6	6040	2650
Clay	30.0	3410	2580

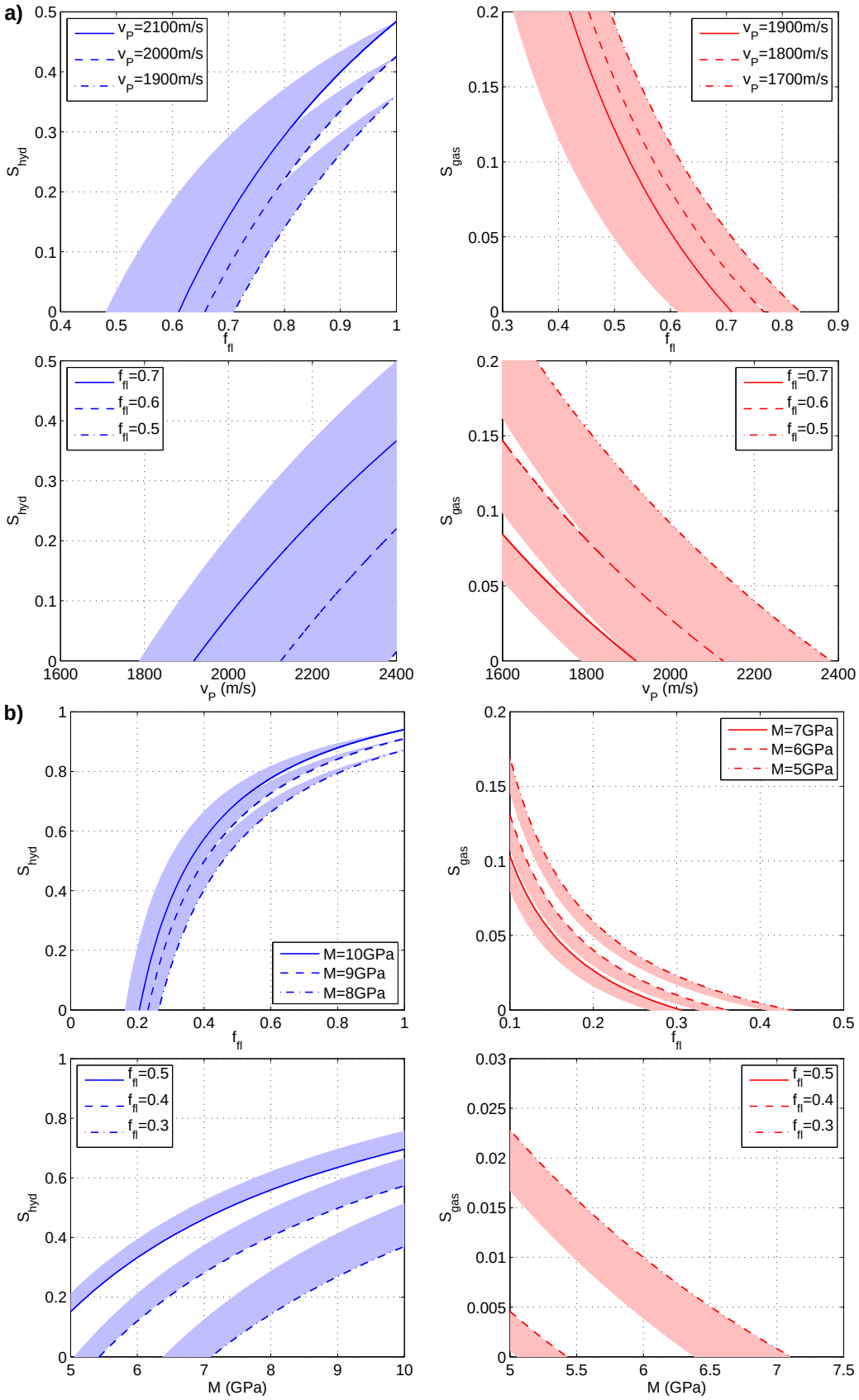

Figure 6.8: Estimated hydrate (blue) and gas saturations (red) for different fluid fractions f_{fl}, (a) P-wave velocities v_{P} and (b) P-wave moduli M. The solid and dashed lines show results for pure sand and the shaded areas mark the differences to a pure clay sediment matrix.

6.3.2 Results for FWI models

To estimate saturation values for the resulting parameter models of the discussed FWI approaches, a model of the P-wave modulus is calculated from the inverted models of density and P-wave velocity. The resulting maximum and minimum M-values above and below the BSR, respectively, are shown in Figure 6.9 for profile P1 and Figure 6.10 for profile P2. Values of the P-wave modulus near the BSR range from 5.5 GPa to 9.1 GPa. Differences between the multiparameter and monoparameter approaches are small (approximately 0.2 GPa) for results using the full signal content for both profiles and for results using the reduced signal content for profile P2. At profile P1 the differences when inverting the reduced signal content reach 0.8 GPa.

For hydrate and gas quantification Equation 6.4 is applied to the starting parameter models of FWI to estimate a model of the fluid fraction. Resulting parameter models from FWI are then interpreted with Equations 6.5 and 6.6 for the estimation of saturation values. Positive parameter changes are converted to hydrate saturation values and negative changes to gas saturation. At profile P1 (Figure 6.11) hydrate accumulation can be interpreted above the BSR. A thin layer with hydrate saturation partly exceeding 20 % can be recognized best in the results from monoparameter inversion with reduced signal content. Below this zone gas accumulation of up to 2 % is calculated. Additionally, the strong parameter changes near the seafloor which result from incorrect density information are converted into high saturation values in the results from the inversion of the reduced signal content. The strong artifacts near the OBS stations from the approach using the full signal content are visible in the resulting saturation models as well.

Saturation estimation at profile P2 yields the models shown in Figure 6.12. At profile P2 hydrate occurrence can be interpreted from the resulting parameter models of FWI in larger regions than on profile P1. No distinct layer near the BSR can be observed. Closely below the BSR gas accumulation can only be estimated in a few zones between 3 km and 6 km profile distance. These observations are consistent between all approaches. Potential hydrate occurrence is estimated with increasing saturation towards the BSR for the approaches where the direct wave and primary reflections are not considered in the inversion. From inversion with all events the potential hydrate saturation is more uniform within the region above the BSR.

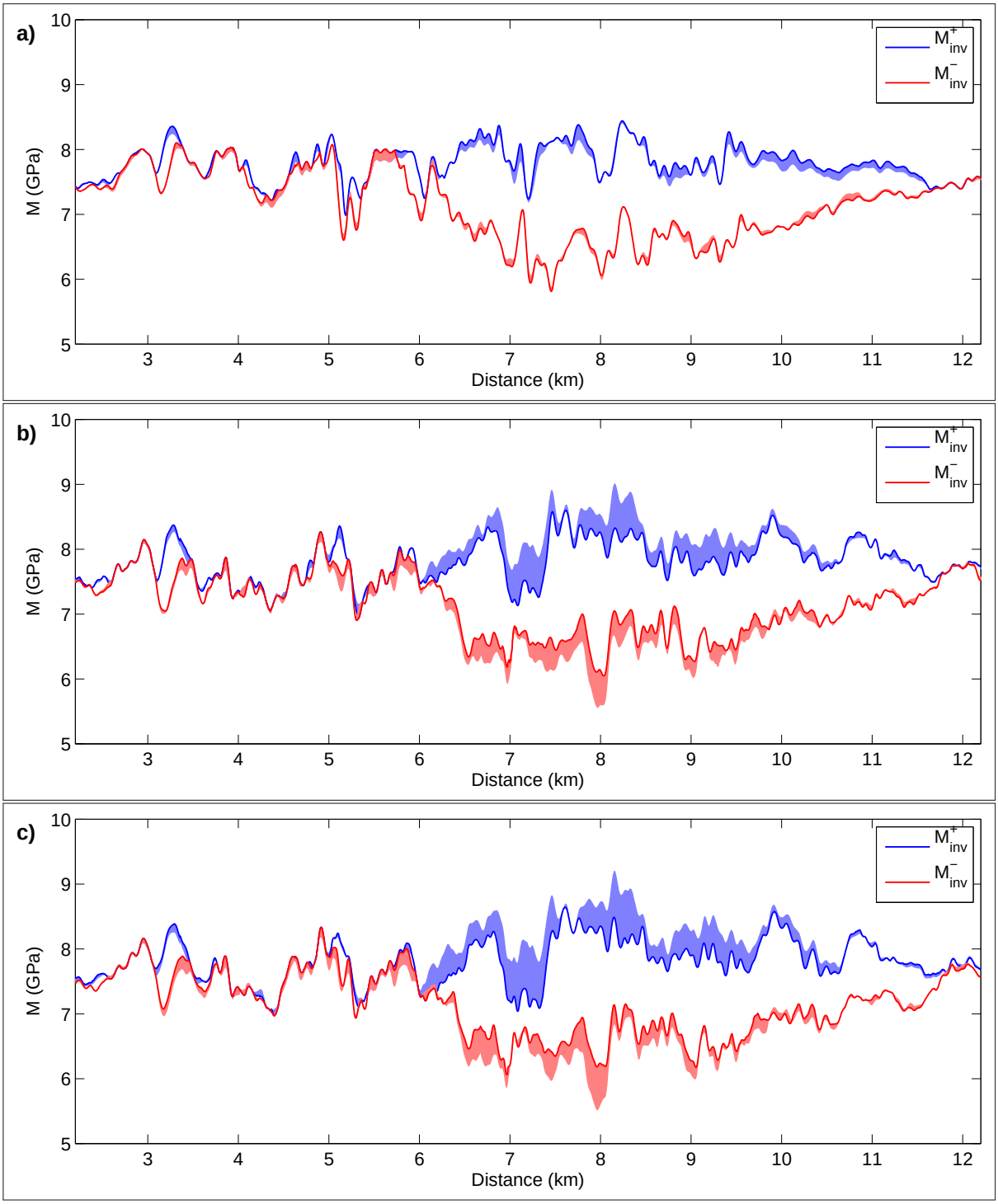

Figure 6.9: Comparison of BSR P-wave modulus distribution for inversion results for profile P1. (a) Inversion with all events, (b) without direct wave and primary reflections, (c) same as (b) but with increasing time window. The blue and red lines show values for simultaneous inversion of v_P and ρ, the shaded areas mark the differences to the result from monoparameter v_P inversion.

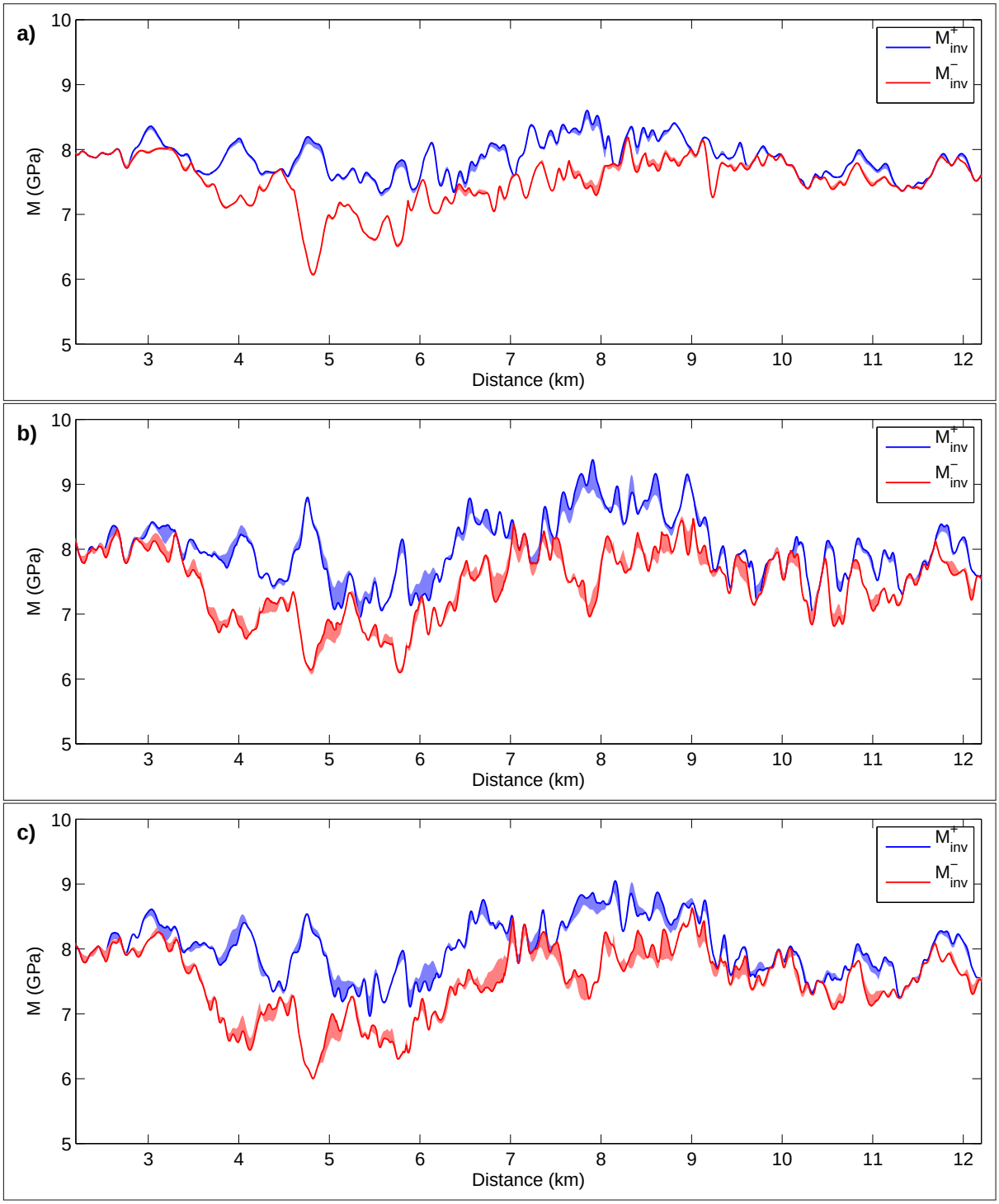

Figure 6.10: Comparison of BSR P-wave modulus distribution for inversion results for profile P2. (a) Inversion with all events, (b) without direct wave and primary reflections, (c) same as (b) but with increasing time window. The blue and red lines show values for simultaneous inversion of v_P and ρ, the shaded areas mark the differences to the result from monoparameter v_P inversion.

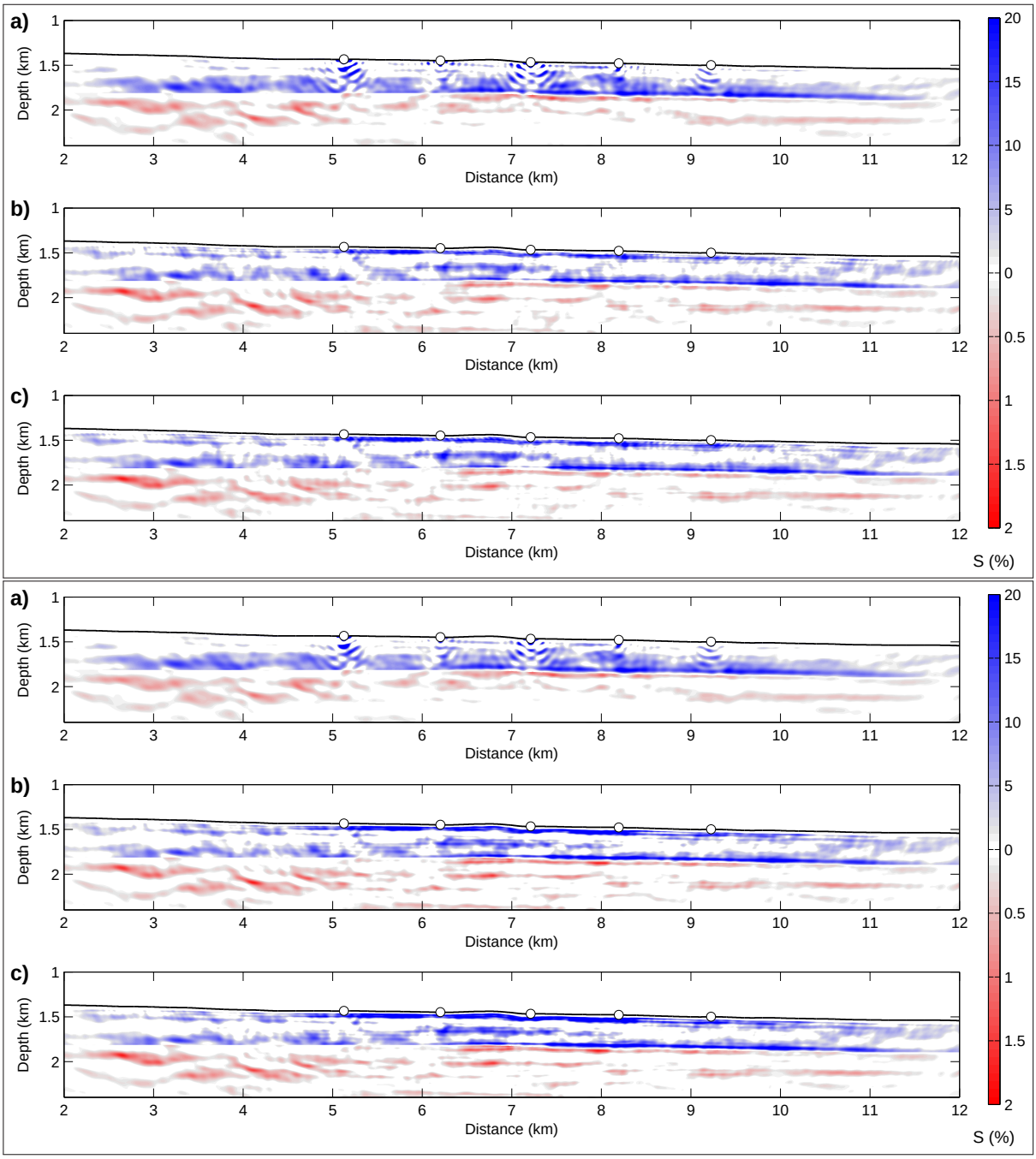

Figure 6.11: Estimated hydrate (blue) and gas (red) saturation for profile P1 for (top) multiparameter and (bottom) monoparameter inversion. (a) Inversion with full signals, (b) without direct wave and primary reflected signals, (c) same as (b) but with increasing time window.

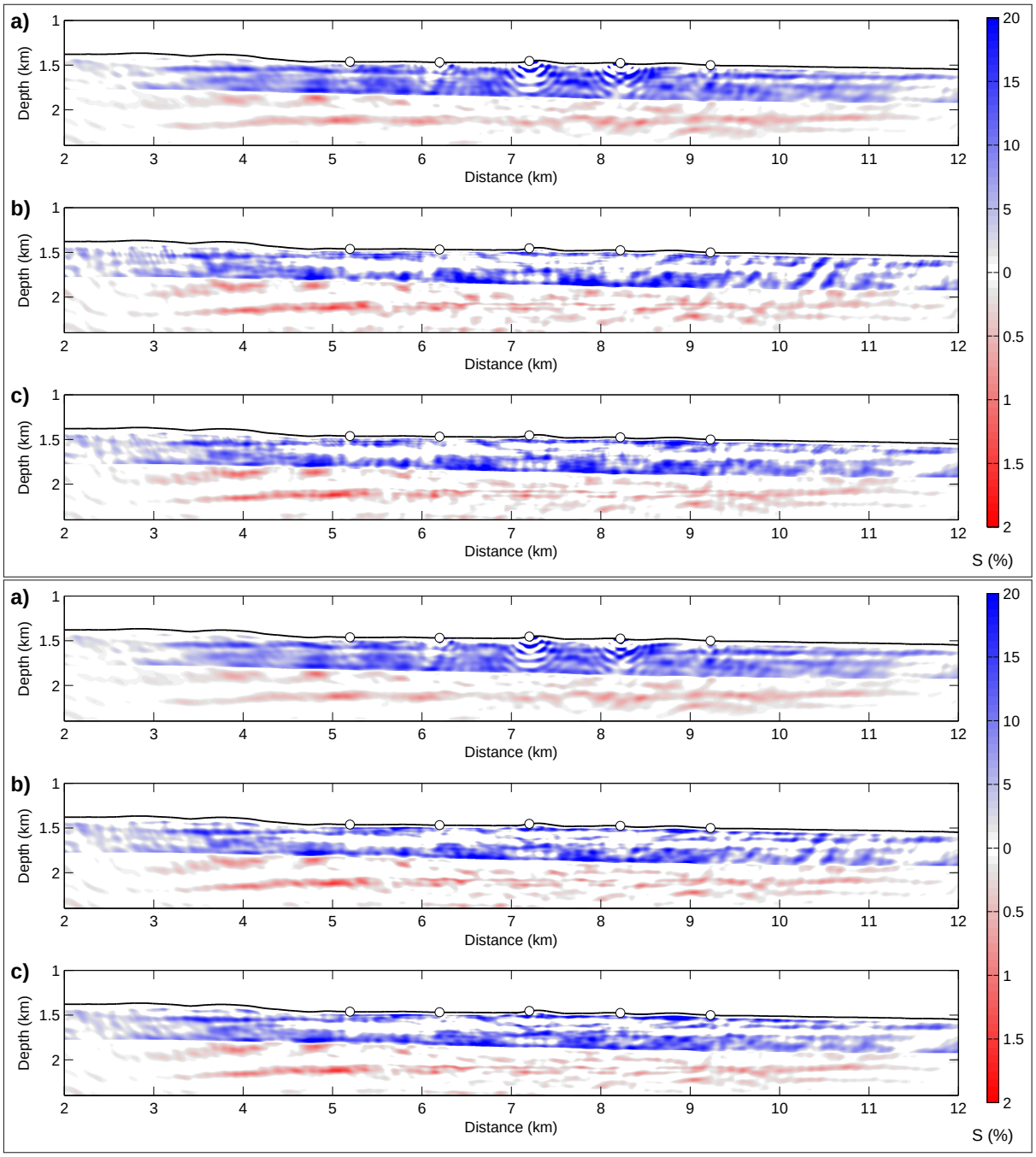

Figure 6.12: Estimated hydrate (blue) and gas (red) saturation for profile P2 for (top) multiparameter and (bottom) monoparameter inversion. (a) Inversion with full signals, (b) without direct wave and primary reflected signals, (c) same as (b) but with increasing time window.

6.4 Summary

In this chapter an evaluation of the results from acoustic FWI is shown verifying the plausibility of the models discussed in Chapter 5. From the inverted v_P models potential hydrate and gas occurrence is indicated by zones of increased and reduced P-wave velocities compared to the starting parameter models. At both profiles, P1 and P2, regions are present where such a parameter contrast is constructed at BSR depth by FWI. The zones delineated by the velocity at BSR depth are of varying horizontal continuity. At profile P1 the interpreted hydrate and gas zone is consistent for all discussed approaches and continues from 6 km to approximately 12 km profile distance. The extent and location of the respective zones at profile P2 vary with the applied approach and zones are less continuous.

A comparison of the v_P models resulting from FWI to the corresponding seismic streamer sections shows that zones delineated by lines of equal velocity are in good agreement with reflectivity structures. In the shallow model part reflectivity structures are matched when inverting the reduced signal content and by applying monoparameter inversion the horizontal continuity of zones is increased. The artifacts near the OBS positions which arise when using the full signal content prevent the reconstruction of the shallow structures indicated by the streamer data. At profile P1 the extent of the observed v_P contrast at BSR depth is consistent with a zone of high-reflectivity amplitudes which is outlined by the velocity contour. Again, the horizontal continuity is highest when using the reduced signal content and applying monoparameter inversion. At profile P2 the match of the respective contour line with structures at BSR depth is less accurate. For both profiles the deepest shown contour line agrees well with a change in reflectivity amplitudes. Here, the fit is best when inverting the full signal content.

To estimate hydrate and gas saturation a simple approach using empirical relations is employed. Due to the lack of information on the subsurface composition a mixed clay and sand composition is assumed. Evaluation of the resulting estimated fluid fractions of the sediment show lower values than in publications studying the same region. The calculation of saturation values of hydrate and gas from the inverted parameter models shows that at profile P1 the inverted parameter contrast at BSR depth can be converted to meaningful saturation values consistently for all approaches. The conversion of parameter changes to saturation values for profile P2 yields no meaningful gas saturations below the BSR for any extended zone. Hydrate saturation can be interpreted for all results although no distinctive zone of increased saturation can be observed above the BSR.

7 Summary and conclusions

In this work I investigate the potential of full-waveform inversion (FWI) applied to an ocean-bottom seismic (OBS) data set with the purpose of studying gas-hydrate deposits. Previously, studies using streamer data from different gas-hydrate provinces have shown successful applications of FWI in the context of hydrate exploration. The use of OBS data is advantageous as long offsets are available and through the application of the reciprocity principle computation times can be reduced significantly compared to conventional streamer data. Inverted models of the elastic subsurface parameters provide information on the extent of potential hydrate and gas deposits and serve as an input for saturation estimations.

The FWI methodology is widely used but still a lot of work has to be invested in the configuration of the FWI workflow and in the evaluation of the outcome from inversion for each new application. Synthetic tests are executed to check the feasibility of FWI for an OBS geometry and a subseafloor parameter distribution representative for hydrate and gas occurrence (Chapter 3). Synthetic studies with a similar geometry and general conditions as in the field measurement show a successful recovery of the P-wave velocity model, providing interpretable parameter models in terms of the recovered maximum and minimum velocities above and below the BSR, respectively. The results of the synthetic tests indicate that an acoustic approximation is valid when the S-wave velocity model is as simple as in the discussed tests. Reconstruction of a v_S model is not possible due to low amplitudes of S-waves compared to P-waves. Also, the reconstruction of the density distribution fails within the synthetic inversion tests. Typically, density inversion is applied to compensate for physical effects not accounted for and therefore in acoustic field data applications v_P and ρ are inverted for simultaneously. In the case of a parameter distribution typical for hydrate and gas occurrence where mainly the P-wave velocity is influenced, the application of simultaneous inversion reduces the recovered parameter contrast in v_P due to cross-talk to the ρ model.

OBS data acquired in the area of the Danube deep-sea fan in the Western Black Sea is utilized to study the capacity of FWI applied to field data for gas-hydrate exploration. Preparation for FWI includes the selection of a suitable subset of the field data, preprocessing of the chosen data, and the creation of starting models and tapers (Chapter 4). Hydrophone data of two parallel profiles is used for field data inversion with an acoustic approach and a constant level of attenuation in the subseafloor sediments. Starting models are created from available results of traveltime tomography yielding smooth models of the subsurface P-wave velocity distribution. Bathymetry data are available with a spatial resolution of approximately 10 m to create tapers preventing updates in the water column. Analysis of the geometry information of the measurement shows that OBS stations at the seafloor were located up to 100 m off the profile line where shots were emitted. This deviation results in differences in the seafloor depth of up to 15 m between the actual OBS stations and the shot lines. The seafloor depth at the mean OBS profiles is used for the creation of starting models and tapers to compensate these differences. Nevertheless, in the results from field data inversion artifacts appear near the OBS stations where deviations are present.

To adjust the field data to the modeling approach 3D-to-2D transformation is applied. This results in a relative amplitude increase of low frequencies requiring the application of high-pass filtering to suppress low-frequency noise. Furthermore, a strong ringing can be observed following the direct wave arrival which masks the primary reflections. Therefore, the application of time windowing to exclude the direct wave and primary reflections and only use the multiply reflected events for inversion is considered.

Results for field data inversion of both profiles using different approaches indicate the influence of time windowing on the inverted parameter distributions (Chapter 5). When the direct wave and primary reflections are included artifacts near the OBS stations are prominent and prevent the resolution of structures in the shallow subseafloor region. The application of time windowing significantly reduces these artifacts which can be attributed to the more complex wave paths. Because of the longer travel distances through the model, errors arising from positioning can be distributed throughout the model and are not projected to the vicinity of the OBS stations. The parameter distribution in the deeper model part is more similar for both approaches. Indications for a typical BSR parameter distribution can be found at profile P1 for all time windowing approaches. At profile P2 no comparable observation can be made. For an inversion for v_P only, a higher parameter contrast in the inverted v_P model is found at profile P1 when using input data reduced to the multiple reflections and the refractions. Results of multiparameter and monoparameter inversion are more similar for all time windowing approaches at profile P2.

From the resulting v_P models regions of potential hydrate and gas occurrence are estimated by a delineation of zones where the velocity at BSR depth is exceeded above and where it falls below this velocity underneath. The horizontal continuity of the estimated zones hints at a horizontal extent of at least 5.6 km at profile P1, while at profile P2 no consistent delineation can be achieved between the different approaches. These observations in the inverted v_P distribution at BSR depth hint at an extended zone of potential hydrate and gas occurrence at profile P1. In contrast, no indications for extended gas occurrence can be observed at profile P2. Theses differences in inverted P-wave velocity distribution can be confirmed by a comparison with migrated seismic streamer data. The zone of reduced v_P is aligned well with a layer of high amplitude reflections, while no such behavior is visible at profile P2. Apart from the region of the BSR a good agreement between lines of equal velocity and zones of distinct reflectivity patterns can be observed. A better correspondence of the horizontal extent of structures in the shallow subseafloor region is achieved by the inversion of v_P only.

To estimate hydrate and gas saturation from the inverted parameter models empirical relations are utilized. It is assumed that the starting v_P model and the derived density model represent water saturated sediment. To describe the relation of the parameters of water saturated sediment with its constituents, average equations for the P-wave velocity or the P-wave modulus are utilized. The inverted parameter models are then supposed to show the effect of hydrate or gas (above or below the BSR, respectively) on the fluid component and are used to predict the saturation of the pore fluid. The estimation yields realistic saturation values compared to other studies in this region (e.g., Zillmer et al., 2005). Resulting parameter models of FWI imply hydrate saturation above the BSR for both profiles with a more distinctive zone visible at profile P1 which is of smaller vertical extent than the potential region at profile P2. Furthermore, extended gas saturation below the BSR can only be deduced for profile P1, whereas only small zones can be observed at profile P2.

In conclusion, the application of acoustic FWI provides detailed models of the subseafloor v_P distribution that can be interpreted in the context of hydrate and gas occurrence. The typical parameter distribution at BSR depth can be reconstructed consistently in synthetic examples and in the field data application. It is shown that FWI is a reliable tool to estimate extended zones of hydrate and gas occurrence which are consistent with the interpretation of migrated seismic streamer data. Therefore, an evaluation of the location of potential reservoirs can be achieved successfully by the inversion of OBS data and can be the groundwork to determine locations for drilling to achieve direct sampling. For the estimation of hydrate and gas saturation more information, e.g. from borehole data or an extensive geological interpretation, need to be considered. Nevertheless, based on suitable assumptions saturation values can be estimated directly from the FWI models.

7.1 Outlook

In this work the consistency of structures between results using different approaches is utilized to evaluate the reliability of the inverted parameter models. The workflow controlling the inversion process can be configured in many different ways depending on the results desired and on previous experiences. A more general approach to classify each option would be a useful tool to evaluate the range of models explaining the input data and to provide a framework for error estimation.

The required resolution and type of parameter model can vary significantly for different FWI applications. In connection with gas hydrate exploration the v_P model is the most important parameter for the assessment of hydrate and gas occurrence. Further information on the pore-scale hydrate distribution can be provided by the v_S and attenuation models. In marine applications the inversion of a v_S model is still not common and strategies need to be developed to recover reliable models also from OBS data. For this purpose the experiment design needs to be optimized as a much closer sampling of the subsurface is required for the reconstruction of v_S. Also, a more precise positioning of the stations would benefit the inversion which can be achieved by the use of remotely operated vehicles.

To show the transferability of the results acquired in this work further applications of FWI to OBS data in other gas hydrate provinces are desirable.

A Geometry details for profiles P1 and P2

Table A.1: Details on geometry of profiles P1 and P2.

	P1	P2
Number of shots	1301	1691
Mean shot distance	10.2 m	8.18 m
Minimum shot distance	6.27 m	5.24 m
Maximum shot distance	13.1 m (41.9 m)	11.26 m
Shot depth	2 m	2 m

Table A.2: Coordinates of profiles P1 and P2.

	°N	°E	Depth in m
First shot P1	43.4257	30.4671	1546
Last shot P1	43.5218	30.3700	1348
First shot P2	43.5151	30.3596	1352
Last shot P2	43.4158	30.4625	1622

Table A.3: Coordinates of OBS stations.

	°N	°E	Depth in m
OBS 1	43.4862	30.4041	1430
OBS 2	43.4784	30.4120	1451
OBS 3	43.4709	30.4192	1467
OBS 4	43.4640	30.4267	1474
OBS 5	43.4565	30.4343	1500
OBS 6	43.4511	30.4246	1501
OBS 7	43.4584	30.4171	1476
OBS 8	43.4657	30.4096	1458
OBS 9	43.4729	30.4021	1469
OBS 10	43.4802	30.3948	1461

Table A.4: Mean shot and OBS y-coordinates for profiles P1 and P2 in the rotated coordinate system.

	P1	P2
Mean y-coordinate shots	6946 m	5975 m
Mean y-coordinate OBS	6864 m	5873 m

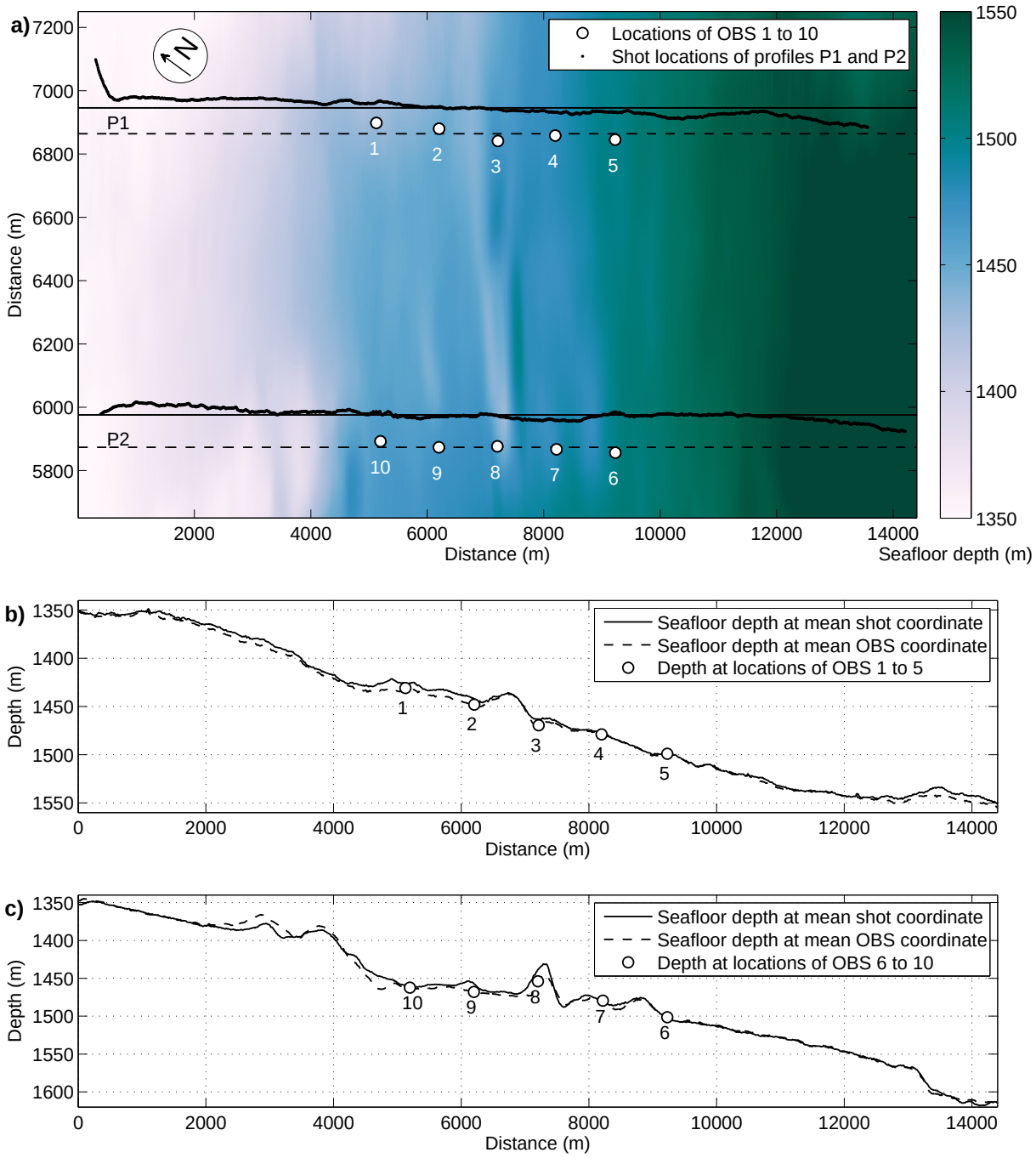

Figure A.1: Detail of field geometry for profiles P1 and P2 with corresponding seafloor depths at OBS and shot locations. (a) Bathymetry with the locations of OBS 1 to 10 and shot locations of P1 and P2. The deviation of the OBS by up to 100 m to the southwest of the profiles is visible. The seafloor depth at the shot locations and OBS stations are shown for profile P1 and P2 in (b) and (c), respectively.

B Technical details on modeling and inversion

B.1 Synthetic example

Table B.1: Technical details on modeling and inversion for synthetic example.

Number of grid points ($NX \times NY$)	2400×600
Spatial discretization Δh	5 m
Number of time steps NT	5000
Temporal discretization Δt	1 ms
Spatial FD-Order	4
Temporal FD-Order	2
PML size	150 m
Number of cores	80
Domain decomposition	20×4
Time per iteration	ca. 8.6 min

Table B.2: Step length estimation for synthetic example.

Stop criterion	0.01
Scale factor	5
Maximum tests	4
Shots used	1, 3, 5

Table B.3: Limitation on model parameters for synthetic example.

v_P	1400 m/s - 2500 m/s
v_S	1 m/s - 1500 m/s
ρ	1000 kg/m^3 - 2000 kg/m^3

B.2 Field data inversion

Table B.4: Technical details on modeling and inversion for field data application.

Number of grid points ($NX \times NY$)	7200×1500
Spatial discretization Δh	2 m
Number of time steps NT	15000
Temporal discretization Δt	0.4 ms
Spatial FD-Order	4
Temporal FD-Order	2
PML size	60 m
Number of cores	480
Domain decomposition	40×12
Time per iteration	ca. 10.86 min

Table B.5: Step length estimation for field data inversion.

Stop criterion	0.01
Scale factor	5
Maximum tests	5
Shots used	1 - 4

Table B.6: Limitation on model parameters for field data inversion.

v_P	1484 m/s - 2500 m/s
ρ	1020 kg/m^3 - 2300 kg/m^3

Table B.7: Q estimation for field data inversion.

Quality factor Q	100
Number of relaxation mechanisms L	2
Relaxation frequencies $f_L = 2\pi/\tau_{\sigma l}$	4.4169 Hz
	34.6818 Hz
τ	0.0159

C Reduced high-pass frequency

Here, I show results for profile P1 using the same setup and time windowing approaches as discussed in Section 5.2 with the constant high-pass frequency reduced to 3 Hz instead of 5 Hz. In general, it is preferred to include as low frequencies as possible into FWI. On one hand, they enable a correction of the long wavelength velocity trend of the model. On the other hand, the signal-to-noise ratio decreases with lower frequencies and therefore strongly influenced signal content is usually excluded from inversion. With 3 Hz high-pass frequency, the effect of low-frequency noise is notable in the seismograms considering the multiply reflected arrivals (Figure C.1).

The resulting parameter models (Figure C.2 and C.3) are similar to the results obtained with 5 Hz high-pass frequency. The source time functions (Figure C.4) are consistent among all stations for each approach. The misfit reduction is less than in the results with 5 Hz high-pass frequency due to the lower signal-to-noise ratio. Low-frequency noise is also visible in the data residuals (Figure C.5).

A comparison of depth profiles (Figure C.6) and the resolved maximum and minimum v_P-values above and below BSR depth (Figure C.7), respectively, show that visible differences of up to 50 m/s occur between the two different high-pass frequencies. The v_P-contrast at BSR depth is reduced in the approach using the full signal content. With reduced signal content the maximum and minimum values are both slightly increased.

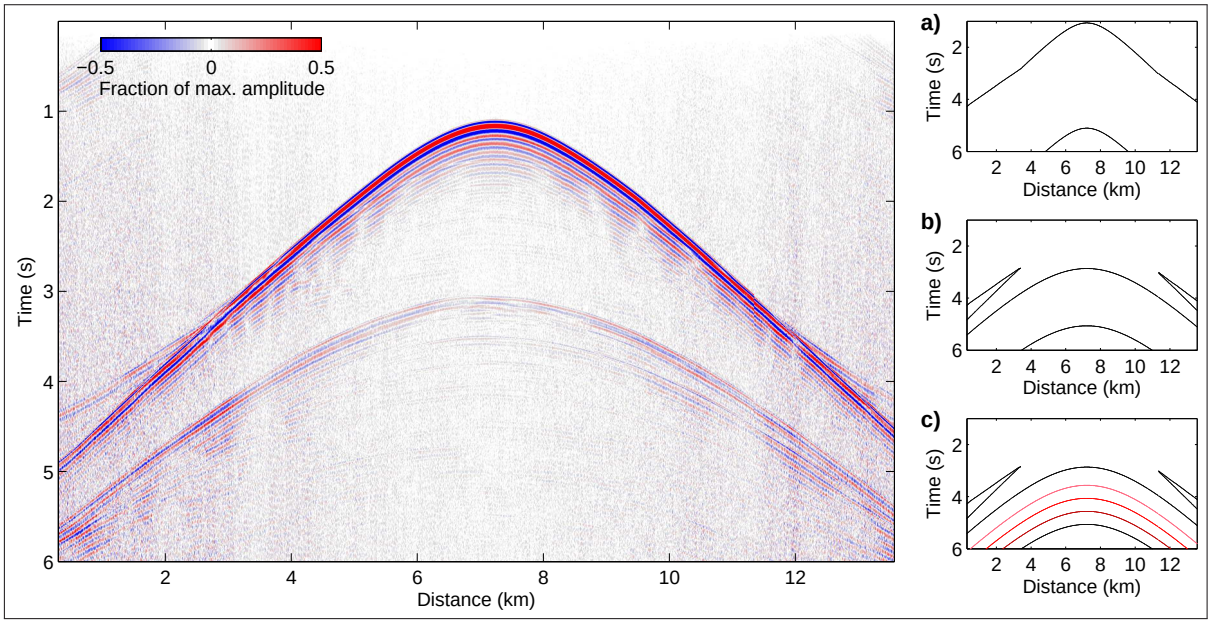

Figure C.1: Examplary seismogram (left) and time windows (right) applied in the inversionof data with reduced high-pass frequency from profile P1. (a) All events, (b) without the direct wave and primary reflections, (c) same as (b) but with increasing time window.

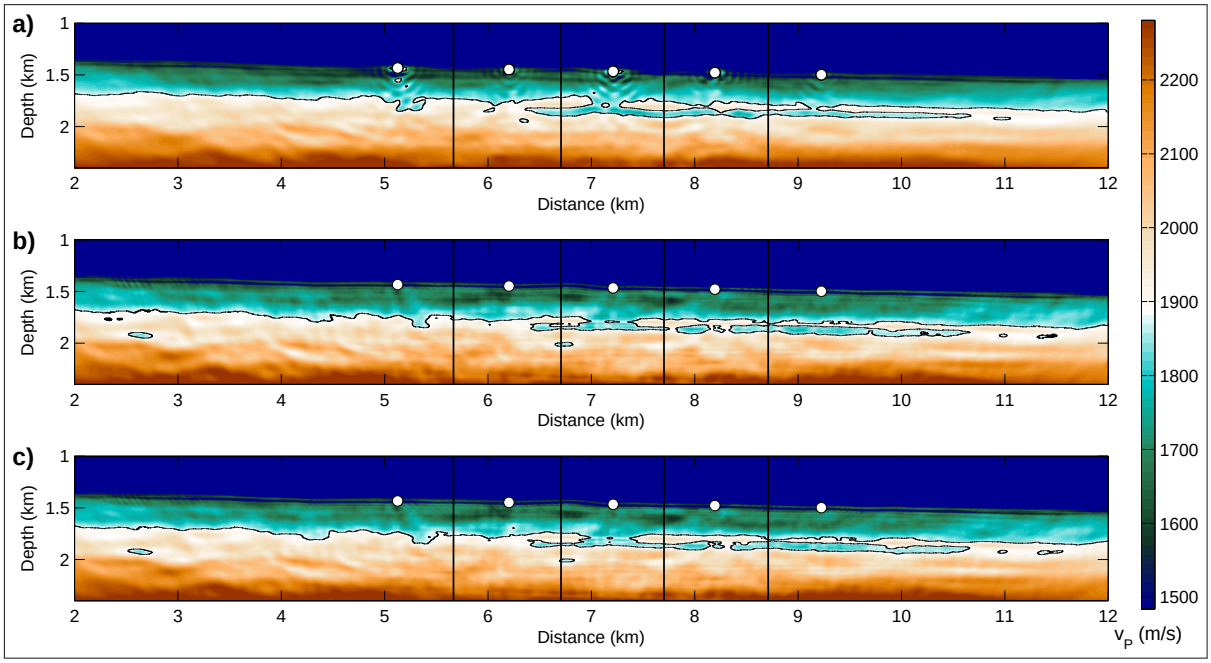

Figure C.2: Resulting v_P models from inversion of data from profile P1 with reduced high-pass frequency. (a) Inversion with all events, (b) without the direct wave and primary reflections, (c) same as (b) but with increasing time window. Vertical black lines mark the locations of the depth profiles shown in Figure C.6.

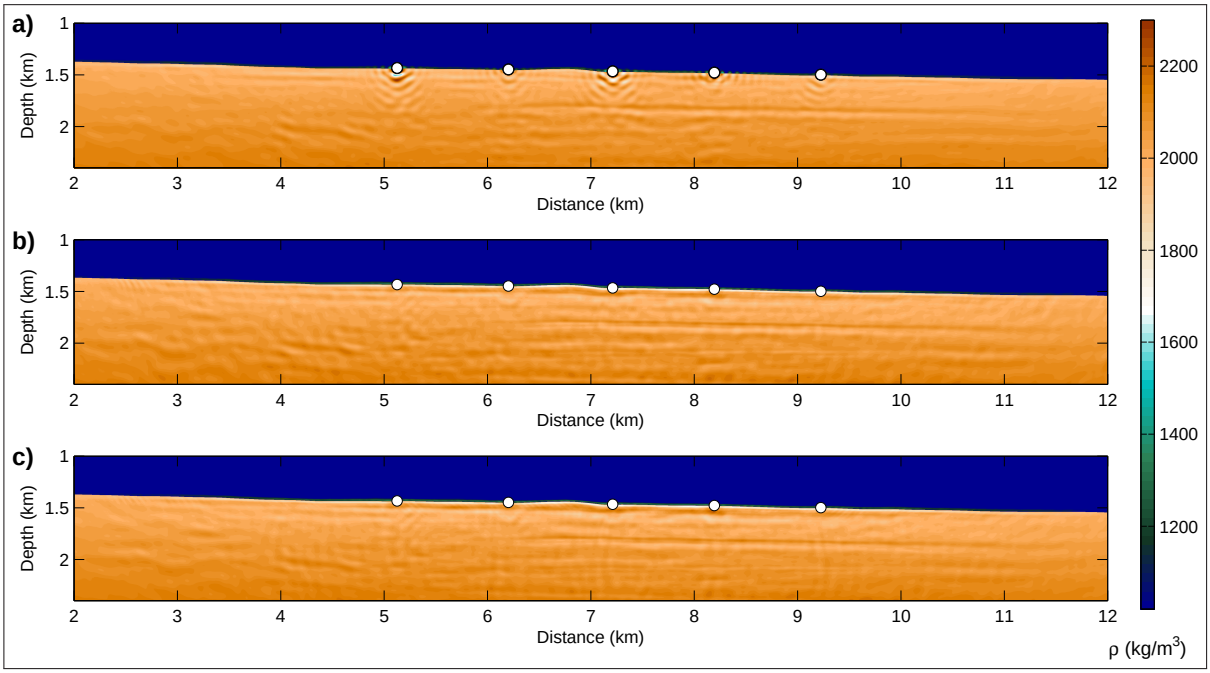

Figure C.3: Resulting ρ models from inversion of data from profile P1 with reduced high-pass frequency. (a) Inversion with all events, (b) without the direct wave and primary reflections, (c) same as (b) but with increasing time window.

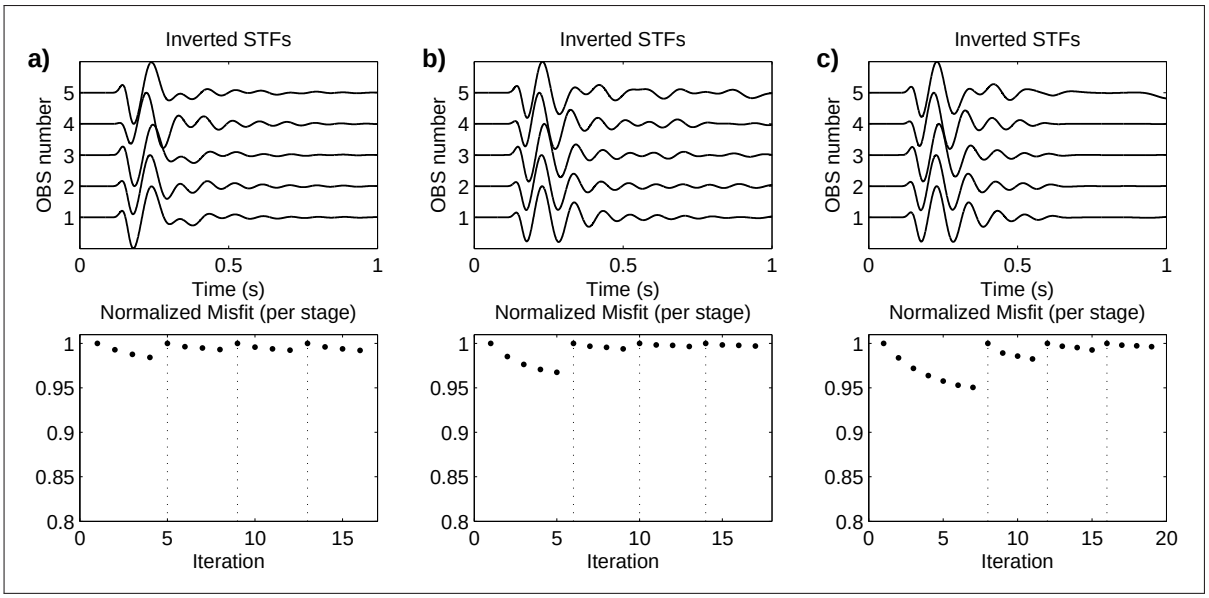

Figure C.4: Source time functions (top) and misfit evolution (bottom) for profile P1 with reduced high-pass frequency. (a) Inversion with all events, (b) without the direct wave and primary reflections, (c) same as (b) but with increasing time window.

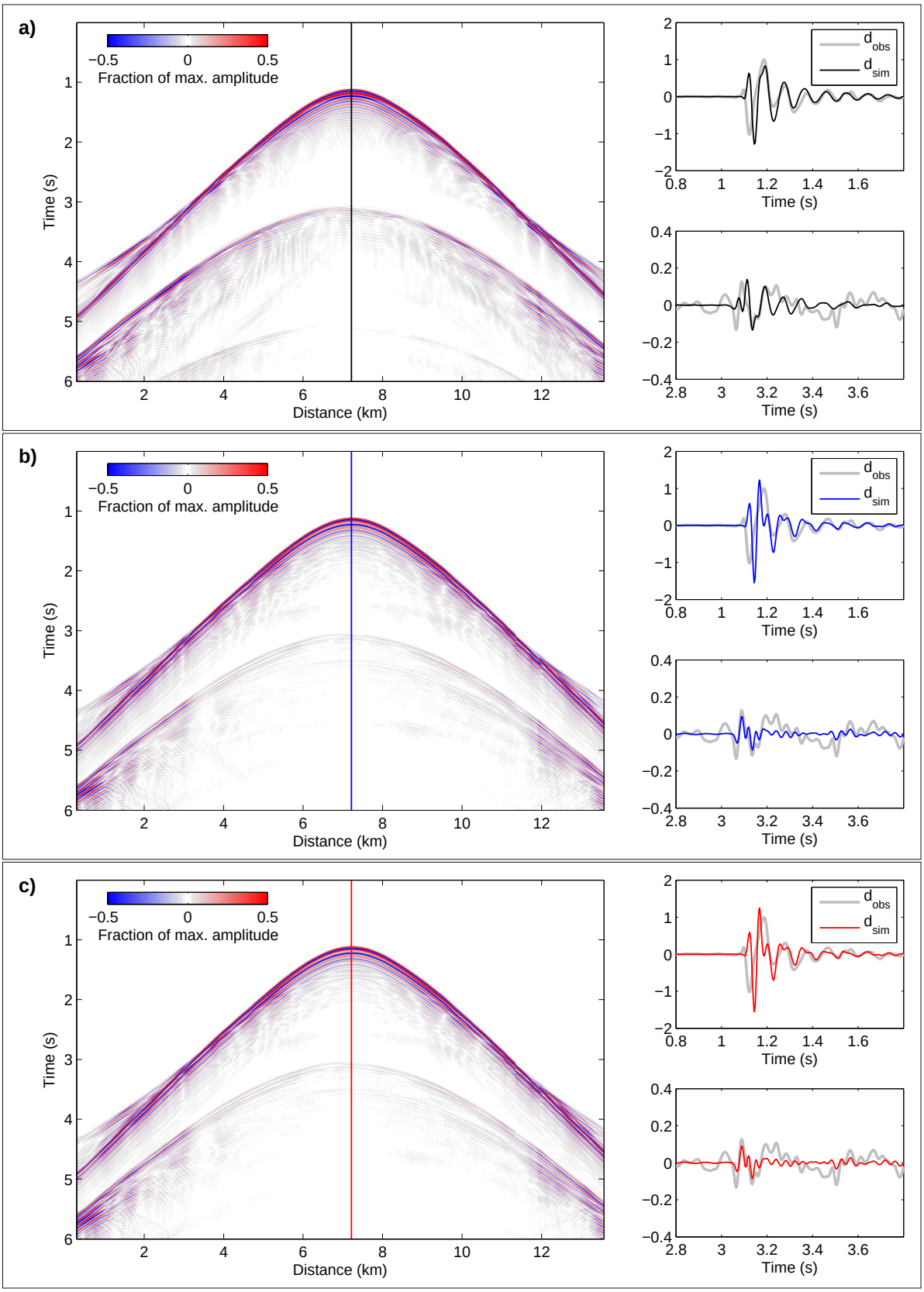

Figure C.5: Final seismograms of OBS 3 for inversion of data from profile P1 with reduced high-pass frequency. (a) Inversion with all events, (b) without the direct wave and primary reflections, (c) same as (b) but with increasing time window. The vertical line in each seismogram image marks the location of the trace shown on the right.

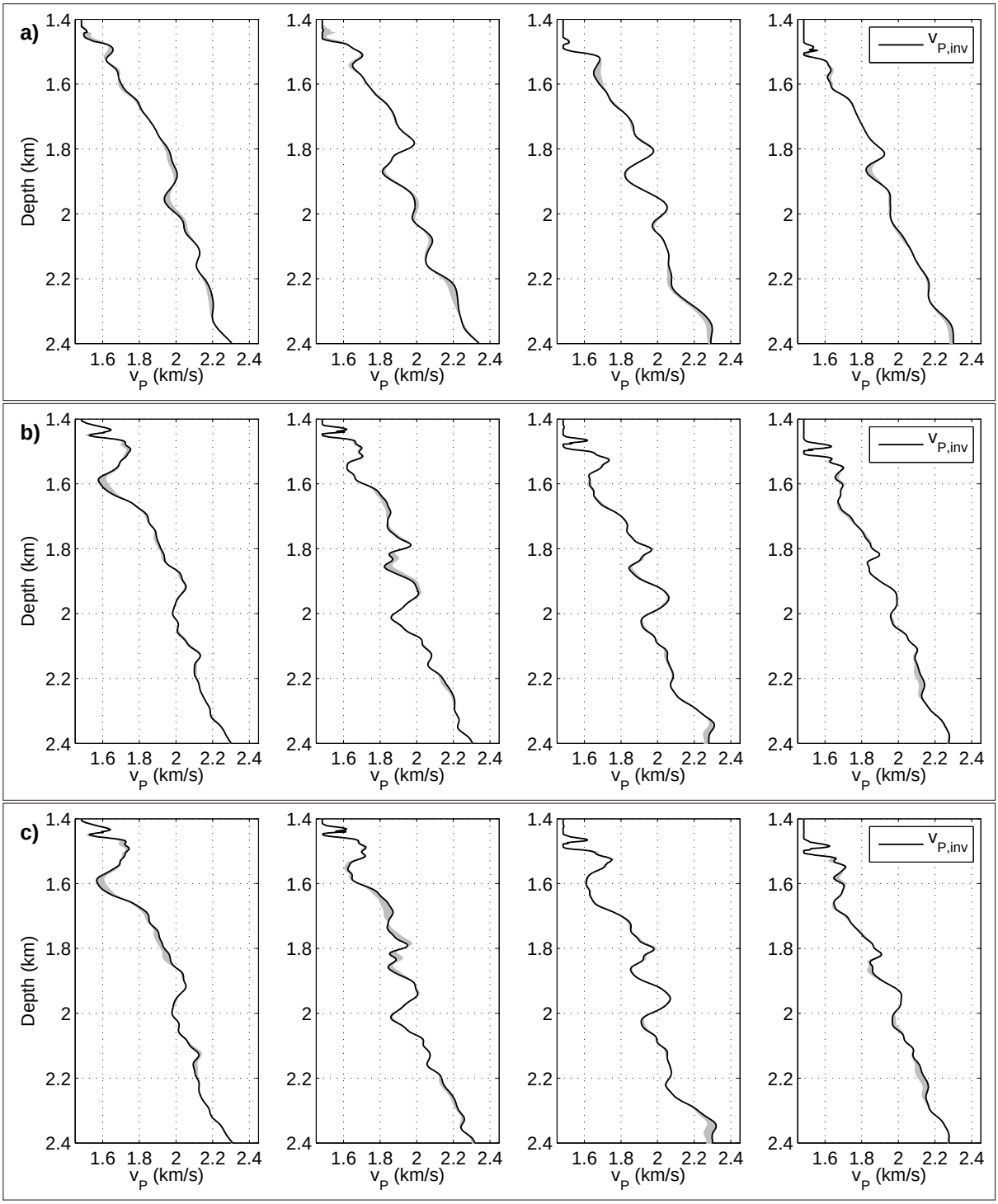

Figure C.6: Comparison of v_P depth profiles for inversion results of profile P1 with reduced high-pass frequency. (a) Inversion with all events, (b) without the direct wave and primary reflections, (c) same as (b) but with increasing time window. Black lines show the resulting v_P depth profiles with 5 Hz high-pass frequency, the shaded areas mark the differences to the result with 3 Hz high-pass frequency.

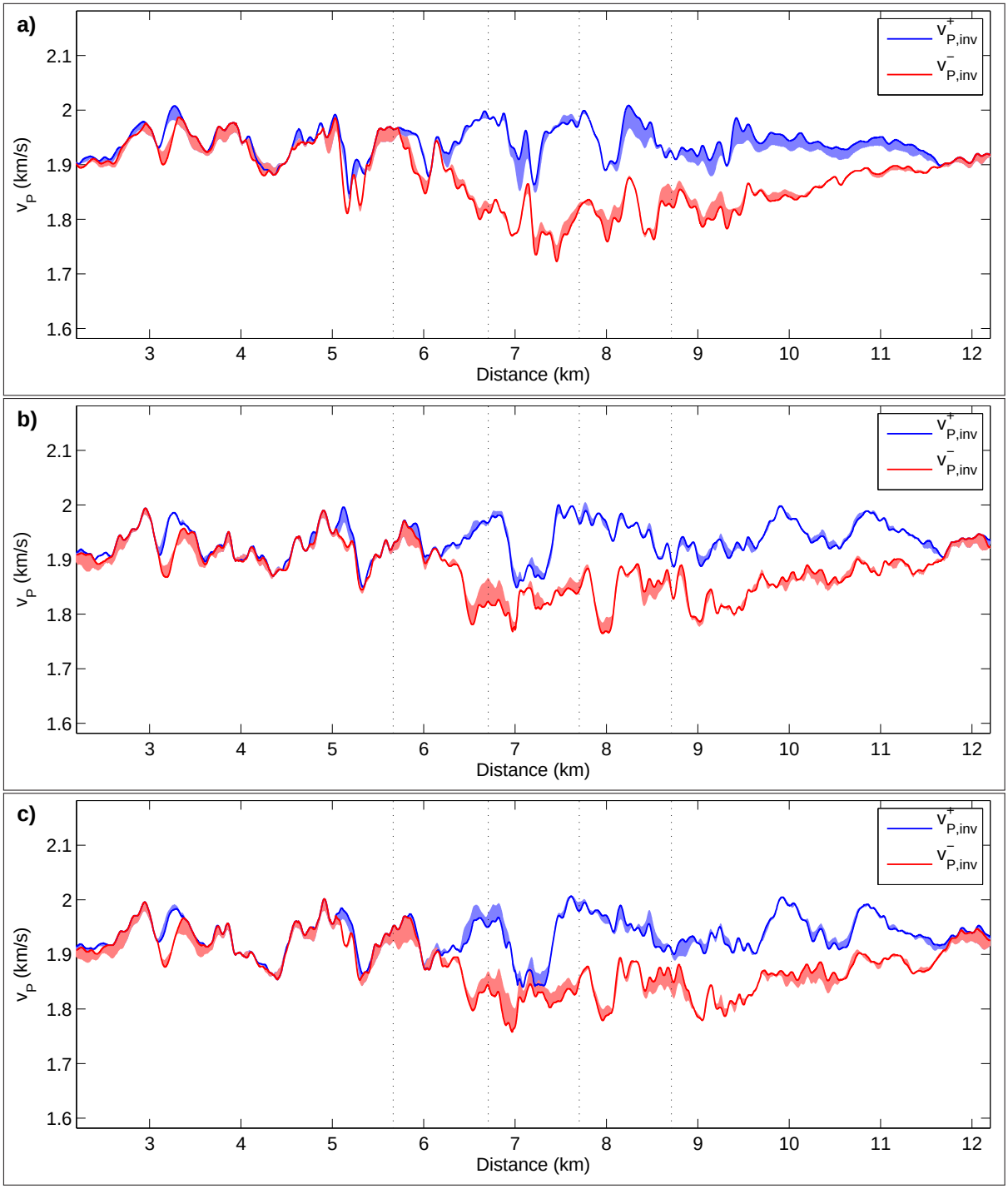

Figure C.7: Comparison of BSR v_P distribution for inversion results for profile P1 with reduced high-pass frequency. (a) Inversion with all events, (b) without the direct wave and primary reflections, (c) same as (b) but with increasing time window. The blue and red lines show values for inversion with 5 Hz high-pass frequency, the shaded areas mark the differences to the result with 3 Hz high-pass frequency. Vertical dotted lines mark the locations of the depth profiles shown in Figure C.6.

Bibliography

Aki, K. and Richards, P. G. (2002). *Quantitative seismology*.

Bialas, J. and Flueh, E. R. (1999). Ocean Bottom Seismometers. *Sea Technology*, 40(4):41–46.

Bialas, J., Klaucke, I., and Haeckel, M. (2014). FS MARIA S. MERIAN Fahrtbericht/Cruise Report MSM34/1 & 2-SUGAR Site; Varna–Varna, 06.12.13–16.01.14.

Blanch, J. O., Robertsson, J. O., and Symes, W. W. (1995). Modeling of a constant Q: Methodology and algorithm for an efficient and optimally inexpensive viscoelastic technique. *Geophysics*, 60(1):176–184.

Bohlen, T. (2002). Parallel 3-D viscoelastic finite difference seismic modelling. *Computers & Geosciences*, 28(8):887–899.

Carcione, J. M. and Tinivella, U. (2000). Bottom-simulating reflectors: Seismic velocities and AVO effects. *Geophysics*, 65(1):54–67.

Choi, Y. and Alkhalifah, T. (2012). Application of multi-source waveform inversion to marine streamer data using the global correlation norm. *Geophysical Prospecting*, 60(4):748–758.

Crutchley, G., Gorman, A., Pecher, I., Toulmin, S., and Henrys, S. (2011). Geological controls on focused fluid flow through the gas hydrate stability zone on the southern Hikurangi Margin of New Zealand, evidenced from multi-channel seismic data. *Marine and Petroleum Geology*, 28(10):1915–1931.

Delescluse, M., Nedimović, M. R., and Louden, K. E. (2011). 2D waveform tomography applied to long-streamer MCS data from the Scotian Slope. *Geophysics*, 76(4):B151–B163.

Ecker, C., Dvorkin, J., and Nur, A. M. (2000). Estimating the amount of gas hydrate and free gas from marine seismic data. *Geophysics*, 65(2):565–573.

Elger, J., Berndt, C., Rüpke, L., Krastel, S., Gross, F., and Geissler, W. H. (2018). Submarine slope failures due to pipe structure formation. *Nature Communications*, 9(1):715.

Forbriger, T., Groos, L., and Schäfer, M. (2014). Line-source simulation for shallow-seismic data. Part 1: Theoretical background. *Geophysical Journal International*, 198(3):1387–1404.

Gardner, G., Gardner, L., and Gregory, A. (1974). Formation velocity and density - The diagnostic basics for stratigraphic traps. *Geophysics*, 39(6):770–780.

Gerner, A., Saenger, E. H., and Shapiro, S. A. (2007). Attenuation of P-waves due to interlayer fluid flow in hydrate-bearing sediments. *Journal of Geophysics and Engineering*, 4(4):394.

Groos, L. (2013). *2D full waveform inversion of shallow seismic Rayleigh waves*. PhD thesis, Karlsruhe Institute of Technology.

Groos, L., Schäfer, M., Forbriger, T., and Bohlen, T. (2014). The role of attenuation in 2D full-waveform inversion of shallow-seismic body and Rayleigh waves. *Geophysics*, 79(6):R247–R261.

Guerin, G. and Goldberg, D. (2002). Sonic waveform attenuation in gas hydrate-bearing sediments from the Mallik 2L-38 research well, Mackenzie Delta, Canada. *Journal of Geophysical Research: Solid Earth*, 107(B5).

Helgerud, M., Dvorkin, J., Nur, A., Sakai, A., and Collett, T. (1999). Elastic-wave velocity in marine sediments with gas hydrates: Effective medium modeling. *Geophysical Research Letters*, 26(13):2021–2024.

Helgerud, M. B., Dvorkin, J., and Nur, A. (2000). Rock physics characterization for gas hydrate reservoirs: Elastic properties. *Annals of the New York Academy of Sciences*, 912(1):116–125.

Holberg, O. (1987). Computational aspects of the choice of operator and sampling interval for numerical differentiation in large-scale simulation of wave phenomena. *Geophysical Prospecting*, 35(6):629–655.

Jaiswal, P., Dewangan, P., Ramprasad, T., and Zelt, C. (2012). Seismic characterization of hydrates in faulted, fine-grained sediments of Krishna-Godavari Basin: Full waveform inversion. *Journal of Geophysical Research: Solid Earth (1978–2012)*, 117(B10).

Kim, H.-J., Jou, H.-T., Kang, S.-G., Lee, G. H., Yi, B. Y., Yoo, D.-G., Ryu, B.-J., and Shin, C. (2013). Seismic characterization and imaging of a gas hydrate deposit in the western part of the Ulleung Basin, the East Sea (Japan Sea). *Marine and Petroleum Geology*, 47:214–221.

Köhn, D. (2011). *Time domain 2D elastic full waveform tomography*. PhD thesis, Christian-Albrechts-Universität zu Kiel.

Komatitsch, D. and Martin, R. (2007). An unsplit convolutional perfectly matched layer improved at grazing incidence for the seismic wave equation. *Geophysics*, 72(5):SM155–SM167.

Korenaga, J., Holbrook, W., Singh, S., and Minshull, T. (1997). Natural gas hydrates on the southeast US margin: Constraints from full waveform and travel time inversions of wide-angle seismic data. *Journal of Geophysical Research: Solid Earth (1978–2012)*, 102(B7):15345–15365.

Kurzmann, A. (2012). *Applications of 2D and 3D full waveform tomography in acoustic and visco-acoustic complex media*. PhD thesis, Karlsruhe Institute of Technology.

Kvamme, B., Graue, A., Buanes, T., Kuznetsova, T., and Ersland, G. (2007). Storage of CO2 in natural gas hydrate reservoirs and the effect of hydrate as an extra sealing in cold aquifers. *International Journal of Greenhouse gas control*, 1(2):236–246.

Kvenvolden, K. A. (1988). Methane hydrate - a major reservoir of carbon in the shallow geosphere? *Chemical Geology*, 71(1-3):41–51.

Kvenvolden, K. A. (1993). Gas hydrates - geological perspective and global change. *Reviews of Geophysics*, 31(2):173–187.

Landrø, M. (1992). Modelling of GI gun signatures. *Geophysical Prospecting*, 40(7):721–747.

Lay, T. and Wallace, T. C. (1995). *Modern Global Seismology*, volume 58. Academic Press.

Leroy, C. C., Robinson, S. P., and Goldsmith, M. J. (2008). A new equation for the accurate calculation of sound speed in all oceans. *The Journal of the Acoustical Society of America*, 124(5):2774–2782.

Levander, A. R. (1988). Fourth-order finite-difference P-SV seismograms. *Geophysics*, 53(11):1425–1436.

Mora, P. (1988). Elastic wave-field inversion of reflection and transmission data. *Geophysics*, 53(6):750–759.

Nocedal, J. and Wright, S. (2006). Numerical optimization. *Springer science & business media*.

Pecher, I. A., Minshull, T. A., Singh, S. C., and von Huene, R. (1996). Velocity structure of a bottom simulating reflector offshore Peru: Results from full waveform inversion. *Earth and Planetary Science Letters*, 139(3):459–469.

Planke, S., Eriksen, F. N., Berndt, C., Mienert, J., and Masson, D. (2009). P-cable high-resolution seismic. *Oceanography*, 22(1):85.

Plessix, R.-E. and Mulder, W. (2004). Frequency-domain finite-difference amplitude-preserving migration. *Geophysical Journal International*, 157(3):975–987.

Popescu, I., Lericolais, G., Panin, N., Normand, A., Dinu, C., and Le Drezen, E. (2004). The danube submarine canyon (Black Sea): morphology and sedimentary processes. *Marine Geology*, 206(1-4):249–265.

Popescu, I., Lericolais, G., Panin, N., Wong, H., and Droz, L. (2001). Late Quaternary channel avulsions on the Danube deep-sea fan, Black Sea. *Marine Geology*, 179(1-2):25–37.

Pratt, R. G. (1999). Seismic waveform inversion in the frequency domain, Part 1: Theory and verification in a physical scale model. *Geophysics*, 64(3):888–901.

Routh, P., Neelamani, R., Lu, R., Lazaratos, S., Braaksma, H., Hughes, S., Saltzer, R., Stewart, J., Naidu, K., Averill, H., et al. (2017). Impact of high-resolution FWI in the Western Black Sea: Revealing overburden and reservoir complexity. *The Leading Edge*, 36(1):60–66.

Schwalenberg, K., Willoughby, E., Mir, R., and Edwards, R. (2005). Marine gas hydrate electromagnetic signatures in Cascadia and their correlation with seismic blank zones. *First Break*, 23(4).

Shipley, T. H., Houston, M. H., Buffler, R. T., Shaub, F. J., McMillen, K. J., Ladd, J. W., and Worzel, J. L. (1979). Seismic evidence for widespread possible gas hydrate horizons on continental slopes and rises. *AAPG Bulletin*, 63(12):2204–2213.

Singh, S. C., Minshull, T. A., and Spence, G. D. (1993). Velocity structure of a gas hydrate reflector. *Science*, 260:204–207.

Tarantola, A. (1984). Inversion of seismic reflection data in the acoustic approximation. *Geophysics*, 49(8):1259–1266.

Tarantola, A. (2005). *Inverse problem theory and methods for model parameter estimation*, volume 89. SIAM.

Virieux, J. (1986). P-SV wave propagation in heterogeneous media: Velocity-stress finite-difference method. *Geophysics*, 51(4):889–901.

Virieux, J. and Operto, S. (2009). An overview of full-waveform inversion in exploration geophysics. *Geophysics*, 74(6):WCC1–WCC26.

Waite, W. F., Santamarina, J. C., Cortes, D. D., Dugan, B., Espinoza, D., Germaine, J., Jang, J., Jung, J., Kneafsey, T. J., Shin, H., et al. (2009). Physical properties of hydrate-bearing sediments. *Reviews of Geophysics*, 47(4).

Wallmann, K., Pinero, E., Burwicz, E., Haeckel, M., Hensen, C., Dale, A., and Ruepke, L. (2012). The global inventory of methane hydrate in marine sediments: A theoretical approach. *Energies*, 5(7):2449–2498.

Warner, M., Ratcliffe, A., Nangoo, T., Morgan, J., Umpleby, A., Shah, N., Vinje, V., Štekl, I., Guasch, L., Win, C., et al. (2013). Anisotropic 3D full-waveform inversion. *Geophysics*, 78(2):R59–R80.

Winguth, C., Wong, H., Panin, N., Dinu, C., Georgescu, P., Ungureanu, G., Krugliakov, V., and Podshuveit, V. (2000). Upper quaternary water level history and sedimentation in the northwestern Black Sea. *Marine Geology*, 167(1-2):127–146.

Wood, A. (1941). A textbook of sound. *Bell, London*.

Wyllie, M., Gregory, A., and Gardner, G. (1958). An experimental investigation of factors affecting elastic wave velocities in porous media. *Geophysics*, 23(3):459–493.

Zander, T., Haeckel, M., Berndt, C., Chi, W.-C., Klaucke, I., Bialas, J., Klaeschen, D., Koch, S., and Atgın, O. (2017). On the origin of multiple BSRs in the Danube deep-sea fan, Black Sea. *Earth and Planetary Science Letters*, 462:15–25.

Zelt, C. and Smith, R. (1992). Seismic traveltime inversion for 2-D crustal velocity structure. *Geophysical Journal International*, 108(1):16–34.

Zillmer, M., Flueh, E. R., and Petersen, J. (2005). Seismic investigation of a bottom simulating reflector and quantification of gas hydrate in the Black Sea. *Geophysical Journal International*, 161(3):662–678.

List of Figures

List of Tables

Danksagung

Danken möchte ich allen Personen, die mich bei meiner Arbeit unterstützt oder einen Teil der Zeit, die ich am GPI verbracht habe, auf irgendeine Art begleitet haben.

Zuerst geht mein Dank an meinen Hauptreferenten Thomas Bohlen, der die Idee zu dieser Arbeit entwickelt und mir immer wieder zu neuen Ideen verholfen hat, wenn es scheinbar nicht mehr weiter ging. Durch seine Betreuung habe ich gelernt, dass letztendlich für jedes Problem doch eine Lösung zu finden ist. Danke auch für die Möglichkeit, aktiv an der Projektplanung und -durchführung mitzuwirken und dabei viele Kontakte knüpfen zu können. Ebenso konnte ich an Konferenzen teilnehmen und auch internationale Erfahrung sammeln.

Andreas Rietbrock danke ich dafür, dass er das Korreferat für diese Arbeit übernommen hat und für die vielen hilfreichen Anmerkungen.

Eine besondere Erfahrung waren die Projekttreffen mit den Partnern aus unserem SUGAR-Teilprojekt, die stets neue Impulse gegeben und häufig einen anderen Blickwinkel auf manche Ergebnisse aufgezeigt haben. Auch die gemeinsamen Abendessen bei mehrtägigen Tagungen mit fachlichen und nichtfachlichen Diskussionen waren eine schöne Erfahrung. Danke an Gerald, Ina, Markus, Peter, Jörg, Anke, Timo, Marion, Sebastian, Katja, Erik und Judith!

Der Arbeitsgruppe Angewandte Geophysik mit all ihren wechselnden Mitgliedern danke ich für die abwechslungsreiche Zeit, die unterhaltsamen Mittagspausen und die regelmäßigen Zusammenkünfte, um selbstgemachten Kuchen zu genießen. Besonderer Dank geht an Niklas, mit dem die gemeinsame Zeit in unserem Büro durch viele Diskussionen und Gespräche nie langweilig wurde. Dein Optimismus und deine Motivation werden mir fehlen! Thomas H. danke ich für die vielen Anregungen und Verbesserungen für Manuskripte und Texte und auch für sein Engagement in der Arbeitsgruppe. Außerdem geht mein Dank an Thomas F. für die gute Zusammenarbeit nicht nur in der Lehre. Zu guter Letzt danke ich Claudia und Petra für die (technische) Unterstützung während der gesamten Zeit, sowie allen anderen Institutsmitgliedern, die bei Problemen immer zur Stelle waren.

Großer Dank geht natürlich auch an Familie und Freunde, die immer ein offenes Ohr haben und für die nötige Abwechslung zum Uni-Alltag sorgen. Ganz besonders danke ich Jannis für die gemeinsame Zeit, ohne dich hätte ich das nicht geschafft!

Acknowledgment

The software IFOS2D is available from the website http://www.gpi.kit.edu/Software-FWI.php under the GNU General Public License.

This work was carried out in the framework of the SUGAR-III project funded by BMWi (grant number 03SX381C).

Computing time was granted on the supercomputer JURECA at Juelich Supercomputing Centre (JSC) and ForHLR I and II at the Karlsruhe Institute of Technology (KIT).